Western $\boxtimes$ Graduate&PostdoctoralStudies

4-20-2017 12:00 AM

The study of plasmonics in nanohole metallic metamaterials

Kieffer J. Davieau, *The University of Western Ontario*

Supervisor: Dr. Mahi R. Singh, *The University of Western Ontario*
Joint Supervisor: Dr. Jeffrey Carson, *The University of Western Ontario*
A thesis submitted in partial fulfillment of the requirements for the Master of Science degree in Physics
© Kieffer J. Davieau 2017

Recommended Citation

Abstract

Plasmonics is the study of light-matter interaction. The interaction of incident light (photons) with surface plasmons present in metamaterials results in unique optical properties. Nanohole arrays are a metamaterial consisting of an array of sub-wavelength holes perforated in an optically thin metallic film which resides upon a dielectric material. The interaction of light with the surface plasmons present in the nanohole array leads to extraordinary optical transmission which produces resonance peaks with a higher intensity than the incident light. By changing the physical parameters of the nanohole array, such as hole size and periodicity, the resonance peaks can be tuned to different locations. This is used in applications such as surface plasmon resonance sensing and surface enhanced Raman spectroscopy studied in this thesis.

Previous derivations of transmission and absorption coefficients show that the transmission is only dependent on the periodicity of the nanohole array [1]. However, numerous simulated and experimental results have shown that the periodicity and hole size have an effect on the transmission and absorption of nanohole arrays.

Keywords

Absorption, extraordinary optical transmission, nanohole array, metamaterial, metamaterial hybrids, plasmonics, surface enhanced Raman spectroscopy, surface plasmon, transmission.

Acronyms

Acronym	Definition
3D	Three Dimensional
DDI	Dipole-Dipole Interaction
EBL	Electron Beam Lithography
EB-PVD	Electron-Beam Physical Vapor Deposition
EF	Enhancement Factor
EOT	Extraordinary Optical Transmission
FDTD	Finite-Difference Time-Domain
LSPR	Localized Surface Plasmon Resonance
NH	Nanohole
NHA	Nanohole Array
PML	Perfectly Matched Layer
QE	Quantum Emitter

SEF	Surface-Enhanced Fluorescence
SEIRA	Surface-Enhanced Infra Red Absorption
SEM	Scanning Electron Microscopy
SERS	Surface-Enhanced Raman Spectroscopy
SP	Surface Plasmon
SPP	Surface Plasmon Polariton
SPR	Surface Plasmon Resonance
SRR	Split Ring Resonator
TERS	Tip-Enhanced Raman Spectroscopy

Co-Authorship and Acknowledgments

Co-Authorship

Chapters 3, 4 and 5 are composed of two publications which were co-authored by the following people:

Chapter 3

Tabatabaei, M., Najiminaini, M., Davieau, K., Kaminska, B., Singh, M.R., Carson, J.J.L., & F. Lagugné-Labarthet. "Tunable 3D plasmonic cavity nanosensors for surface-enhanced Raman spectroscopy with sub-femtomolar limit of detection." ACS Photonics 2(6): 752-759 (2015).

Dr. Tabatabaei provided the experimental and fabrication results of the 3D plasmonic cavity nanosensor for SERS. Dr. Najiminaini provided the experimental results such as fabrication of the NHA and the optical characterization setup. Dr. Kaminska, Dr. Singh, Dr. Carson, and Dr. Lagugné-Labarthet all provided supervision over the manuscript. They also aided in reading and editing of the manuscript. Dr. Lagugné-Labarthet provided concept for the project. I provided the simulated results as well as the figures. I also compared both experimental results with simulated results.

Chapters 4 and 5

M. R. Singh, K. J. Davieau, and J. J. L. Carson, "Effect of quantum interference on absorption of light in metamaterial hybrids." Journal of Physics D: Applied Physics, 49(44) (2016).

Dr. Singh helped in providing the theoretical calculations and results. He also provided the project concept, as well as supervision over the project. Dr. Carson aided in reading and editing of the manuscript. He also provided supervision over the project. I helped in providing theoretical, simulated, and experimental data. I also compared both the theoretical data with the experimental data. I also provided the experimental fabrications.

Acknowledgments

Dedication

I dedicate this Thesis to my loving parents, Daya and Arthur Underwood,

and to my beloved father, Arthur Davieau. They have supported me as

a team, through thick and thin, earning them my sincere appreciation.

A special thank you goes to my mother, who introduced me

to science at a very young age. It was her individual support

and encouragement which got me as far as I have.

I am thankful to be able to share my passion for science with her.

Table of Contents

List of Figures

physical parameters were $e_f = 1.0$, $e_d = 1.5$, $\hbar\omega_p = 5eV$, $W = 1.0$, $P = 5.0$, $a = 2$, $R = 20nm$, $k_{sp} = 0.5/R$,

$g^{nr} = 3$, and $\hbar\omega_{ba} = 0.5$ 69

List of Appendices

<center>Chapter 1</center>

1   **Introduction**

Plasmonics is the study of light-matter interaction. In this thesis, the interaction of incident light (photons) with surface plasmons present in metamaterials was studied. The metamaterials consisted of an array of sub-wavelength holes that are perforated in an optically thin gold film. These metamaterials are referred to as nanohole arrays (NHAs) [1], [2], [3], [4], [5].

NHAs have optical properties that allow the incident light to couple with the surface plasmons (SPs) present at the interface between a dielectric material and a metallic material. The coupling of the light with the surface plasmons excites the surface plasmons leading to extraordinary optical transmission (EOT) [1]. EOT is a phenomenon where the light decouples from the excited surface plasmons producing resonance peaks at specific wavelengths. The resonance peaks that are observed due to the EOT phenomenon have a higher intensity than the intensity of the incident light [1], [3], [4]. This phenomenon leads to many novel applications such as surface plasmon resonance (SPR) sensing [6], [7], [8], [9], surface enhanced Raman spectroscopy (SERS) [10], [11], [12], [13] and multispectral filtering [14].

The effects of EOT in NHA metamaterials were studied in this thesis for the application of SERS. Recent advances of SERS platforms include the use of metallic structures with EOT properties combining the functions of optical trapping and increasing the enhancement factor of SERS measurements to improve the detection of a single

<center>– 1 –</center>

molecule. The NHA metamaterials fabricated in this thesis were designed to improve each factor for SERS measurements.

Furthermore, theoretical derivations for the absorption and transmission of light on NHAs are compared with experimental results to show which physical parameters of NHAs have an effect on the absorption and transmission spectra.

1.1   Background Research

In 1998, Thomas Ebbesen discovered the phenomenon of extraordinary optical transmission (EOT) in a metallic film perforated with an array of sub-wavelength holes [1]. Ebbesen et al. studied the transmission spectra of these NHAs and observed that there are resonance peaks with a higher transmission than the incident light. They found that the periodicity of the nanoholes scale exactly with the positions of the resonance peaks. They also found that the ratio between thickness and hole size influenced the width of the resonance peaks. As the ratio of thickness divided by hole size approaches 1, the resonance peak has a narrower width referred to as the maximum sharpness, as opposed to when the ratio approaches 0 where the resonance peak has a broader width [1]. The enhanced transmission, combined with the relationship of the physical parameters of a NHA with the resonance peak, allows NHAs to be used in sensing and filtering applications [7], [23], [15], [16], [17], [18].

Therefore, NHAs can be used for surface plasmon resonance (SPR) sensing applications due to the transmission spectra shifting depending on the refractive index of the dielectric material. An increase in the refractive index results in the transmission spectrum red-

shifting, where as a decrease in the refractive index results in the transmission spectrum blue-shifting. The SPR sensitivity can be expressed as the change in resonance peak position ($\Delta\lambda$) divided by the refractive index unit (RIU) [3], [4]. SPR applications involve binding a chemical to the surface of the gold that, in turn, changes the refractive index of the dielectric resulting in a shift in the transmission spectrum.

Another application which was studied in this thesis is surface enhanced Raman spectroscopy (SERS). Similar to SPR sensing, SERS – the enhancement and detection of Raman signals of a specific molecule – requires a high SPP resonance peak transmission. Without this enhancement, a Raman signal for a molecule is generally too weak to measure [19], [20], [21], [22]. It has been previously studied that the Raman signal can be enhanced with the use of a NHA. Due to the coupling of light with SPs, if a molecule is absorbed onto the surface of the NHA, an increase in the enhancement factor (EF) can be observed as a result of the EOT. Conventional NHAs have shown to increase the EF by 10^5 relative to the Raman signal [8]. Higher EFs are of interest since a higher EF can lead to the detection of a smaller concentration of molecules.

Previous research on the theory of NHAs found that the location of resonance peaks was dependant on the periodicity and hole size of the NHAs [2], [3], [4], [5]. They theoretically and experimentally investigated the scattering cross-section of NHAs with various unique periodicities and hole sizes. By solving the Hamiltonian of the surface plasmon polaritons (SPPs) in the second quantized form, they developed a theory of the scattering cross sections. This theory was developed based on Green's function method and the quantum

scattering theory which can be used in the optimization of NHAs for sensing, medical, and engineering applications [4], [7], [8], [9], [23], [24], [25], [26].

1.2   Metamaterials

Recently, due to the EOT phenomena, there has been considerable interest in the study of metamaterials such as NHAs. These metamaterials are arrays of periodic nanoholes in a metallic film that act as plasmonic substrates with diverse applications [1], [6], [27], [28]. The NHA structure in an optically thin metal film allows for momentum matching between light incident on a NHA and the SP waves existing at the interface between a metal and a dielectric material (refer to Fig. 1 in Chapter 2). Experimentally, it is found that NHAs can transmit more radiation than the incident light upon the nanohole apertures due to the presence of SPs [29], [30], [31], [32]. Other metamaterials consist of split ring resonators (SRRs) as well as metallic nanorods [32].

NHAs are considered to be 2-dimensional and consist of nanoholes in a thin metallic film on top of a Pyrex substrate. The energy matching of light with SPs lead to the excitation of SPs as light is incident on the NHAs. The excited SPs become localized around the edge of the nanohole and are referred to as localized surface plasmons (LSPs). Due to the localized surface plasmon resonance (LSPR) having a higher transmission than incident light, NHAs can be used in applications such as SERS where the LSPR leads to a high enhancement factor [33], [34], [35], [36].

NHAs can be fabricated with cavities beneath the metallic material. During this fabrication process, metallic nanocones can be deposited in these cavities creating

a 3-dimensional NHA structure (refer to Fig. 9 in Chapter 3). When the incident light couples with the SPs, LSPs are located along the edge of the nanohole as well as on the top of the nanocone. When a nanocone is close to the nanohole, the LSPs interact with each other creating a higher intensity for the LSPRs than the original 2D NHA. This effect leads to an even higher enhancement factor than the previous 2D NHAs. Therefore, due to the higher enhancement factor, a 3D NHA structure is more desirable for SERS applications [37], [38], [39], [40], [41].

As studied in this thesis, other metamaterial structures arranged periodically in a lattice form consist of split ring resonators (SRRs) which have a similar effect as NHAs since they also allow for the coupling of incident light to SPs.

1.3   Motivation and Objective of Thesis

The motivation behind my research was to provide optimal results via simulations as opposed to the manual process used until now. The manual process involves fabricating one or two NHA structures and then simulating them which is quite time consuming and costly – it can also be less accurate depending on the impurities in the NHA when fabricating. In comparison, the simulation process involves simulating thousands of different NHAs but fabricating only the few simulations that provide the best results for a desired application, which is more efficient as it saves time and money. In other words, the simulation process can be described as providing "optimal results" for desired applications.

In the first paper I co-authored, my motivation was to create a 3-dimensional nanostructure that provided a higher enhancement factor than the previously studied

2-dimensional nanostructure compared to the Raman signal. A 2-dimensional nanohole array cannot generate a strong enough resonance compared to a 3-dimensional nanostructure, resulting in limited detection and sensitivity in SERS applications.

For the second paper I co-authored, the motivation was to study the effects that metamaterials have on the NHA absorption and transmission coefficients in order to find a better relationship between metamaterials and their transmission. While one can measure the transmission of a metamaterial, knowing how to manipulate the transmission would allow for a better understanding of the metamaterial structure. The effect of interference between quantum dots and the nanostructure was also studied. This effect can be used for many sensing applications as well as other photonic applications, hence its importance.

It was found that, when probed with energy, the quantum dots may interfere with each other and result in either destructive or constructive interference. This is of importance as it can be used for novel applications such as optical switches – destructive interference resulting in a lack of transmission and constructive interference resulting in transmission.

The main objective of this thesis was to create 2- and 3-dimensional nanostructures that would support the applications presented herein. This involves the study of light-matter interaction in metallic metamaterials. To this end, I started by creating a program that could simulate the light-matter interaction of various nanostructures. The program simulated thousands of NHAs with varying parameters and then compared the transmission spectrum of each NHA. In doing so, the resulting simulation data was compared with existing experimental and theoretical data. For example, for the SERS

application regarding the detection of a specific molecule, a nanostructure with optical resonance peaks matching the optical properties of the molecule was required. The numerous data comparisons confirmed that the program I wrote was successful in creating a nanostructure with the most optimal resonance peaks. This nanostructure was then physically fabricated and the results of the experiment were compared with the simulation which confirmed the validity of the simulations when the comparison agreed. The same could be done for other applications involving fabrications or theoretical calculations.

1.4   Chapter Summaries

Following this section, the second chapter describes the fundamental properties of metamaterials and the physics behind the strange phenomenon of EOT that allows for applications used in this thesis. It also describes the methods used to fabricate and simulate the 2D and 3D NHA structures that appear in latter chapters.

In the third chapter, the optical enhancement effects of a NHA structure was studied for the application of SERS. NHAs have been used for the detection of molecules in low concentrations due to their providing a higher EF than the Raman signal. EFs can be increased through characteristics such as the energy matching between light and SPs and the energy matching between the resonance peak and the Raman signal. Previous studies show that 2D NHAs provided an enhancement factor of up to 10^5 higher than the original Raman signal [42], [43], [44], [45], [46]. In other words, this chapter studied the effect that 3D NHA structures have on the enhancement factor. The 3D NHA structure consists of nanoholes perforated in a gold film similar to a 2D NHA but with an underlying cavity and metallic nanocones residing beneath the nanoholes (refer to Fig. 9 in Chapter 3).

Having the nanocones in a cavity beneath the nanoholes provides another factor to the enhancement of the Raman signal. This is the result of localized surface plasmon coupling between the nanocone and nanohole (refer to Fig. 11 in Chapter 3). This allows the detection of smaller concentrations of molecules in comparison to the 2D NHA and can also be used for optical trapping applications [47].

In the fourth chapter, the absorption coefficient of a metallic metamaterial is theoretically derived and compared to the experimental results of a NHA. The light-matter interaction in metallic metamaterials made from an array of split ring resonators (SRR) was also theoretically investigated.

The transmission coefficient spectrum was measured for three samples, each having a unique NHA hole size and periodicity. Each measured spectrum had several peaks due to SP resonance variatons. The transmission line theory of metamaterials and Bloch's theorem was used to calculate the SP energies. The absorption and transmission coefficient was calculated using the quantum scattering theory and Green's function method [48], [49], [50], [51], [52], [53], [54], [55].

Due to the similarity in deriving the absorption coefficient of a SRR and deriving the absorption coefficient of a NHA, the theoretical data was compared to the experimental data of a NHA.

In the fifth chapter, the effect of quantum interference on the absorption of light was studied. This effect was observed at the interface of a metamaterial and a dielectric material, where an ensemble of non-interacting quantum emitters (QEs) was deposited.

Quantum interference occurs when two multilevel atoms spontaneously decay and interfere with each other [48] - [55].

Spontaneous emission cancellation can occur when two excited states of an atom decay and the two resulting decay pathways are not independent of each other. This phenomenon, as well as the study of quantum coherence and quantum interference, has lead to many novel effects such as induced transparency, dark spectral lines and lasing without population inversion [65].

The sixth chapter includes a summary of the main conclusion behind the research relating to each chapter as well as future recommendations for future research.

Appendix A outlines the code created and used for generating and comparing simulation data. This code generates a graphical user interface (GUI) that allows a user to choose what type of metamaterial they want to simulate as well as the parameters for the chosen metamaterial. It also allows the user to determine a range of parameters so that the program simulates a single metamaterial numerous times including varying parameters and compares the results of each simulation. This code was used for all simulations in this thesis and also generated the data for the color map (refer to Fig. 7 and Fig. 8 in Chapter 2).

Appendices B and C outline the supporting information for Chapter 3 as well as Chapters 4 and 5.

Chapter 2

I would like to acknowledge Dr. Tabatabai for providing the SERS research and results as well as Dr. Najiminaini for helping with the experimental results and fabrication of the NHAs.

2 Fundamentals

This chapter describes in detail the fundamentals when light interacts with metallic metamaterials and the phenomenon that occur. The metallic metamaterials studied in this thesis consist of nanohole arrays and an array of split ring resonators. These metamaterials consist of a 3D metallic structure on top of a dielectric material. At the interface of the metal and dielectric material are surface plasmons (SPs).

These SPs can interact with incident light if the energy of the incident light and the energy of the SPs are matching. In order to match the energies of both incident light and SPs a metamaterial is needed. In the case of this thesis a nanohole array as well as a split ring resonator is studied as they both allow for energy matching between SPs and the incident light. The coupling of a SP and incident light creates a surface plasmon polariton, which also occurs at the interface between the metal and dielectric material. Surface plasmon resonances occur due to constructive interference between the SPs and the incident light.

These surface plasmon resonances lead to an interesting phenomenon called extraordinary optical transmission (EOT) [1]. Depending on the geometry and physical characteristics of the metamaterial, the EOT produces enhanced transmission of light at specific wavelengths. By changing the geometry and physical characteristics the EOT can occur at different wavelengths. A metamaterial such as a nanohole array has unique optical properties that allow for EOT to occur in the visible and near infrared ranges [15], [27]. This leads to many different novel applications such as multispectral filtering, surface plasmon resonance (SPR) sensing, and surface enhanced Raman spectroscopy applications, which is studied in this thesis.

2.1 Surface Plasmons

Surface plasmons (SPs) are the collective oscillations of free electrons at the interface between a metal and dielectric material [53], [54]. SPs are highly localized within the interface of the two materials. SPs depend on the geometry of the metallic material and the coarseness of the metallic surface. The dielectric constant of a surface plasmon can be found in the Shankar paper [32], [56].

2.2 Surface Plasmon Polaritons

When a SP is normal to the surface of the interface, the field intensity drops at an exponential rate. As illustrated in Fig. 1 the SP oscillations exist at the interface.
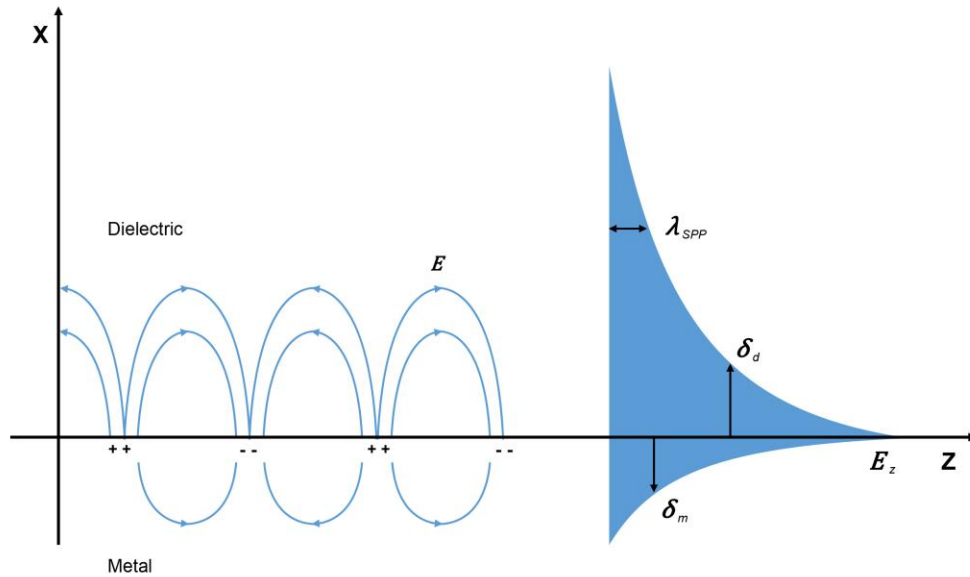
Figure 1 — Free electrons oscillating at the interface between metal and dielectric. The decay of the SPs for a dielectric and a metal.

This occurs between a metal and a dielectric material when the real part of the dielectric function for the two materials are opposite in sign. At the interface between the two materials the real part of the dielectric function must be less than zero but greater than the dielectric constant of a dielectric material in magnitude [57]. The length of the SP wave propagating at the interface can be estimated by:

$$L_{sp} = \frac{c}{\omega} \left(\frac{\varepsilon'_m + \varepsilon_d}{\varepsilon'_m \varepsilon_d}\right)^{3/2} \frac{(\varepsilon'_m)^2}{\varepsilon''_m} \qquad \textbf{Equation 1}$$

where ε_d is the dielectric constant of the dielectric material, ε'_m and ε''_m are the real and imaginary parts of the dielectric function for the metal. The decay of the SP wave along the interface is caused by ε''_m. The decay of the SP normal to the interface can be found by:

$$\delta_{sp} = \frac{c}{\omega} \left(\frac{\varepsilon'_m + \varepsilon_d}{\varepsilon_d^{\,2}} \right)^{1/2}$$ **Equation 2**

This can be used to calculate the decay for any metal/dielectric interface such as gold/air or gold/glass discussed in this thesis.

While it is possible to excite SPs by using metal-impinged electrons, this cannot be done optically. Since light momentum is not sufficient to couple to the SPs, light can therefore not couple to or excite SPs on a smooth metal-air interface.

The dispersion relation of SPs on a smooth metal film, from the conservation of energy, can then be expressed by:

$$\left| \vec{k}_{sp} \right| = \left| \vec{k}_0 \right| \sqrt{\frac{\varepsilon_m \varepsilon_d}{\varepsilon_m + \varepsilon_d}}$$ **Equation 3**

where ε_m indicates the dielectric function of metal, and ε_d indicates the dielectric's dielectric constant, and where $\vec{k}_0 = \frac{\omega}{c}$ indicates the incident excitation photon's free space wavenumber.

Light and SP's dispersion curves are shown in Fig. 2 illustrating the location of the SP curve being outside the accessible region surrounded by the light line, concluding that the light can therefore not excite SPs at the interface between metal and dielectric.
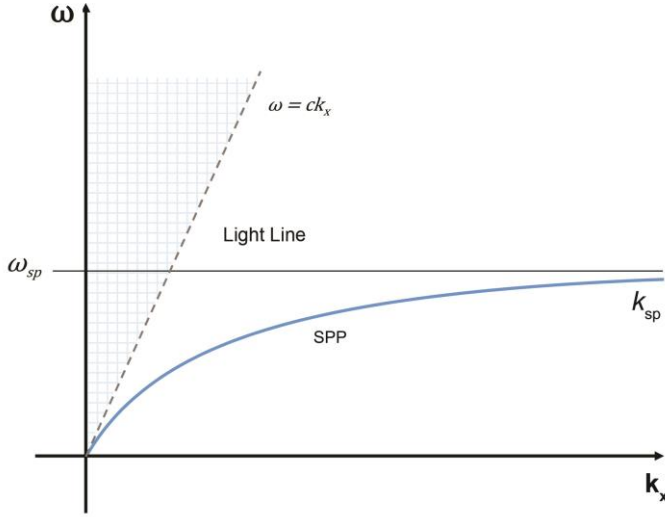
Figure 2 — Dispersion curves of SP and light line ($\omega = ck_x$), where ω_{sp} indicates a SP frequency.

Therefore, features such as prisms, gratings, or surface roughness are necessary to increase the momentum of light to excite SPs, at any specific wavelength, since SPs have higher momentum than incident light at the dielectric-metal interface [27], [53]. However, due to the grating structure and results in coupling of light to SP, light momentum increases in the case of a 2-dimensional grating in a metal film (e.g. an array of periodic holes in a metal film). The dispersion relation between light and SP on a metallic grating structure, specifically when a plane wave is incident on a grating structure with a square lattice arrangement, can be expressed by:

$$\vec{k}_{sp} = \vec{k}_0 \sin \theta \pm i\, \vec{u}_x \pm j\, \vec{u}_y \qquad\qquad \textbf{Equation 4}$$

where $\vec{k}_0 \sin \theta$ indicates the wave vector of the incident light's in-plane component, $k_0 = \dfrac{\omega}{c}$ [1], [58] and where $\vec{u}_x$ and $\vec{u}_y$ indicate the reciprocal lattice wave vectors for

a square lattice with $|\vec{u}_x| = |\vec{u}_y| = 2\frac{\pi}{p}$ (where p indicates the spacing between adjacent holes), and where i and j specify integers expressing the scattering mode indices (see Fig. 3 for examples of i and j). Inserting Eqn.3 into Eqn. 4 results in the dispersion relation between light and SP, which is formulated as:

$$|\vec{k}_{sp}| = \left[\left(\frac{2\pi}{\lambda} \sin(\theta) + i \frac{2\pi}{p}\right)^2 + \left(j \frac{2\pi}{p}\right)^2\right]^{\frac{1}{2}} = |\vec{k}_0|\sqrt{\frac{\varepsilon_m \varepsilon_d}{\varepsilon_m + \varepsilon_d}} \qquad \textbf{Equation 5}$$

2.3 Extraordinary Optical Transmission

The phenomena of extraordinary optical transmission (EOT) was the result of an array of periodic sub-wavelength holes fabricated in an optically thin metal film was discovered by Thomas W. Ebbesen in 1998 [59].

Surpassing the diffraction limit of light, this unique optical property is due to excitation of SP waves existing at the interface of the dielectric and the metal.

The periodic arrangement of the sub-wavelength holes produce momentum matching between the SP and the light, resulting in the occurrence of SP excitation [59]. Further results show the coupling of the light to the SP and evanescent transmission through the sub-wavelength hole array continuing with the light decoupling from SP and radiating to free space.

The wavelengths at which the SP excitation modes can be expressed, for a grating or sub-wavelength hole structure with square lattice arrangement, relating to a normally incident plane wave on an array of periodic sub-wavelength holes (by inserting $\theta = 0$ in Eqn. 5), can be expressed by:

$$\lambda_{max} = \frac{p}{\sqrt{i^2 + j^2}} \left(\frac{\varepsilon_m \varepsilon_d}{\varepsilon_d + \varepsilon_m} \right)^{\frac{1}{2}}$$

Equation 6
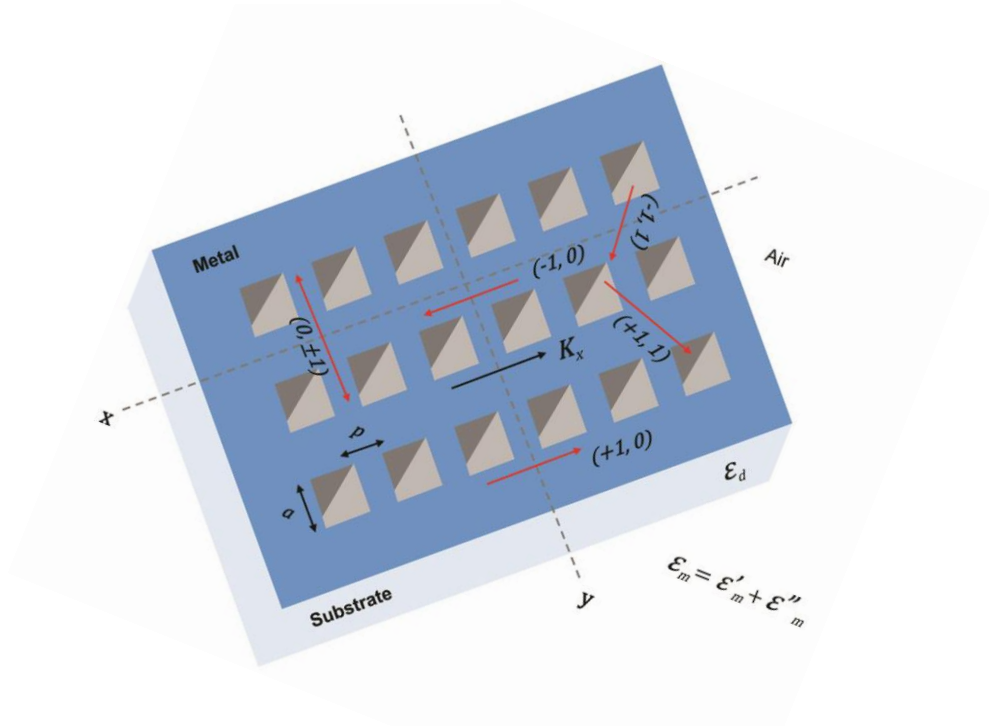
Figure 3 — A 2-dimension sub-wavelength hole array in a metal film on a substrate in a square lattice arrangement where p indicates the spacing between two adjacent holes, a indicates a width of each hole, Kx wave vector of the light is along the x-axis, and where (+1,0), (-1,0), (0,±1), (+1,1), and (-1,1) are various (i, j) grating modes.

Whenever incident light is normal to the surface of sub-wavelength hole array, Eqn. 6 can be used to estimate the EOT positions of sub-wavelength hole arrays for various SP excitation modes (i ,j) [59]. Furthermore, the direction of the light wave vector (K_x) greatly affects the various SP excitation modes.

For example, as shown in Fig. 3, it was found that various (i, j) SP excitation modes relate to metal/air or metal/substrate interfaces when the wave vector of the light (K_x) is along the x-axis. The (+1,0), (-1,0), (0,±1), (+1,1), and (-1,1) designate various grating modes resulting in various SP excitation modes from metal/air or metal/substrate sides by the light.

While other grating modes such as (+2,0) and (-2,0) do exist, these were not illustrated in Fig. 3. In this figure, the (0,±1) SP excitation mode are perpendicular to the K_x and the (±1,0) SP excitation modes are parallel to the wave vector of the light (K_x). However, the (±1,0) and (0,±1) SP excitation modes result in a spectral overlap in the optical transmission spectra of the structure and a single resonance called (1,0) EOT peak whenever the light is normal to the surface of the sub-wavelength hole array. The results are similar for (+1,1), and (- 1,1) in the case of light that is normal to the surface of the sub-wavelength hole array.

A transmission minimum occurs before each EOT at a shorter wavelength (Wood's anomaly), in a similar way of calculating EOT positions. This transmission minimum is caused by the diffraction of light by the grating and its propagation in the dielectric.

When a transmission minimum occurs, the diffracted wave becomes tangent to the grating and propagates within the dielectric resulting in the diffracted wave matching the grating periodicity, expressed by:

$$k_{diff} = \frac{w}{c}\sqrt{\varepsilon_d} = i\,\vec{u}_x \pm j\,\vec{u}_y \qquad\qquad \textbf{Equation 7}$$

where ε_d is a dielectric constant of the propagation medium. The transmission minimum

for a sub-wavelength hole array's position can be expressed as:

$$\lambda_{min} = \frac{p}{\sqrt{i^2 + j^2}} \, (\varepsilon_d)^{\frac{1}{2}}$$

<div align="right">**Equation 8**</div>

2.4   Nanohole Array

A nanohole array (NHA) consists of a periodic array of nanoholes perforated in an

optically thin metallic film as shown in Fig. 4. In this thesis, the NHAs consist of circular

holes perforated in an optically thin gold (Au) film. This gold film is deposited on top of

a Pyrex substrate.

The dielectric material used was either air or water. The index of refraction for air is 1

and for water is 1.33. The optical transmission characteristics of NHAs can be tuned by

changing the nano-hole diameter as well as the periodicity between the nanoholes.
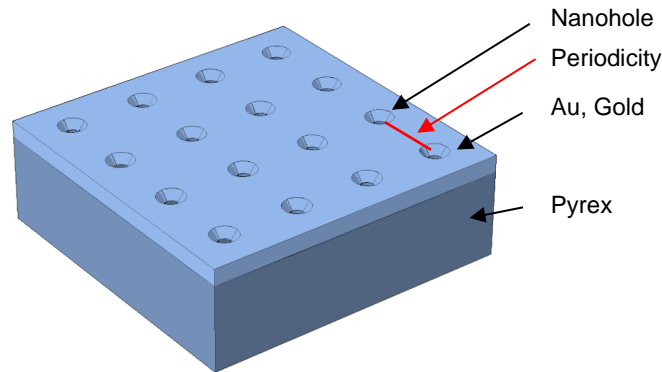
Figure 4 — A 3-dimensional view of a NHA

Equation 8 shows the relationship between the location of the SP excitations and the periodicity of the NHA which are dependent on each other. However, Fig. 5a shows the relationship between the SP excitations as well as the hole size and periodicity of the NHA.

As the periodicity increases, the SP excitation wavelength red-shift in the optical transmission spectrum. As the periodicity decreases, the SP excitation wavelength blue-shifts. However, the hole size influences intensity and bandwidth of the SP excitation. As the hole size increases, the intensity and bandwidth also increases as illustrated in Fig. 5b.
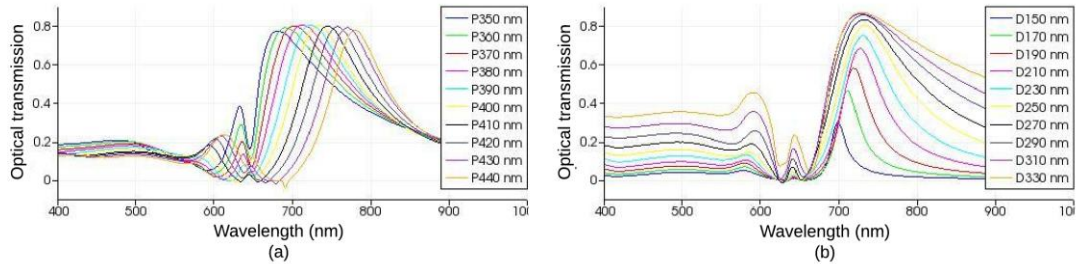
Figure 5 — Optical transmission spectra of NHAs with (a) variable periodicity, ranging from 350 nm to 440 nm in 10 nm increments and constant nano-hole diameter of 250 nm, and (b) variable hole diameter, ranging from 150 nm to 330 nm in 20 nm increments and constant periodicity of 400 nm.

2.5   Transmission Coefficient

The nano-hole array structure on the Pyrex substrate contains surface plasmon polaritons (SPPs) that have quantized energy ε_n with eigenket $|n\rangle$. Having two states, the SPP modes participating in the transmission process have energies ε_1 and ε_2.

The ground state is denoted by $|1\rangle$ with energy ε_1 while the next excited state is denoted

by $|2\rangle$ with energy ε_2 as shown in Fig. 6.

The nano-hole array structure's transmission coefficient T_{trans} due to the absorption

and emission of SPPs between the states $|1\rangle$ and $|2\rangle$ is expressed as [55]:

$$T_{trans} = \alpha_0 \, \mathrm{Im}(\rho_{12}) \qquad \qquad \text{Equation 9}$$

where

$$\alpha_0 = \frac{\mu_{12}\varepsilon_p}{\hbar E_p c} \qquad \qquad \text{Equation 10}$$
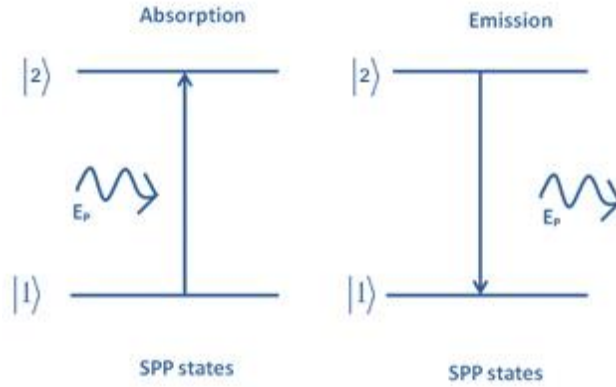
Figure 6 — Energy level diagram of transmission process. The SPP will absorb energy of a photon to be taken from ground state to excited state. Once the SPP decays back to the ground state, it emits the photon back.

Here, $\mu_{12} = \langle 1|\mu|2\rangle$ and $\rho_{12} = \langle 1|\rho|2\rangle$ represent dipole and density matrix elements

between states $|1\rangle$ and $|2\rangle$ respectively and E_p represents the amplitude of incident EM

field and ε_p represents the energy of the incident EM field.

Using the density matrix method, the density matrix elements, including element ρ_{12}, were evaluated using the following equation of motion:

$$\frac{d\rho(t)}{dt} = \frac{i}{\hbar}[H, \rho(t)]$$

Equation 11

where $H = H_0 + H_{int}$,

where H_0 is the non interacting Hamiltonian. It consists of two parts, (1) a photon Hamiltonian H_{ph}, and (2) a plasmon Hamiltonian H_{pl}. Hence H_0 can be expressed as:

$$H_0 = H_{ph} + H_{pl}$$

Equation 12

In Eqn. 11 H_{int} is the interacting Hamiltonian between plasmon and photon. It is the interaction between SPP and CLE. Hence it is expressed as:

$$H_{int} = H_{ph-pl} + H_{CLE-SPP}$$

Equation 13

We can express the density matrix method in Eqn. 11 in the matrix notation. We denote $|i> = |0>, |1>$, and $|j> = |0>, |1>$. The Eqn. can be rewritten as:

$$-i\hbar \frac{d}{dt} <i|P|j> = <i|H, P|j>$$

$$= <i|HP|j> - <i|PH|j>$$

Equation 14

The right side of Eqn. 14 can be further expanded as:

$$i\hbar \frac{dP_{ij}}{dt} = \sum_n <i|H|n><n|P|j> - \sum_n <i|P|n><n|H|j>$$

$$i\hbar\frac{dP_{ij}}{dt} = \sum_n\left(H_{in}P_{nj} - P_{in}H_{nj}\right)$$ **Equation 15**

where $P_{ij} = <i|P|j>$ and $H_{ij} = <i|H|j>$.

For the two-level system $n = |1>, |2>$, the density matrix Eqn. can be expressed as:

$$i\hbar\frac{dP_{11}}{dt} = H_{11}P_{11} + H_{12}P_{21} - (P_{11}H_{11} + P_{12}H_{21})$$

$$i\hbar\frac{dP_{12}}{dt} = H_{11}P_{12} + H_{12}P_{22} - (P_{11}H_{12} + P_{12}H_{22})$$ **Equation 16**

$$i\hbar\frac{dP_{21}}{dt} = H_{21}P_{11} + H_{22}P_{21} - (P_{21}H_{11} + P_{22}H_{21})$$

$$i\hbar\frac{dP_{22}}{dt} = H_{21}P_{12} + H_{22}P_{22} - (P_{21}H_{12} + P_{22}H_{22})$$ **Equation 17**

Note that to calculate the absorption and emission coefficient from Eqn. 9, we need to calculate the matrix operator P_{12}. Note that P_{12} in Eqn. 17 can not be evaluated from one equation and therefore, in order to solve Eqn. 17, it needs to be calculated in MAPLE software.

2.6   Methods

This section defines the different methods used for simulations, fabrications and optical characterizations of metallic nano-hole arrays presented in this thesis. Prior to fabrication the first approach is to simulate different geometrical parameters of nano-hole arrays using a finite-difference time-domain (FDTD) method. Lumerical FDTD Solutions

provides a software using this method that is used to simulate the different geometries of the nano-hole arrays.

After choosing an optimal simulation for a specific application, the nano-hole array will be fabricated. The nano-hole arrays were fabricated at the Western Nanofabrication Facility using Electron Beam Lithography (EBL) methods described in this chapter. After fabrication comes optical characterization which is described in the final parts of this chapter.

2.6.1 Simulation of Nanohole Arrays

The finite-difference time-domain (FDTD) method was used to perform modeling of the electromagnetic field in order to numerically solve Maxwell's equations (FDTD Solutions, Lumerical Inc., Vancouver, Canada).

The FDTD calculations were performed by creating a 3D unit cell, as shown in Fig. SI.1b in Appendix B. This was achieved by simulating a 3D unit cell with a perfectly matched layer (PML) boundary condition on the z-axis and periodic boundary conditions on the x- and y-axis. A rectangular Cartesian-style mesh, with a maximum mesh setting of 3 nm, was positioned around the unit cell. Increasing the number of points within the mesh alters the mesh settings and increases the overall accuracy of the simulation.

In this thesis, the code found in the appendix was used to simulate any geometry of nanohole array. The code generates a GUI that allows a user to specify a range of hole sizes and geometries and simulate an array of geometries.

Once all the simulations are done the user can compare the results for different applications. This allows for the most optimized NHA to be fabricated later. As shown in Fig. 7, changing the hole size vs periodicity affects the SP excitation intensity.
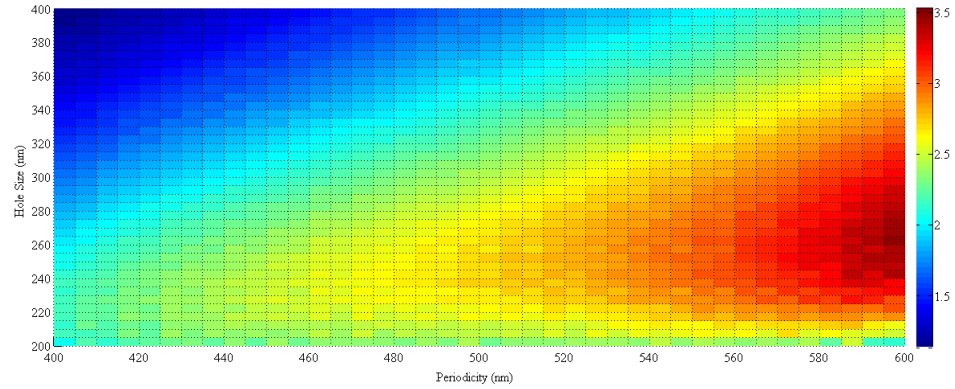
Figure 7 — Normalized intensity of NHAs for variable hole sizes and periodicities.
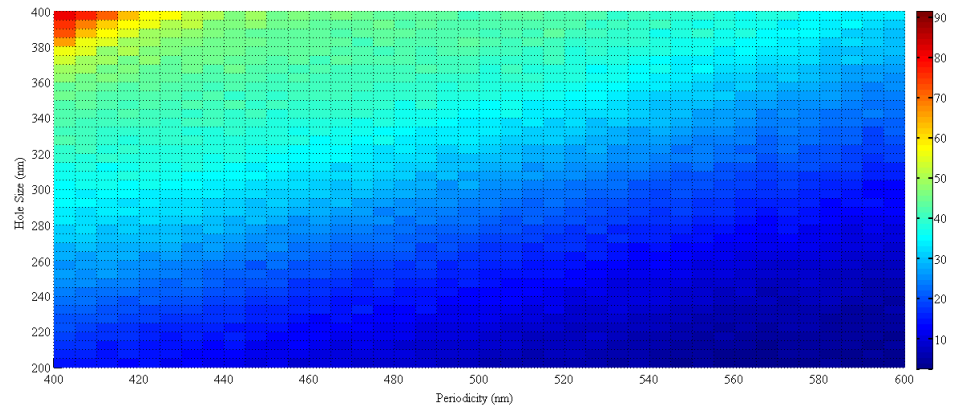
Figure 8 — Fullwidth at half maximum of NHAs for variable hole sizes and periodicities.

As shown in Fig.8, a relationship can be found for changing the hole size vs periodicity for the SP excitation bandwidth. These figures were the results of multiple simulations using the code provided in the appendix. They consisted of a NHA with circular holes and a gold thickness of 100 nm and air as the dielectric material (refractive index = 1). The results of these simulations can be used for applications such as multispectral filtering or creating a band pass filter.

2.6.2 Fabrication Methodology

Electron beam lithography (EBL) methodology was used to fabricate the plasmonic NHAs. To start, a thin 3 nm Ti layer was deposited on a Pyrex substrate using an electron-beam physical vapor deposition (EB-PVD), ensuring substrate surface conductivity required for the EBL writing process.

Then, a 500 nm thick layer of photoresist (negative tone photoresist ma-N 2403) was spin-coated onto the Ti layer which was then baked at 90 °C for 60 s. Nanohole array patterns were written on the photoresist layer of an EBL machine (LEO, 1530 e-beam lithography), where the sample was placed in preparation for development.

It was left in MF 319 developer (Shipley, Marlborough, MA, USA) for 40 s, leaving behind photoresist nanopillars, which acted as a mask to create the nanoholes in the metal film. Consequently, an adhesion layer was created by depositing a second 3 nm Ti layer followed by 100 nm Au, using an EB-PVD deposition instrument. NHAs were left behind in the Au film after the sample was left in PG Remover solution at 80 °C, lifting off the photoresist nanopillars.

2.6.3 Optical Characterization Setup

An inverted microscope (Nikon, TE300) attached to a photometer (PTI, D104),

monochromator (PTI, 101), and a photomultiplier (PTI, 710) were used to measure the

optical transmission spectra of the platforms. Unpolarized white light, produced by a

100 W halogen lamp, was focused onto the structure using a microscope equipped with a

bright-field condenser lens (N.A. = 0.3). The scattered light was then collected by a 20×

objective (N.A. = 0.45; Nikon, 93150) and guided to the photometer using a beam

splitter. Adjusting the apertures on the photometer allowed light from a specific region on

the sample to be collected and then guided to the monochromator for spectral analysis.

Background intensity (dark noise) corrections were made to the optical transmission

spectra which was consequently normalized by the intensity of the light source.

3   Tunable 3D Plasmonic Cavity Nanosensors for Surface-enhanced Raman Spectroscopy

We evaluated the SERS performance of a 3D metallic nanostructure composed of an array of nanoholes and co-registered nanocones embedded in a single cavity. The optical properties of the nanosensors were investigated experimentally and using optical field modeling. Three major features of these sensors are highlighted in this work: (i) plasmonic tunability; (ii) surface-enhanced Raman spectroscopy of 4-nitrothiophenol (4-NTP) covalently attached on these sensors, and finally (iii) limit of detection of 4-NTP adsorbed onto the sensors with fast acquisition time along with mapping the distribution of the molecules over the platform generating strong signals on the sensors based on the molecular fingerprint. Following are the related results and discussions.

3.1   Physical Characterization of the Fabricated 3D Plasmonic Cavity Nanosensors.

Scanning electron microscopy (SEM) images of the nanosensors are shown in Fig. 9. These sensors are composed of an NHA membrane with a co-registered nanocone array (NCA). As shown in Fig. 9a, this NHA-NCA platform consists of an NHA membrane in a 230 nm thick Au film on a Pyrex substrate with a 250 nm deep cavity, below the surface of the Au film.
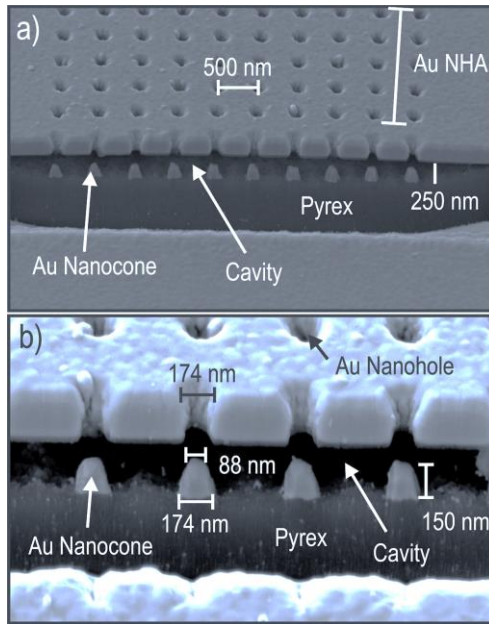
Figure 9 — SEM images of 3D plasmonic cavity nanosensors composed of a NHA membrane with co-registered NCA. (a) A 230 nm thick Au NHA membrane with 500 nm periodicity and 87 nm hole radius fabricated on a Pyrex substrate with a single 250 nm deep cavity. (b) Magnified image shown in (a) representing the dimensions of the truncated Au nanocones with an apex radius of 44 nm, a base radius of 87 nm, and a height of 150 nm.

It can be seen in Fig. 9b that at the bottom of the cavity, the co-registered truncated nanocones are aligned with the center of the nanoholes. The schematic representation of 3D plasmonic cavity nanosensors is shown in Fig. SI.1a. Demonstrated in Fig. 9b, a truncated cone has a height of 150 nm with an apex 100 nm away from the Au film. The hole sizes varied from 74 to 87 nm, and the periodicities varied from 425 to 500 nm with increments of 25 nm. A nanohole consists of two truncated nanocones with their apexes connected at the center of the nanohole. The apex of the cone has a 1:2 ratio with respect to the cone base diameter. For the simulations, the complex refractive indices of Au were provided by Palik, and a refractive index of 1.474 was used for Pyrex. [60]

3.1.1 Tunable Cavity 3D Nanosensors

In both simulated and experimentally measured optical transmission spectra of the 3D

nanosensors in Fig. 10, multiple transmission resonances were observed due to the SPP

corresponding to various scattering mode indices. A metallic NHA with a square lattice

arrangement of nanoholes results in momentum matching between the in-plane wave

vectors of the incident light and the SP, when $\vec{k}_{sp} = (\omega/c)\sin\theta \pm m\vec{u}_x \pm n\vec{u}_y$ is satisfied.

The expression $(\omega/c)\sin\theta$ is the in-plane component of the wave vector of the incident

light, where ω is the frequency of the incident light, c is the speed of the light, and θ is

the incident angle of light [56]. The reciprocal lattice wave vectors $\vec{u}_x$ and $\vec{u}_y$ describe a

square lattice when $|\vec{u}_x| = |\vec{u}_y| = (2\pi/p)$, where p is the spacing between adjacent

nanoholes and m and n are integers expressing the scattering mode indices. From the

conservation of energy, the SP dispersion relationship on a smooth metal surface can

be expressed as $|k_{sp}| = |k_0|[\varepsilon_m\varepsilon_d/(\varepsilon_m + \varepsilon_d)]$ where ε_d and ε_m are the dielectric functions

of the incident medium (at the top or bottom surface of the nanohole) and the metal film.

By combining the momentum-matching condition of the light-SP for light at normal

incidence to the NHA and the dispersion relation of the SP, the EOT positions of an NHA

associated with the SPP can be expressed by Eqn. 18:

$$\lambda_{max} \cong \frac{p}{\sqrt{m^2 + n^2}} \sqrt{\frac{\varepsilon_m \varepsilon_d}{\varepsilon_m + \varepsilon_d}} \qquad \textbf{Equation 12}$$

The simulated and experimentally measured optical trans-mission spectra of the platforms for various periodicities are shown in Fig. 10 for platforms surrounded by air (n = 1.00) or immersed in water (n = 1.33). When the structures are in air, both simulation and experimental results showed a single transmission resonance, which can be associated with the (−1, 0) excitation of the SP on the top and bottom surface of the NHA membrane.

However, this resonance has been also induced with the presence of a truncated nanocone at the bottom of the cavity. The apex of the truncated nanocone and the bottom of the nanohole generated a nanoantenna effect at the resonance wavelength, which generated a localized SP between two aforementioned nanosensors, resulting in the (−1, 0) resonance being related to not only SPPs but also LSPRs.

As the periodicity of the hole decreases, the resonance transmission of the 3D nanosensors are blue-shifted to shorter wavelengths (Figs. 10a and c). The existence of LSPR coupling was observed between the nanocone and nanohole in the simulation model, which resulted in generation of an antenna and strong hot spot within this area.
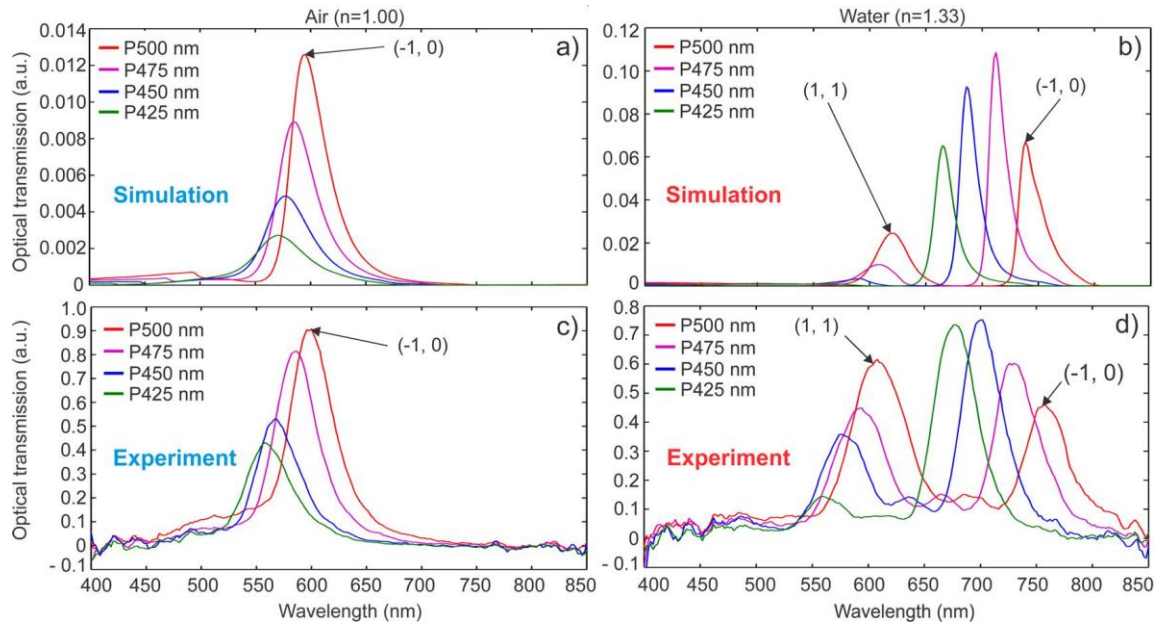
Figure 10 — Optical transmission spectra of 3D plasmonic nanosensors for simulated and experimental results. The periodicities range from 425 nm (green curve) to 500 nm (red curve) with increments of 25 nm. Simulated results for (a) air (n = 1.00) and (b) water (n = 1.33); experimental results for (c) air (n = 1.00) and (d) water (n = 1.33).

Although a nanocone structure without the presence of a nanohole could have two LSPRs located at the base and at the apex, the combination of both structures yields a strong local coupling of the respective LSPRs. The presence of a nanocone alters both the resonance frequency of the LSPRs and the transmission efficiency of a NHA due to the shadowing effect and optical absorption of the nanocone. [8]

However, a NHA without nanocones cannot generate a strong LSPR similar to the proposed structure and would have more limited detection and sensitivity in the SERS applications according to the previous studies on NHAs. [39], [40], [45]

Due to the bulk plasmon wavelength of Au at 500 nm, the resonance of the 3D nanosensors decays for smaller periodicity as the resonance blue-shifts toward 500 nm.

When the 3D nanostructure is encapsulated in water, the LSPR-SPP-mediated resonances of the 3D nanosensors are red-shifted toward longer wavelengths (Figs. 10b and d). Two LSPR-SPP resonances were seen in the optical transmission spectra of the 3D nanosensors. The resonances were associated with $(-1, 0)$ and $(1, 1)$ scattering hole orders of the 3D nanosensors.
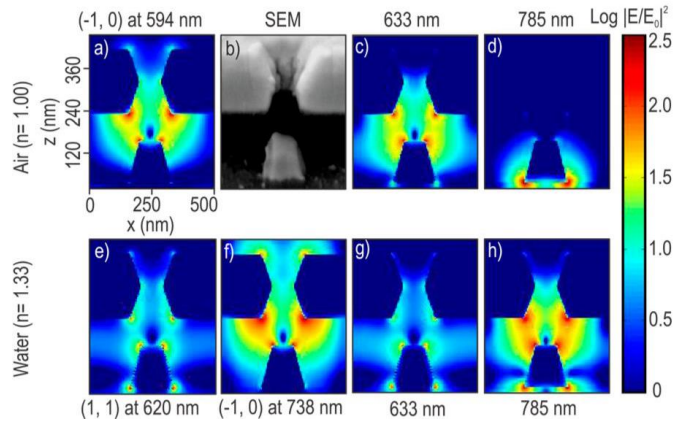
Figure 11 — Electric field ($|E/E0|2$, log scale representation) intensity of a unit cell in a 3D plasmonic nanosensor displayed on the xz plane. The electric field intensity for air (n = 1.00) at the (-1, 0) peak at (a) 594 nm, (c) 633 nm, and (d) 780 nm. The SEM image of the actual structure of represented simulated images is shown in (b). The electric field intensity for water (n = 1.33) at (e) the (1, 1) peak at 620 nm and (f) the (-1,0) peak at 738 nm, (g) 633 nm, and (h) 785 nm.

The electric field intensity of 3D nanosensors with 500 nm periodicity is shown in Fig. 11 at the LSPR-SPP resonance wavelengths of 633 and 785 nm for both air and water surrounding media. The electric field distributions at LSPR-SPP resonances for air and water confirm that there is a strong LSPR coupling between the bottom of the hole and the apex of the nanocone.

This structure generates the highest electric field at the resonance peak. However, the electric field at the (1, 1) LSPR-SPP resonance is of weaker intensity compared to the electric field at (−1, 0) resonance. The electric field at 633 nm appeared to be more intense in air, whereas it was lower when the platform was immersed in water.

This was due to the presence of the (−1, 0) resonance peak close to 633 nm for a 3D nanosensor with 500 nm periodicity located in air. In contrast, the electric field at 785 nm was significantly higher within the apex of the truncated cone and the bottom surface of the hole compared to that obtained in air at 785 nm.

There was a high absorption at the base of the truncated nanocone due to the LSPR absorption properties of the 3D nanosensor. Similar results are expected when the platform is immersed in a polar organic solvent such as ethanol (n = 1.36) based on its simulated optical transmission shown in Fig. SI2.
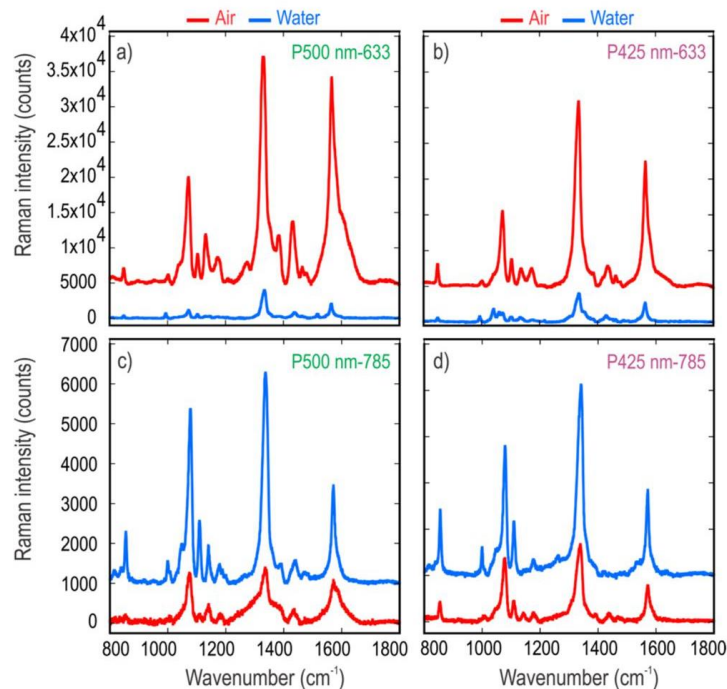
Figure 12 —— SERS spectra of 4-NTP adsorbed on the 3D nanosensors with different periodicities, medium (air and water), and wavelength of incident light. (a) P500 nm and (b) P425 nm periodicities at 633 nm incident light in air (red) and water (blue); (c) P500 nm and (d) P425 nm periodicities at 785 nm in air (red) and water (blue). Acquisition time for each spectrum was 3 s with five accumulations. Base line correction was applied to all spectra. A +5000 counts offset was applied to both red spectra in (a) and (b). A +1000 counts offset was applied to both blue spectra in (c) and (d). These offsets were applied to represent the data in a more comparable fashion.

3.1.2 Effect of Plasmonic Tunability on SERS

As shown in Fig. 12, the SERS spectra of the 4-NTP molecules (1 mM) were collected on different 3D nanosensors in two different media (air and water) and also for two wavelengths of incident light (633 and 785 nm). Using the 633 nm laser, the SERS signals of 4-NTP integrated for the vs NO_2 mode (1337 cm−1) were stronger for 3D nanosensors with periodicities of 500 (3.2×10^4 counts) and 425 nm (2.5×10^4 counts) when the signal was collected in air compared to water (Figs. 12a and b).

When the 785 nm laser was used, the SERS intensities of 4-NTP were stronger for both 3D

nanosensors, P500 (5.4×10^3 counts) and P425 (4.1×10^3 counts), when collected in water

compared to air (Figs. 12c and d). These phenomena are also related to the tuned plasmonic

bands of the 3D nanosensors in air and water as shown in Fig. 12.

We observed similar responses for 3D nanosensors with periodicities of 475 and 450 nm

(Fig. SI3). We also observed a decrease in the 4-NTP SERS signal when the periodicity

was decreased from 500 to 425 nm, which was related to the dependence of the plasmonic

bands on periodicity. For instance, from 500 to 425 nm, the plasmonic band is blue-shifted

to wavelengths below 600 nm in both simulations and experiment (Figs. 12a and c).

3.1.3 SERS Mapping of Hot Spots on 3D Plasmonic Nanosensors

In order to evaluate the detection limit of our 3D nanosensors, platforms were

functionalized with a 100 attomolar (aM) solution of the 4-NTP. The transmission

optical image of the array of P500 3D nanosensors is shown in Fig. 13a. The SERS

mapping was performed on the selected area in red shown in Fig. 13a. The map was

generated by integrating the intensity of the stretching mode of the nitro group (vs NO_2)

in the $1282 - 1400$ cm^{-1} spectral range.

A strong SERS intensity (bright regions) corresponded to the location of the 3D

nanosensors and, therefore, the location of the hot spots. This is the case for spot 1 in

Fig. 13b. However, regions away from the 3D nanosensors (labeled spot 2 in Fig. 13b)

show a considerably weaker SERS signal. This lack of enhancement was attributed to

positions containing only flat Au.

As shown in the inset of Fig. 14a, the relationship between the location of the 3D

nanosensors in the optical image and the locations of strong SERS intensity was

maintained. As a result, the detection of 4-NTP drop-casted onto the 3D nanosensors

was possible even at a concentration of 100 aM and with a rapid acquisition time of 1 s.
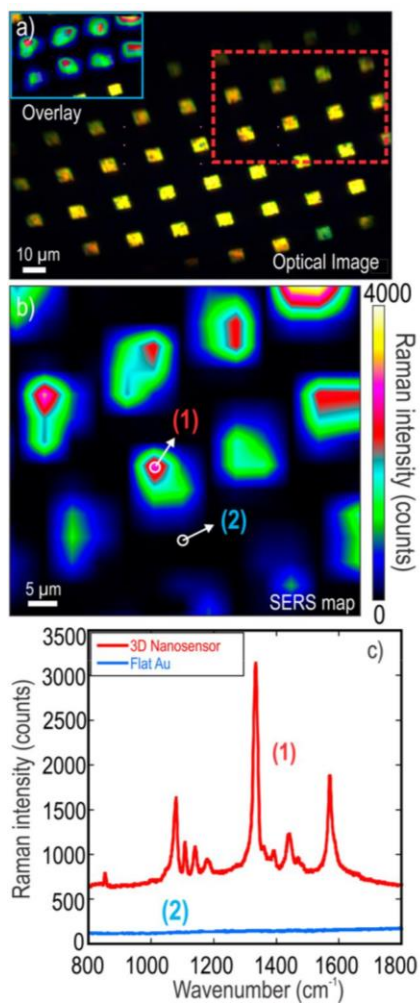
Figure 13 — Surface-enhanced Raman mapping of 4-NTP adsorbed on the 3D nanosensors with 500 nm periodicity in air with 633 nm incident light. Acquisition time for each spectrum was 1 s with a 1 μm step size. (a) Transmission optical image of 3D nanosensors with overlaid SERS mapping (inset) for the area outlined with a red dashed box. (b) Raman mapping of the outlined area in panel (a). (c) Spectra of the regions marked (1) and (2) in panel (b). No baseline correction was applied to spectra in panel (c).

The distinguishable locations of the 3D nanosensors based on the Raman map proved the reproducible ability of the sensors to generate a strong signal for low concentrations of molecules trapped in the nanoscale hot spots. Noteworthy, as stated previously, the engineered 3D nano-sensors allow for coupling of SPP and LSPR, which generates strong hot spots between nanoholes and nanocones. Furthermore, the 3D structure of nanosensors potentially increases the surface area for attachment of probe molecules to the surface of the nanostructure compared to a planar structure.

This effect has been observed in other studies for SERS substrates compared to a 2D array of nanosensors. [38] For instance, in this case, the 3D nanosensors have surface areas on both top and bottom surfaces of a gold NHA membrane as well as on the nanocone itself compared to the planar NHA structure.

3.1.4 Limit of Detection for 3D Nanosensors

To evaluate the limit of detection of such cavity-based sensors, the platforms were functionalized with 4-NTP at concentrations between 1 μM and 1aM. To avoid cross contamination between high and low concentration experiments, each SERS experiment was repeated 3 to 5 times onto freshly prepared arrays of 3D nanosensors (P500−P425). Furthermore, the experiments were conducted for an average of 10 to 15 spots on each platform. Fig. 14a shows that all the main peaks of the 4-NTP were detectable between 1 μM and 100 aM. [61]
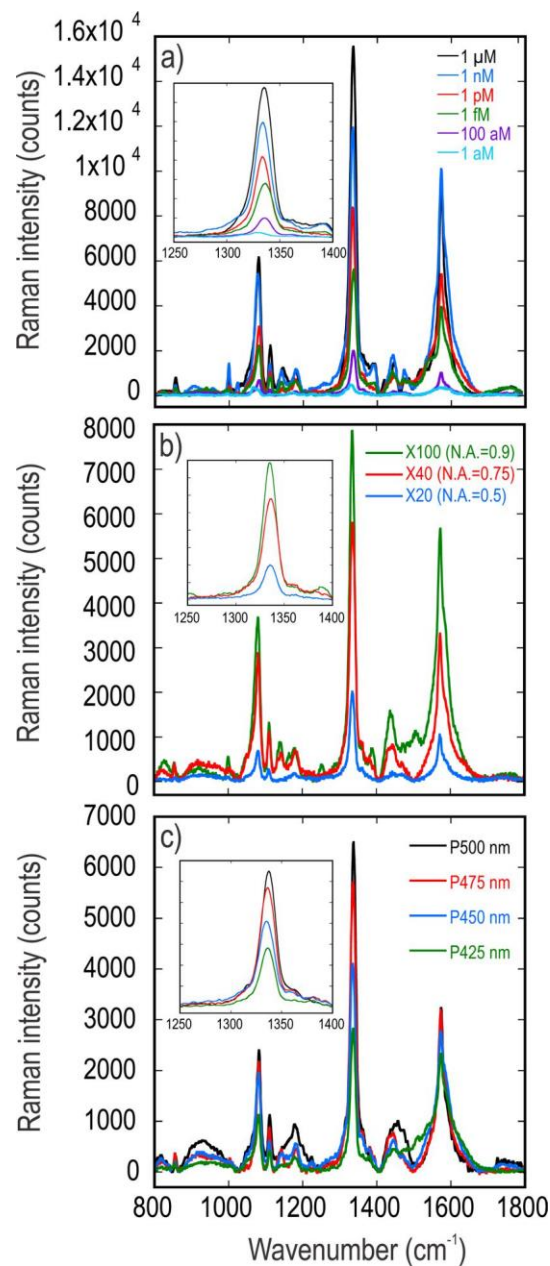
Figure 14 — SERS spectra of 4-NTP adsorbed onto 3D nanosensors collected by using a 633 nm incident laser in air. (a) Different concentrations (1 aM to 1 mM) of 4-NTP adsorbed on the 3D nanosensors with 500 nm periodicity. (b) The effect of numerical aperture and magnification on SERS spectra of 100 aM 4-NTP absorbed on the 3D nanosensors. (c) SERS spectra of 100 aM 4-NTP adsorbed on the 3D nanosensors. Baseline correction was applied to all spectra. SERS signals of the main NO_2 peak are shown within each inset in each panel.

However, we observed a small but measurable change in the intensity of the SERS signal for 1aM 4-NTP, even though at this concentration it was statistically unlikely to find a spot with a single or a few molecules trapped in the plasmonic cavity of the 3D nanosensors.

Compared to higher concentrations of 4-NTP, there were fewer spots on the 3D nanosensors that provided a SERS signal, and the signals were not stable over long exposures. In most of the 2D plasmonic substrates for SERS, providing a reproducible global signal requires at least a homogeneous monolayer of the probe molecule attached onto the surface. [44] The advantage of nanostructures with an embedded cavity can be highlighted here, as they provide a better opportunity to trap the molecule in the nanoscale hot spots compared to equivalent 2D structures.

A reliable Raman signal collected from these 3D nanosensors was obtained for concentrations down to 100 aM. This can be clearly observed by evaluating the intensity of the main peak of NO_2 (Fig. 14a). Comparing the signal at 100 and 1 aM, it is apparent that the signal has mostly vanished for 1 aM. These measurements yield a limit of detection of ~100 aM (Fig. 14a).

Since altering the conditions of the experiment plays a key role in obtaining the SERS signal for different structures, the measurements for 100 aM 4-NTP were repeated with microscope objectives of different numerical apertures (N.A.). Increasing the N.A. of the objective resulted in an enhanced SERS signal (compare the main peak of NO_2 in Fig. 14b.

The SERS signals were enhanced almost 2 times when increasing the N.A. from 0.5 to 0.75 and 3 times when increasing the N.A. up to 0.9. By increasing the N.A. of the microscope objective, the laser beam was more confined at the apex of the nanocone and the bottom of the nanohole, resulting in a more efficient hot spot and LSPR. It can also be beneficial to decrease the laser spot even further to be more focused on the 3D nanosensors, thereby excluding the scattering from flat Au regions around the hot spots.

To evaluate the sensitivity of different 3D nanosensors based on their periodicities, the SERS signals have been collected with the same concentration of 100 aM. As shown in Fig. 14c, a decreasing trend was observed for the SERS signal when the periodicity of the platforms was decreased from 500 nm to 425 nm. These results have a similar trend to measurements performed with 1 mM 4-NTP.This trend was clearly observed, as shown in the inset of Fig. 14c.

3.1.5 Estimation of a SERS Enhancement Factor

Generally speaking, the definition of the SERS EF can be considered as the ratio between the SERS intensity per adsorbed molecule and the normal Raman intensity per bulk molecule. However, in SERS, the EF for a given molecule varies with the opto- geometric conditions of the SERS measurement and corresponding reference measurement [62]. The determination of the number of molecules that yield the Raman signal and their contribution to the EF is not trivial and may lead to erroneous estimations. The ensemble of parameters that need to be considered when performing a SERS experiment, such as probing a single molecule or multiple molecules, the orientation of the molecules in the experimental system, the spatial distribution, or the experimental limitations in resolution, can be used only to approximate

an EF. The Raman signal is enhanced through both the excitation and the emission processes, as shown in Eqn. 19. [57]

$$F = \left|(E_{v_{\text{excitation}}})\right|^2 \left|(E_{v_{\text{Raman}}})\right|^2 \qquad\qquad \textbf{Equation 13}$$

where $E(v_{\text{excitation}})$ and $E(v_{Raman})$ are the local electric-field EFs at the incident frequency ($v_{\text{excitation}}$) and at the Raman Stokes frequency (v_{Raman}), respectively. However, since the plasmon frequency width is large compared to the Raman Stokes shift, both electromagnetic fields are pre-resonance with the plasmon band. Therefore, an approximation is to assume that $E(v_{\text{excitation}})$ and $E(v_{Raman})$ same, leading to an EF proportional to $F = |\ E(v_{\text{excitation}})|^4$.

In such an approximation, the matching of the excitation laser line with the plasmon frequency is an essential condition to obtain large Raman surface enhancements. In order to establish the relationship between the nanostructured surface and the SERS activity of the platform, the EFs have been determined. The determination of the EF in SERS is a prerequisite to quantify the enhancement of the Raman signal. The surface Raman EF can be estimated by comparing the measured SERS intensities nonenhanced (INE) as shown in Eqn. 20 [58], [63].

$$EF = \frac{N_{NE} \times I_{SERS}}{I_{NE} \times N_{SERS}} = 1.2 \times 10^7 \qquad\qquad \textbf{Equation 14}$$

These 3D nanosensors also provide a remarkable molecular limit of detection of 10^{-16} M for a probe molecule (4-NTP) with a short acquisition time of 1 s. Consequently, a reliable EF of $\sim 10^7$ is achieved for these sensors for an extremely low concentration of 100 aM from a femtoliter plasmonic probe volume.

Reproducible SERS signals have been collected on the 3D nanosensors with concentrations down to 100 aM, providing the spatial distribution of hot spots on the plasmonic substrate. It is also shown that by increasing the N.A. of the objectives, an enhancement occurs for the SERS signals obtained on these sensors, proving the confined strong LSPR coupling in the NHA-NCA interface. The strong LSPR coupling of these nanosensors can introduce them to other spectroscopic techniques such as SEF, SEIRA, and even tip-enhanced Raman spectroscopy (TERS), in which there is better control over the polarization of light.

Of even greater interest, the plasmonic tunability of these sensors can be used for simultaneous optical trapping and surface-enhanced detection.

3.2   Methods

3.2.1 Fabrication of 3D Plasmonic Cavity Nanosensors

The plasmonic cavities were fabricated using electron beam lithography (EBL) methodology. First, electron-beam physical vapor deposition (EB-PVD) was used to deposit a 3 nm thin Ti layer on a Pyrex substrate. This ensured that the substrate surface was conductive for the EBL writing process.

A 500 nm thick layer of photoresist (negative tone photoresist ma-N 2403) was then spin-coated onto the Ti layer and soft baked at 90 °C for 60 s. The sample was placed into an EBL machine (LEO, 1530 e-beam lithography), where the nanohole array patterns were written on the photoresist layer.

The sample was developed in MF 319 developer (Shipley, Marlborough, MA, USA) for 40 s, leaving behind photoresist nanopillars, which acted as a mask to create the nanoholes in the metal film. Another 3 nm thick Ti layer was deposited to create an adhesion layer followed by 80 nm deposition of Au using an EB-PVD deposition instrument.

Once the Au layer was deposited, the sample was left in PG Remover solution at 80 °C to lift off the photoresist nanopillars and leave behind the NHAs in the Au film. Once the NHAs were created, a TFT Ti etchant (Transene Company, Inc.) was used to etch away both the Ti layer and Pyrex, forming a large cavity beneath the gold NHA. The sample was in Ti etchant for 70 s and resulted in a 250 nm deep cavity. Afterward, 150 nm Au was deposited onto the structure to create a truncated nanocone beneath each nanohole on the bottom surface of the cavity.

The SEM images of the fabricated 3D plasmonic nanosensors with 500 nm periodicity are shown in Fig. 9. The presence of the 250 nm deep cavity and 150 nm tall truncated NCA beneath the NHA membrane structure is shown in these SEM images. Each 3D nanosensor had dimensions of approximately 5 µm by 5 µm and was repeated in a 7 by 7 square lattice arrangement with a periodicity of 10 µm. In order to clean the platform for further use, O_2 plasma and UV-O_3 exposure are efficient methods. The substrate can also be cleaned by Nanostrip (90% sulfuric acid, 5% peroxymonosulfuric acid, <1% hydrogen

peroxide, and 5% water) to remove all the impurities and subsequently washed with ultrapure Milli-Q water and dried under nitrogen prior to O_2 or UV-O_3 cleaning.

SERS Measurements and Sample Preparation. The Raman measurements were performed using a Horiba Jobin-Yvon Raman spectrometer equipped with a 600 g/mm grating and a 632.8 or 785 nm excitation with proper interference and edge filters. For both laser sources, intensities were set to 2 mW or 200 μW at the sample using neutral density filters with 1.0 or 2.0 optical densities, respectively. Olympus microscope objectives of 20× (N.A.= 0.5), 40× (N.A.= 0.75), and 100× (N.A.= 0.9) were used for all experiments.

The pinhole of the spectrometer was opened to 200 μm. All the Raman spectra collected for individual spots were the result of 3 s exposures, while the maps were the result of 1 s exposures. The maps were integrated within 1316 to 1354 cm^{-1}. A stock solution of 4-NTP (10^{-3} M) in ethanol was made. This stock solution was then further diluted to yield 2 mL of solutions with concentrations ranging from 10^{-6} to 10^{-18} M.

Two drops of the as-prepared solution (∼100 μL) were deposited onto one platform and then placed into a Petri dish. All glassware used for functionalization and washing were new to avoid contamination. The Petri dish was sealed and stored in the refrigerator for the duration of the functionalization. For the determination of limit of detection, the platforms were functionalized overnight (24 h). Each platform was then washed into a beaker of ethanol (99.9%) three times to remove any excess 4-NTP not adsorbed onto the surface.

The platforms were then dried under nitrogen. Each SERS measurement was performed 3−5 times. The spectra of 10−15 spots were collected on each 3D nanosensor, and the average value of the intensities was used in all relevant graphs (Fig. SI4).

3.2.2 Numerical Simulation of 3D Plasmonic Cavity Nano-sensors

Modeling of the electromagnetic field was performed using the finite-difference time-domain (FDTD) method to numerically solve Maxwell' s equations (FDTD Solutions, Lumerical Inc., Vancouver, Canada).

As shown in Fig. SI.1b, FDTD calculations were performed by creating a 3D unit cell that was simulated with periodic boundary conditions on the x- and y-axis, and a perfectly matched layer (PML) boundary condition on the z-axis. A rectangular, Cartesian-style mesh was placed around the unit cell with a maximum mesh setting of 3 nm. The mesh settings can be altered to increase the accuracy of the simulation by increasing the number of points within the mesh.

3.2.3 Optical Characterization Setup

The optical transmission spectra of the platforms were measured, using an inverted microscope (Nikon, TE300) attached to a photometer (PTI, D104), monochromator (PTI, 101), and a photomultiplier (PTI, 710). A 100 W halogen lamp produced unpolarized white light, which was focused onto the structure using a bright-field condenser lens (N.A. = 0.3) on the microscope.

A 20× objective (N.A. = 0.45; Nikon, 93150) was used to collect the scattered light, which was then guided to the photometer using a beam splitter. Light from a desired region on the sample was selected by adjusting the apertures on the photometer.

The light from this desired region was then guided to the monochromator for spectral analysis. The optical transmission spectra were corrected for the background intensity (dark noise) and normalized by the intensity of the light source.

3.2.4 SERS Measurements and Sample Preparation

The Raman measurements were performed using a Horiba Jobin-Yvon Raman spectrometer equipped with a 600 g/mm grating and a 632.8 or 785 nm excitation with proper interference and edge filters. For both laser sources, intensities were set to 2 mW or 200 μW at the sample using neutral density filters with 1.0 or 2.0 optical densities, respectively.

Olympus microscope objectives of 20× (N.A.= 0.5), 40× (N.A.= 0.75), and 100× (N.A.= 0.9) were used for all experiments. The pinhole of the spectrometer was opened to 200 μ m. All the Raman spectra collected for individual spots were the result of 3 s exposures, while the maps were the result of 1 s exposures. The maps were integrated within 1316 to 1354 cm^{-1}. A stock solution of 4-NTP (10^{-3} M) in ethanol was made.

This stock solution was then further diluted to yield 2 mL of solutions with concentrations ranging from 10^{-6} to 10^{-18} M. Two drops of the as-prepared solution (~100 μL) were deposited onto one platform and then placed into a Petri dish. All glassware used for functionalization and washing were new to avoid contamination.

The Petri dish was sealed and stored in the refrigerator for the duration of the functionalization. For the determination of limit of detection, the platforms were functionalized overnight (24 h). Each platform was then washed into a beaker of ethanol (99.9%) three times to remove any excess 4-NTP not adsorbed onto the surface. The platforms were then dried under nitrogen.

Each SERS measurement was performed 3−5 times. The spectra of 10^{-15} spots were collected on each 3D nanosensor, and the average value of the intensities was used in all relevant graphs (Fig. SI4).

3.3   Conclusions

In this work, for the first time, the capability of cavity-based plasmonic Nanosensors is demonstrated for SERS-based molecular sensing. These nanosensors provide extraordinary optical transmission properties, which can generate strong SPP and LSPR coupling. These phenomena have been shown here by simulated and experimental optical transmission measurements.

The experimental results were also in good agreement with the FDTD calculations for electromagnetic field distributions at the plasmonic bands of the nanosensors. In the meantime, these structures represent a plasmonic tunability with respect to the media of the experiment as well as the wavelength of the incident light.

4 Study of Absorption Coefficient of Nanohole Array Metamaterials

In this chapter, we have investigated the absorption coefficient experimentally and theoretically in metallic metamaterials made from an array of split ring resonators [56]. The split ring resonator array is deposited on a dielectric Pyrex substrate. The SPPs were found at the interface between the split ring resonators and the substrate. The absorption coefficient spectrum was measured for one sample having a unique split ring resonator radius and periodicity. Each measured spectrum had several peaks due to SPPs.

The transmission line theory of metamaterials and Bloch's theorem [50] was used to calculate SPP energies. The transmission and absorption coefficients were calculated using the transfer matrix method. The experimental and theoretical results agreed well. It was found that the locations of spectral peaks were dependent on the array periodicity and radii of the split ring resonators.

4.1 Surface Plasmon Polaritons in Metamaterials

Generally, the transverse magnetic (TM) field of light is responsible for the SPP modes at the interface of metallic heterostructures [31], [59], [64]. The H field describes the TM modes. Referring to Fig. 15, let us consider that the interface between the metamaterial and dielectric lies in the yz-plane and is located at $x = 0$. The QEs are doped at the interface. We consider that y and z directions are symmetric.
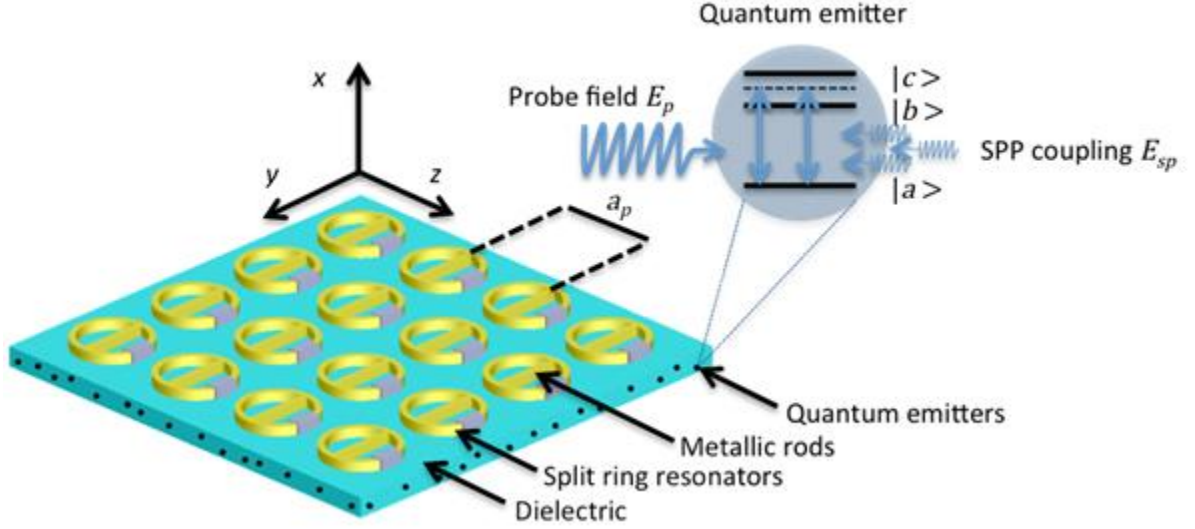
Figure 15 — A schematic diagram of the Quantum emitters (QE) and metamaterial system. The metamaterial was fabricated from a split ring resonator (SRR) and metallic rod unit cell, where each cell was deposited on top of a dielectric material. Here ap is the periodicity of the metamaterial lattice. QEs were deposited at the interface between the metamaterial and the dielectric substrate. The QE had three levels denoted as |a>, |b>, |c>. A probe field Ep was applied to excite the QEs and SPP field Esp.

The dielectric constant and magnetic permeability of the dielectric material are denoted as ε_d and μ_d, respectively. Similarly, the dielectric constant and permeability for the metamaterial are denoted as ε_m and μ_m, respectively. Expressions for ε_m and μ_m, have been obtained in reference [65] for metamaterials fabricated from split ring resonators and metallic rods. Their expressions are:

$$\varepsilon_m = \left(1 - \frac{\omega_p^2}{\omega^2 + i\gamma_m\omega}\right), \qquad \omega_p = \sqrt{\frac{2\pi c^2}{a_p^2 \ln(a_p/r_p)}}$$

Equation 15

where

$$\mu_m = \left(1 - \frac{F\omega^2}{\omega^2 - \omega_m^2 + i\gamma_m\omega}\right), \qquad F = \pi r_p^2 / a_p^2$$

Equation 16

Here, ω_p is called the plasmon frequency. Similarly, ω_m is called the magnetic plasmon frequency where c is the speed of light, a_p is the periodicity of the lattice and r_p is the radius of the rods. Note that ε_m has a negative value for $\omega < \omega_p$ and similarly μ_m has negative value at $W < W_m / \sqrt{1-F}$.

$$\nabla^2 H_y(x,z) = (\frac{\omega}{c})^2 \varepsilon_d H_y(x,z) \qquad x > 0$$ **Equation 17**

and

$$\nabla^2 H_y(x,z) = (\frac{\omega}{c})^2 \varepsilon_m H_y(x,z) \qquad x < 0$$ **Equation 18**

The TM modes near the interface can be found as:

$$H_y(x,z) = H_p e^{-ik_z z} e^{\kappa_{mx} x} \quad x > 0$$ **Equation 19**

and

$$H_y(x,z) = H_p e^{-ik_z z} e^{\kappa_{dx} x} \quad x < 0$$ **Equation 20**

where

$$\kappa_{mx} = \sqrt{\beta^2 - \frac{\omega^2 \varepsilon_m \mu_m}{c^2}}$$ **Equation 21**

and

$$\kappa_{dx} = \sqrt{\beta^2 - \frac{\omega^2 \varepsilon_d \mu_d}{c^2}}$$ **Equation 22**

where β and κ_{mx} and κ_{dx} are wave vectors of light along z and x directions, respectively.

Note that the TM wave is propagating along the zy-plane and decays perpendicular to the interface. Using the boundary conditions at the interface x = 0 for the TM wave we get the following expression after some mathematical manipulation:

$$b = \frac{w}{c}\sqrt{\frac{e_m e_d \left(e_m m_d - e_d m_m\right)}{\left(e_m^2 - e_d^2\right)}}$$

Equation 23

The above expression is the dispersion relation for SPP modes at the interface. The electric field produced by SPPs along the x direction in the dielectric is calculated as:

$$\mathbf{E}_{sp} = \frac{1}{i\omega\varepsilon_d}\frac{d\mathbf{H}_{dy}}{dz} \quad \text{from Eqn. 25 and found as:}$$

$$\mathbf{E}_{sp} = a_{sp}\left(\mathbf{E}_p + \mathbf{E}_q\right)e^{k_{dx}x}$$

Equation 24

where $\qquad a_{sp} = \sqrt{\frac{e_m e_d \left(e_m m_d - e_d m_m\right)}{\left(e_m^2 - e_d^2\right)}}$

Equation 25

and $\qquad k_{dx} = \frac{w}{c}\sqrt{\frac{e_m e_d \left(e_m m_d - e_d m_m\right) - e_d m_d \left(e_m^2 - e_d^2\right)}{\left(e_m^2 - e_d^2\right)}}$

Equation 26

4.2   Results and Discussions

In this section, we considered the metamaterial to be fabricated from gold with SPP energy.

$$\varepsilon_{sp} = \hbar\omega_{sp} = 1.9eV$$
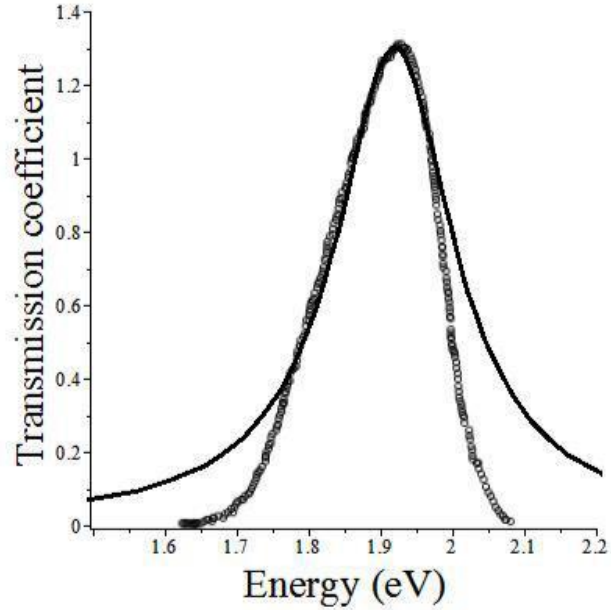
Figure 16 — The transmission spectra of nanohole arrays with circular holes for experimental (dotted line) and theoretical results (solid line). The holes in the nanohole array have a diameter of 150 nm, a periodicity of 400 nm, and a 100 nm thick gold film.

Now we compare our theory of SPPs with our recent experiment in Fig. 16. We used the same theory as proposed in this chapter to calculate the transmission coefficient of a nanohole array (NHA). The results are presented in Fig. 16. The circular holes are for experimental results and the dotted line is for theoretical results. This NHA was fabricated using Electron Beam Lithography (EBL).

Our theory does not agree at lower or higher energies. It may be due to the scattering

of photons and phonons in the NHA. We have also not calculated the decay rate of SPPs

using the perturbation theory. Finally, nanoholes are not perfectly circular and their

radius are not exactly the same. It is also noted that the periodicities of the NHA are also

not constant.

The NHA consisted of an array of holes with a diameter of 150 nm and a periodicity of

400 nm in a 100 nm gold sheet. The gold was deposited onto a 4 nm titanium (adhesion)

layer which was deposited onto a Pyrex substrate using electron beam physical

vapor deposition.

To optically characterize this NHA, we used optical transmission spectroscopy [14].

One can see that there is a good agreement between the experimental results and the

theoretical results.

We would like to make comments on our theory. This theory was developed for SPPs

located at the interface between a dielectric slab and a metamaterial slab. In other words,

we have calculated SPPs for 2-dimensional hybrid systems. This theory cannot be applied

to 3-dimensional hybrid systems fabricated from depositing spherical dielectric material

on the top of the spherical metamaterial. In this case, SPPs are localized in all three

directions.

Recently Feng et al. [66] have proposed a broadband infrared absorber by engineering

the frequency dispersion of the metamaterial surface. They have demonstrated that the

absorption bandwidth in metamaterials can be dramatically enhanced through utilizing

the metamaterial surface to mimic the dispersion of an ideal absorbing sheet. Pu et al. [67] have also studied the transmission of light in planar metamaterials with perturbed periodicity and found an enhancement in Fano resonances in the transmission coefficient.

In these two papers, authors have studied absorption and emission in metamaterials. Whereas in the present paper we have studied the effect of metamaterials on the absorption in the quantum emitters. The absorption bandwidth in quantum emitters can be increased by dispersion engineering and multiple Fano resonances in metamaterials as discussed in the above papers.

5   **Effect of Quantum Interference**

In this chapter, we report the effect of quantum interference on the absorption of light in a quantum emitter and metamaterial system. The system was comprised of a dielectric substrate doped with quantum emitters and metallic split ring resonators that included metallic rods. At the interface between the dielectric substrate and the metal are surface plasmon polaritons; these interact with excitons, which are present in quantum emitters.

Quantum interference occurs due to the interaction between excitons and surface plasmon polaritons. It is also considered that excitons decay from an excited state to the ground state due to the radiative and nonradiative decay processes. The quantum interference phenomenon occurs between excitons decay rates. The density matrix method is used to calculate the absorption of light in the presence of both radiative and nonradiative processes. It is found that there is a decrease in the absorption of light by metamaterial hybrids due to quantum interference.

There is also an increase in the absorption of light when the resonant frequencies of two excitons are in resonance with the surface plasmon polariton. Absorption peaks are shifted and broadened due to the surface plasmon polariton coupling. These findings suggest that the optical absorption properties of a metamaterial hybrid can be tuned by doping the supporting substrate with quantum emitters.

5.1 Effect of Quantum Interference on Absorption of Light in Metamaterial Hybrids

In this work, an ensemble of QEs was deposited at the interface between a metamaterial and a dielectric material. The concentration of QEs was assumed to be low enough such that interaction between QEs could be neglected. A probe field was applied to monitor the absorption of light by the hybrid system. A schematic diagram of the system is shown in Fig. 15. It is considered that the quantum emitters have two excitonic states.

The excitonic states interacted with the SPPs resulting in interference. The SPPs were calculated in the metallic hybrid using the transfer matrix method. We consider that two excitons decay to the ground state due to the radiative and nonradiative process. In the radiative process the excitons lose energy due to the spontaneous process. On the other hand, in the nonradiative process the excitons lose energy to the metamaterial due to exciton and SPP coupling.

The quantum interference phenomenon occurs when two exciton decay rates interfere with each other. The density matrix method was used to calculate the absorption of light in the presence of exciton-SPP interaction, along with radiative and nonradiative processes. It was found that the absorption of light decreases under certain conditions due to the quantum interference effect. We also found an enhancement in the absorption of light when the resonance frequencies of two excitons were in resonance with the SPP frequency. Absorptions peaks were shifted and broadened due to the SPP coupling.

5.2 Exciton-surface plasmon-polariton interaction

In this section, we calculate the exciton and SPP coupling. We consider that the QE contains three levels which are denoted as $|a\rangle$, $|b\rangle$ and $|c\rangle$ with energies ω_a, ω_b and ω_c, respectively. Two exciton frequencies due to transitions $|a\rangle \leftrightarrow |b\rangle$ and $|a\rangle \leftrightarrow |c\rangle$ are denoted as ω_{ab} and ω_{ac}, respectively. The Hamiltonian of the excitons in the QE can be written as:

$$H_{EX} = \hbar\omega_a\sigma_{aa} + \hbar\omega_b\sigma_{bb} + \hbar\omega_c\sigma_{cc}$$

Equation 27

where

$$\sigma_{ii} = |i\rangle\langle i| \text{ with i = a,b,c.}$$

Equation 28

We applied the probe field with amplitude E_p and frequency ω to monitor the absorption between the transitions $|a\rangle \leftrightarrow |b\rangle$ and $|a\rangle \leftrightarrow |c\rangle$. This field induces polarization $\mathbf{P}_q$ in the QE due to these transitions. This in turn produces a dipole field $\mathbf{E}_q$ at distance R from the QE and it is found as: [59], [64]

$$\mathbf{E}_{sp} = \alpha_{sp}\left(\mathbf{E}_p + \mathbf{E}_q\right)e^{\kappa_{dx}x}$$

Equation 29

where

$$\alpha_{sp} = \sqrt{\frac{\varepsilon_m\varepsilon_d\left(\varepsilon_m\mu_d - \varepsilon_d\mu_m\right)}{\left(\varepsilon_m^2 - \varepsilon_d^2\right)}}$$

Equation 30

and

$$\kappa_{dx} = \frac{\omega}{c} \sqrt{\frac{\varepsilon_m \varepsilon_d (\varepsilon_m \mu_d - \varepsilon_d \mu_m) - \varepsilon_d \mu_d (\varepsilon_m^2 - \varepsilon_d^2)}{(\varepsilon_m^2 - \varepsilon_d^2)}}$$

Equation 31

In the above expression, we have considered that the electric field falling at the interface is due to the probe field E_p and also the dipole field equation produced by the QE. The above expression is simplified for metamaterials made of metallic rods only. In this case, we have $\mu_d = \mu_m = 1$. Eqn. 32 reduces to:

$$\mathbf{E}_{sp} = \alpha_{sp} (\mathbf{E}_p + \mathbf{E}_q) e^{\kappa_{dx} x}$$

Equation 32

where

$$\alpha_{sp} = \sqrt{\frac{\varepsilon_m \varepsilon_d (\varepsilon_m - \varepsilon_d)}{(\varepsilon_m^2 - \varepsilon_d^2)}} = \sqrt{\frac{\varepsilon_m \varepsilon_d}{(\varepsilon_m + \varepsilon_d)}}$$

Equation 33

and

$$\kappa_{dx} = \frac{\omega}{c} \sqrt{\frac{\varepsilon_m \varepsilon_d - \varepsilon_d (\varepsilon_m + \varepsilon_d)}{(\varepsilon_m + \varepsilon_d)}} = \frac{\omega}{c} \sqrt{\frac{\varepsilon_d^2}{(\varepsilon_m + \varepsilon_d)}}$$

Equation 34

Note that at $\mathrm{Re}(\varepsilon_m) = \varepsilon_d$ the α_{sp} function has a large value. This condition gives the SPP frequency ω_{sp} which is found as $W_{sp} = W_p / \sqrt{(1 + e_d)}$.

$$\mathbf{E}_q = \frac{g_l \mathbf{P}_q}{4\pi\varepsilon_0\varepsilon_f R^3} = \frac{g_l\left(\mathbf{\mu}_{ab}\rho_{ab} + \mathbf{\mu}_{ac}\rho_{ac}\right)}{4\pi\varepsilon_0\varepsilon_f R^3} + c.c. \qquad \text{Equation 35}$$

Here ε_f is the effective dielectric constant, and c.c is a complex conjugate. We put

$\mathbf{P}_q = \mathbf{\mu}_{ab}\rho_{ab} + \mathbf{\mu}_{ac}\rho_{ac} + c.c.$ in the above expression. The constant g_l is called the

polarization parameter and it has values $g_l = -1$ and $g_l = 2$ for $\mathbf{P}_q \| \mathbf{E}_p$ and $\mathbf{P}_q \perp \mathbf{E}_p$,

respectively. Here μ_{ij} and ρ_{ij} are the dipole moment and density matrix element,

respectively for the transition $|i\rangle \leftrightarrow |j\rangle$. Putting Eqn. 41 into Eqn. 38 we get the SPP

electric field as:

$$\mathbf{E}_{sp} = \alpha_{sp}\mathbf{E}_p e^{-k_{sp}R} + \frac{\left(\mathbf{\mu}_{ab}\alpha_{sp}g_l e^{-k_{sp}R}\right)}{4\pi\varepsilon_0\varepsilon_f R^3}\rho_{ab} + \frac{\left(\mathbf{\mu}_{ac}\alpha_{sp}g_l e^{-k_{sp}R}\right)}{4\pi\varepsilon_0\varepsilon_f R^3}\rho_{ac} \qquad \text{Equation 36}$$

Note that the SPP field contains three terms. The first term is the induced SPP field due

to the external probe field $\mathbf{E}_p$. The second term is the induced SPP field due to the QE

dipole field for transition $|a\rangle \leftrightarrow |b\rangle$. The last term is the induced SPP field due to the QE

dipole field for transition $|a\rangle \leftrightarrow |c\rangle$.

The interaction of the excitons with SPPs is calculated as follows. The QE feels the

influence of the probe electric field $\mathbf{E}_p$ and the SPP field $\mathbf{E}_{sp}$. They induce excitons

transitions $|a\rangle \leftrightarrow |b\rangle$ and $|a\rangle \leftrightarrow |c\rangle$ in the QE. Hence the induced dipoles due to these

two transitions in QE interact with these two electric fields.

The exciton-SPP interaction Hamiltonian in the second quantized notation is expressed

in the dipole and the rotating wave approximation as:

$$H_{int} = -\sum_{n=b,c} \mu_{na}.\left(\mathbf{E}_p + \mathbf{E}_{sp}\right)\sigma_{na}^\dagger + h.c.$$

Equation 37

where h.c. stands for the Hermitian conjugate and $\sigma_{na}^+ = |b\rangle\langle a|$ is the exciton creation
operator. Putting the expressions $\mathbf{E}_{sp}$ from Eqn. 42 into Eqn. 43 we get:

$$H_{int} = H_{ex-p} + H^p_{ex-sp} + H^q_{ex-sp}$$

Equation 38

where

$$H^p_{ex-sp} = \Pi_b\sigma_{ba}^\dagger + \Pi_c\sigma_{ca}^\dagger + h.c.$$

Equation 39

and

$$H_{ex-p} = \Omega_b\sigma_{ba}^\dagger + \Omega_c\sigma_{ca}^\dagger + h.c.$$

Equation 40

where

$$H^q_{ex-sp} = \left(\alpha_b\rho_{ba} + \alpha_{bc}\rho_{ca}\right)\sigma_{ba}^\dagger + \left(\alpha_c\rho_{ca} + \alpha_{bc}\rho_{ba}\right)\sigma_{ca}^\dagger + h.c.$$

Equation 41

where $\sigma_{bc}^\dagger$ and $\sigma_{ac}^\dagger$ are called, the exciton raising operators for

transition $|a\rangle \leftrightarrow |b\rangle$ and $|a\rangle \leftrightarrow |c\rangle$, respectively. Other parameters appearing in Eqn. 47

are found as:

$$\Omega_b = \mu_{ab}E_P, \quad \Omega_c = \mu_{ac}E_P,$$

and

$$\Pi_b = \frac{\alpha_{sp}e^{-k_{sp}R}\Omega_{ab}}{4\varepsilon_0\varepsilon_f},$$

and

$$\Pi_c = \frac{\alpha_{sp}e^{-k_{sp}R}\Omega_{ac}}{4\pi\varepsilon_0\varepsilon_f},$$

and

$$\alpha_b = \frac{\left(\mu_{ab}^2 \alpha_{sp} g_l e^{-k_{sp}R}\right)}{4\pi\varepsilon_0\varepsilon_f R^3},$$

and

$$\alpha_c = \frac{\left(\mu_{ac}^2 \alpha_{sp} g_l e^{-k_{sp}R}\right)}{4\pi\varepsilon_0\varepsilon_f R^3},$$

and

$$\alpha_{bc} = \left(\frac{\boldsymbol{\mu}_{ba}\cdot\boldsymbol{\mu}_{cac}}{\mu_{ba}\mu_{ca}}\right)\sqrt{\alpha_b\alpha_c}$$

where Ω_{ba} and Ω_{ca} are Rabi frequencies associated with $|a\rangle \leftrightarrow |b\rangle$ and $|a\rangle \leftrightarrow |c\rangle$ transitions, respectively.

The first term H_{ex-p} in Eqn. 47 is the interaction between the exciton and the external probe field E_p. The second term H_{ex-sp}^p is due to the interaction of the excitons with the SPP electric field induced by the probe field.

Therefore, we refer to this as the direct-dipole-dipole interaction (DDI) term. The last contribution H_{ex-sp}^q is due to the interaction of the excitons with the SPP dipole field that arises when the external field polarizes the QE, which in turn creates the SPP field. In other words, this contribution is the self-interaction of the QE since it depends on the polarization of the QE. For this reason, it is called the self-induced DDI term.

We consider that excitons in the QE decay from excited states $|b\rangle$ and $|c\rangle$ to the ground state and lose energy due to the spontaneous emission. This type of decay rate is called the radiation decay. It is also considered that excitons decay due to the exciton-SPP interaction and lose energy to the metamaterial. This type of decay rate is known as the nonradiative decay. The decay interaction Hamiltonian can be written in the second quantized notation using the rotating wave approximation as:

$$H_{\text{int}} = -\left[\sum_{k} \sum_{n=b,c} g_{na}^{r}(\varepsilon_{k}) a_{k} \sigma_{na}^{\dagger} e^{-i(\varepsilon_{na}-\varepsilon_{k})} + \sum_{\beta} \sum_{n=b,c} g_{na}^{nr}(\varepsilon_{\beta}) a_{\beta} \sigma_{na}^{\dagger} e^{-i(\varepsilon_{na}-\varepsilon_{\beta})} + h.c. \right] \qquad \text{Equation 42}$$

where $g_{na}^{r}(\varepsilon_{k})$ and $g_{na}^{nr}(\varepsilon_{\beta})$ are coupling constants for the radiative and nonradiative interactions, respectively. They are found as:

$$g_{na}^{r} = i \left(\frac{\varepsilon_{k}}{2 \in_{0} \pi V_{q}} \right)^{1/2} (\mathbf{\mu}_{na}.\mathbf{e}_{k}) \qquad \text{Equation 43}$$

where

$$g_{na}^{nr} = i \left(\frac{\varepsilon_{\beta}}{2 \in_{0} \pi V_{q}} \frac{\alpha_{sp} e^{-k_{sp}R}}{4\pi \in_{q}} \right)^{1/2} (\mathbf{\mu}_{na}.\mathbf{e}_{k}) \qquad \text{Equation 44}$$

where $\in_{q}$ is the dielectric constant of the metamaterial at zero frequency, μ_{na} is induced dipole moment due to the transition $|n\rangle \leftrightarrow |a\rangle$, operator a_{k} is the photon annihilation operator for energy ε_{k}, operator a_{β} is the SPP annihilation operator for energy ε_{β} and V_{q} is the volume of the QE.

5.3 Density Matrix Method and Absorption Coefficient

We use the density matrix method to evaluate the absorption coefficient due to exciton transitions $|a\rangle \leftrightarrow |b\rangle$ and $|a\rangle \leftrightarrow |c\rangle$. Using Eqns. 26–35 for the Hamiltonian of the system and the master equation for the density matrix we can obtain the following equations for the motion density matrix elements:

$$\frac{dr_{cc}}{dt} = -g_c r_{cc} - p\left(\sqrt{g_c g_b}/2\right)(r_{cb} + r_{bc}) + i\left(W_c + P_c\right)r_{ac} - i\left(W_c + P_c\right)^* r_{ca} + ib\left(r_{ba}r_{ac} - r_{ab}r_{ca}\right)$$

$$\frac{dr_{bb}}{dt} = -g_b r_{bb} - p\left(\sqrt{g_c g_b}/2\right)(r_{cb} + r_{bc}) + i\left(W_b + P_b\right)r_{ab} - i\left(W_b + P_b\right)^* r_{ba} + ib\left(r_{ab}r_{ca} - r_{ba}r_{ac}\right)$$

$$\frac{dr_{ca}}{dt} = -X_{ca} r_{ca} - p\left[\sqrt{g_c g_b}/2 + i\sqrt{a_b a_c}(r_{cc} - r_{aa})\right]r_{ba} - i\left(W_c + P_c\right)(r_{cc} - r_{aa}) - i(W_b + P_b + a_b r_{ba})r_{cb}$$

$$\frac{dr_{ba}}{dt} = -X_{ba} r_{ba} - p\left[\sqrt{g_c g_b}/2 + i\sqrt{a_b a_c}(r_{bb} - r_{aa})\right]r_{ca} - i\left(W_b + P_b\right)(r_{bb} - r_{aa}) - i(W_c + P_c + a_c r_{ca})r_{bc}$$

$$\frac{dr_{cb}}{dt} = \left(\begin{array}{c} -X_{cb} r_{cb} - p\left(\sqrt{g_c g_b}/2\right)(r_{cc} + r_{bb}) + i\left(W_c + P_c\right)r_{ab} - i(W_b + P_b)^* r_{ca} + i(a_c - a_b)r_{ca}r_{ab} \\ +ip\sqrt{a_b a_c}\left(|r_{ba}|^2 - |r_{ca}|^2\right) \end{array} \right)$$

Equation 45

where $p = \left(\mathbf{\mu}_{ba} \cdot \mathbf{\mu}_{ca} / \mu_{ba}\mu_{ca}\right)$ is called the interference parameter and it is responsible for the quantum interference in the system. Other parameters appearing in Eqn. 36 are found as:

$$\Xi_{ca} = \frac{\gamma_c}{2} + i\delta_c + i\alpha_c(\rho_{cc} - \rho_{aa}) + i\alpha_{bc}\rho_{cb}$$ **Equation 46**

$$\Xi_{ba} = \frac{\gamma_b}{2} + i\delta_b + i\alpha_b(\rho_{bb} - \rho_{aa}) + i\alpha_{bc}\rho_{bc}$$

$$\Xi_{cb} = \frac{\gamma_b + \gamma_c}{2} + i\left(\delta_c - \delta_b\right)$$

Here $\delta_b = \omega_{ab} - \omega$ and $\delta_c = \omega_{ac} - \omega$ are called the probe field detunings. Physical

quantities γ_b and γ_c are the decay rates of the levels $|b\rangle$ and $|c\rangle$, respectively and

are found as:

$$\gamma_b = \gamma_b^r + \gamma_b^{nr}, \quad \gamma_c = \gamma_c^r + \gamma_c^{nr} \qquad \text{Equation 47}$$

where

$$\gamma_{bc} = p\sqrt{\left(\gamma_b^r + \gamma_b^{nr}\right)\left(\gamma_c^r + \gamma_c^{nr}\right)} \qquad \text{Equation 48}$$

and

$$\gamma_b^r = \frac{\mu_{ba}^2 \varepsilon_{ba}^3}{3\pi \in_0 \hbar^4 c^3}, \gamma_c^r = \frac{\mu_{ca}^2 \varepsilon_{ca}^3}{3\pi \in_0 \hbar^4 c^3} \qquad \text{Equation 49}$$

where

$$\gamma_b^{nr} = \gamma_b^r \left(\frac{\alpha_{sp} e^{-k_{sp}R}}{4\pi \in_q}\right), \gamma_c^{nr} = \gamma_c^r \left(\frac{\alpha_{sp} e^{-k_{sp}R}}{4\pi \in_q}\right) \qquad \text{Equation 50}$$

where γ_c^r and γ_c^{nr} are radiative and nonradiative decay rates, respectively. Note that

the radiative decay rate depends on the SPP frequency and distance of the QE from

the interface. The absorption coefficient due to the transitions $|a\rangle \leftrightarrow |b\rangle$ and $|a\rangle \leftrightarrow |c\rangle$

is calculated in the literature [52], [65] and it is written as:

$$\alpha_{abs} = \alpha_0 \, \text{Im}\left(\frac{\rho_{ab} + \rho_{ac}}{\Omega}\right) \qquad \text{Equation 51}$$

where

$$\alpha_0 = \frac{\mu_{ab}^2 \omega_p}{\hbar c}$$

Equation 52

where $\mu_{ab} = \mu_{ac}$ is considered. Matrix elements ρ_{ab} and ρ_{ac} appearing in Eqn. 58 will be evaluated numerically.

An analytical expression for the absorption coefficient can be obtained if we consider that $\rho_{aa} > \rho_{bb}$ and $\rho_{aa} > \rho_{cc}$. In this approximation, we get $\rho_{aa} \approx 1$ since $\rho_{aa} + \rho_{bb} + \rho_{cc} = 1$.

Now Eqn. 51 can be rewritten as:

$$\frac{d\rho_{ca}}{dt} = -\Xi_{ca}\rho_{ca} - \Phi\rho_{ba} + i(\Omega_c + \Pi_c)$$

$$\frac{d\rho_{ba}}{dt} = -\Xi_{ba}\rho_{ba} - \Phi\rho_{ca} + i(\Omega_b + \Pi_b)$$

$$\frac{d\rho_{cb}}{dt} = -\Xi_{cb}\rho_{cb} + i(\Omega_c + \Pi_c)\rho_{ab}$$

Equation 59

Here $\Phi = p(\sqrt{\gamma_c \gamma_b}/2 - i\sqrt{\alpha_b \alpha_c})$. In the steady state the above two equations are solved for ρ_{ba}, ρ_{cb} and ρ_{ca} and their expressions are found as:

$$\rho_{ba} = \frac{i(\Phi(\Omega_c + \Pi_c) - \Xi_{ca}(\Omega_b + \Pi_b))}{(\Phi^2 - \Xi_{ba}\Xi_{ca})}$$

Equation 53

and

$$\rho_{ca} = \frac{i(\Phi(\Omega_b + \Pi_b) - \Xi_{ba}(\Omega_c + \Pi_c))}{(\Phi^2 - \Xi_{ba}\Xi_{ca})}$$

Equation 54

and

$$\rho_{cb} = \frac{i\left(\left(\Omega_b + \Pi_b\right)\rho_{ab} - \left(\Omega_c + \Pi_c\right)\rho_{ca}\right)}{\Xi_{cb}}$$

where

$$\Xi_{ca} = \frac{\gamma_c}{2} + i\delta_c - i\alpha_c + i\alpha_{bc}\rho_{cb}$$

$$\Xi_{ba} = \frac{\gamma_b}{2} + i\delta_b - i\alpha_b + i\alpha_{bc}\rho_{bc}$$

Putting the expressions of ρ_{ba} and ρ_{ca} from Eqn. 41 into Eqn. 57 we get:

$$\alpha = \alpha_0 \text{ Im}\left(\frac{i\left(\Phi - \Xi_{ca}\right)\left(1 + \Pi_b / \Omega\right) + \left(i\Phi - \Xi_{ba}\right)\left(1 + \Pi_c / \Omega\right)}{\left(\Phi^2 - \Xi_{ba}\Xi_{ca}\right)}\right)$$

This expression will be used to calculate the absorption of light in the next section.

5.4   Results and Discussions

In this section, we considered the metamaterial to be fabricated from gold with SPP

energy $\varepsilon_{sp} = \hbar\omega_{sp} = 2.2eV$. We considered the radiation decay rates (energies) and Rabi

frequencies for both excitons to be the same i.e. $\gamma_b^r = \gamma_c^r = \gamma$ and $\Omega_b = \Omega_c = \Omega$. All

energies in the simulations were measured with respect to the radiation decay energy γ .

Parameters used in the calculations are shown in the captions to the figures.
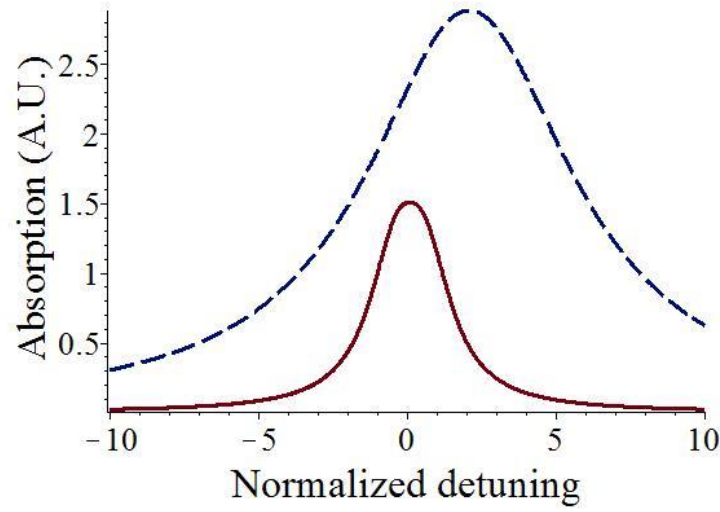
Figure 17 — The absorption of light in arbitrary units (A.U.) plotted against the normalized probe detuning in the absence of interference (p=0). The solid and dotted lines correspond to the absence and presence of the exciton-SPP interaction, respectively. All energies were measured with respect to the radiative decay energy γ^r. Values of the physical parameters used were $e_f = 1.0$, $e_d = 1.5$, $\hbar\omega_p = 5eV$, $W = 1.0$, $P = 5.0$, $a = 2$, $R = 20nm$, $k_{sp} = 0.5/R$, and $\hbar\omega_{ba} = 0.5$.

Let us calculate the absorption of light in the absence of quantum coherence (i.e. p=0). The normalized absorption spectrum is plotted in Fig. 17 with respect to the normalized probe detuning parameter $\delta = (\delta_b + \delta_c)/2$. We considered that the energy difference between excitons was smaller than that of the radiation decay energy i.e. $\omega_{cb} < \gamma$.

Solid and dotted curves were plotted in the absence and presence of the exciton-SPP interaction, respectively. Note that there was enhancement of absorption light in the presence of exciton-SPP interaction. This was due to the presence of the SPP field, which fell on the QE, and there was energy transfer from the metamaterial to the QE. The main term, which was responsible for this process, is H^p_{ex-sp} appearing in Eqn. 47.

It is also noted from Fig. 17 that the peak of the absorption spectrum in the presence of the exciton-SPP interaction is broader and also shifted to the right. This shift was due to the self-induced DDI interaction term between the QE and the metamaterial. The broadening was due to the nonradiative decay rate. The enhancement of the light was partially depressed due to loss of energy due to the nonradiative decay from the QE to the metamaterial. The shift and broadening of the absorption peak can be explained clearly by Eqn. 63 by putting p=0. This equation reduces to:

$$\alpha_{abs} = \alpha_0 \, \text{Im}\left(\frac{2(1+\Pi/\Omega)\left[(\delta_k - \alpha) - i(\gamma^r + \gamma^{nr})\right]}{\left[(\delta_k - \alpha) - i(\gamma^r + \gamma^{nr})\right]^2 - \omega_{32}^2} \right)$$

Equation 58

Here $a_b = a_c = a$. Note that the denominator in the above expression contains term α s, which is responsible for the shift. These terms were due to the dipole-dipole interaction. On the other hand, the broadening was due to the γ^{nr} term, which was responsible for the nonradiative decay process.
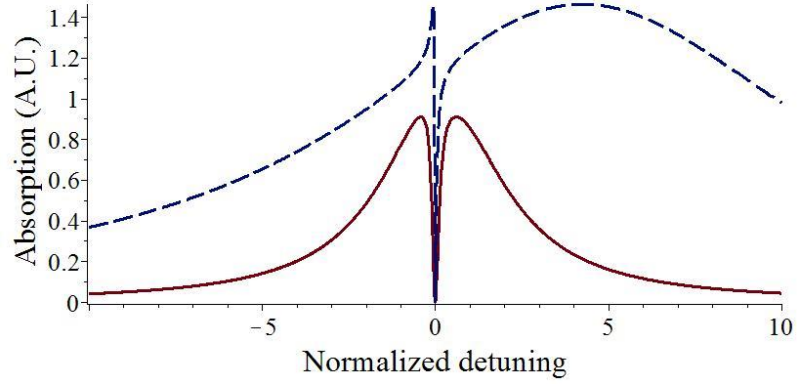
Figure 18 — The absorption of light in arbitrary units (A.U.) plotted against the normalized probe detuning in the absence of the interference (p=1). The solid and dotted lines correspond to the absence and presence of the exciton-SPP interaction, respectively. All energies were measured with respect to the radiative decay energy γ^r. Values of the physical parameters were $e_f = 1.0$, $e_d = 1.5$, $\hbar\omega_p = 5eV$, $W = 1.0$, $P = 5.0$, $a = 2$, $R = 20nm$, $k_{sp} = 0.5 / R$, $g^{nr} = 3$, and $\hbar\omega_{ba} = 0.5$.
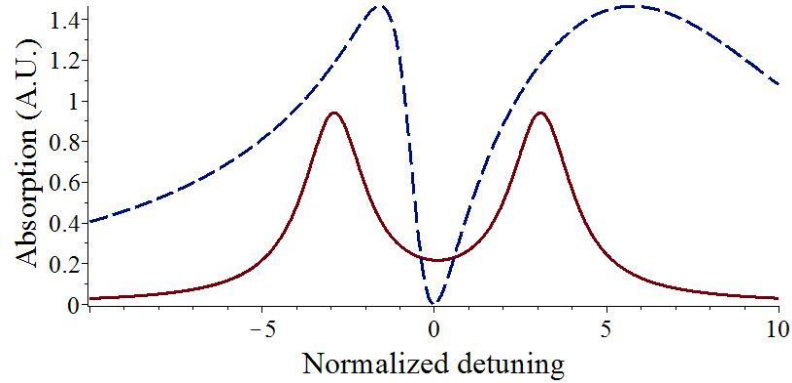
Figure 19 — The absorption of light in arbitrary units (A.U.) plotted against the normalized probe detuning in the absence of the interference (*p*=0). The solid and dotted lines correspond to the absence and presence of the exciton-SPP interaction, respectively. All energies were measured with respect to the radiative decay energy γ^r.

Values of the physical parameters were $e_f = 1.0$, $e_d = 1.5$, $\hbar\omega_p = 5eV$, $W = 1.0$, $P = 5.0$, $a = 2$, $R = 20nm$,

$k_{sp} = 0.5/R$, $g^{nr} = 3$, and $\hbar\omega_{ba} = 3$.
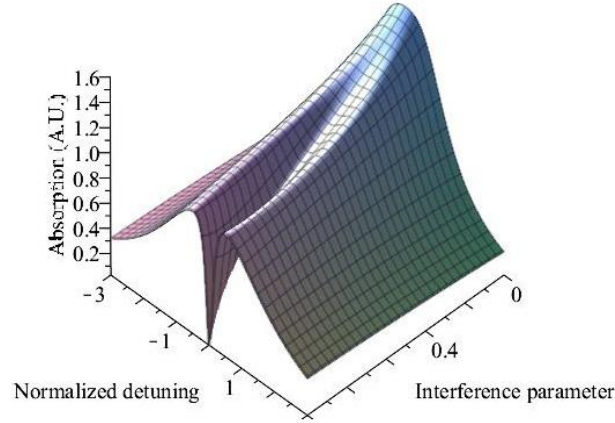
Figure 20 — The absorption of light in arbitrary units (A.U.) plotted against the normalized probe detuning and interference parameter in the absence (5a) and presence (5b) of the exciton-SPP interaction. All energies were measured with respect to the radiative decay energy γ^r. Values of the physical parameters were $e_f = 1.0$, $e_d = 1.5$, $\hbar\omega_p = 5eV$, $W = 1.0$, $P = 0.0$, $a = 0$, $R = 20nm$, $k_{sp} = 0.5/R$, $g^{nr} = 0$, and $\hbar\omega_{ba} = 0.5$.
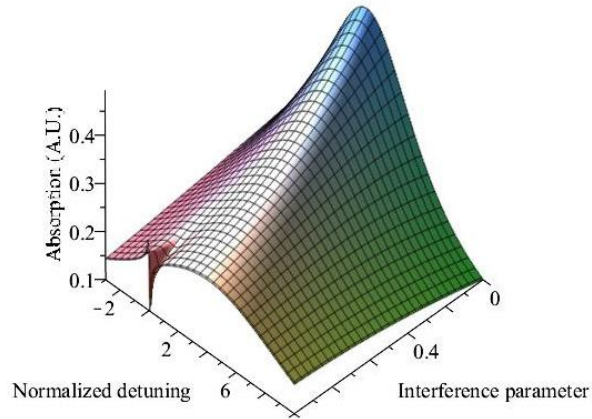
Figure 21 — The absorption of light in arbitrary units (A.U.) plotted against the normalized probe detuning and interference parameter in the presence of the exciton-SPP interaction. All energies were measured with respect to the radiative decay energy γ^r. Values of the physical parameters were $e_f = 1.0$, $e_d = 1.5$, $\hbar\omega_p = 5eV$, $W = 1.0$, $P = 5.0$, $a = 2$, $R = 20nm$, $k_{sp} = 0.5/R$, $g^{nr} = 3$, and $\hbar\omega_{ba} = 0.5$.

Now we include the effect of the quantum interference term in the absorption of light. The results are plotted in Fig. 18. Solid and dotted curves are plotted in the absence and presence of the exciton-SPP interaction, respectively. Note that at zero normalized detuning the absorption of light disappeared and the spectrum had two peaks. The disappearance of the absorption was due to the quantum interference.

In the absence of the exciton-SPP interaction the spectrum had symmetric structure with respect to zero detuning. In other words, peaks were located at equal distances with respect to zero detuning and also the height and the width of both peaks were the same.

On the other hand, in the presence of the exciton-SPP interaction the absorption spectrum had asymmetric structure. In other words, peaks were located at different places with respect to zero detuning, and the height and width of both peaks were also different.

Now we present calculation for the absorption when the energy difference between excitons was smaller than that of the radiation decay energy i.e. $\omega_{cb} > \gamma$. The results are present in Fig. 19. Solid and dotted curves were plotted in the absence (p=0) and presence (p=1) of the quantum interference term, respectively.

Note that in the absence of the quantum interference in Fig. 17 has one peak and on the other hand in Fig. 19 the spectrum has two peaks. In Fig. 17, the two peaks merge into one peak due to the broadening of two peaks since $\omega_{cb} < \gamma$. In this case the single peak split into two peaks due to the $\omega_{cb} > \gamma$ condition.

We have plotted the effect of the quantum coherence in Figs. 20 and 21 in the absence and the presence of the exciton-SPP interaction, respectively. The absorption spectrum split from one peak to two peaks as the interference parameter increased to a maximum value of p = 1. Note that in Fig. 20 the spectrum is symmetric whereas in Fig. 21 the spectrum is asymmetric due to the exciton-SPP interaction. One can also see the quantum interference effect was reduced due to exciton-SPP interaction.

We would like to make comments on our theory. This theory was developed for SPPs located at the interface between a dielectric slab and a metamaterial slab. In other words, we have calculated SPPs for 2-dimensional hybrid systems. This theory cannot be applied to 3-dimensional hybrid systems fabricated from depositing spherical dielectric material on the top of the spherical metamaterial. In this case, SPPs are localized in all three directions.

Recently Feng et al. [14] have proposed a broadband infrared absorber by engineering the frequency dispersion of the metamaterial surface. They have demonstrated that the absorption bandwidth in metamaterials can be dramatically enhanced through utilizing the metamaterial surface to mimic the dispersion of an ideal absorbing sheet. Pu et al. [66] have also studied the transmission of light in planar metamaterials with perturbed periodicity and found an enhancement in Fano resonances in the transmission coefficient.

In these two papers, authors have studied absorption and emission in metamaterials. Whereas in the present paper we have studied the effect of metamaterials on the absorption in the quantum emitters. The absorption bandwidth in quantum emitters can be increased by dispersion engineering and multiple Fano resonances in metamaterials as discussed in the above papers.

Chapter 6

6   **Conclusion**

After having simulated thousands of NHAs with varying periodicities and hole sizes, it was found that for specific applications, a NHA can be tuned to provide the desired intensity, bandwidth, and resonance peak location. This saved time and cost from having to physically fabricate numerous NHAs in search of the same transmission spectrum for the desired application. The simulation results agreed with the experimental and fabricated results. This meant that, depending on the application, an optimal NHA could be found via simulations compared to the previous methods of having to fabricate these multiple times.

For the first time, 3D NHAs with cavity-based plasmonic nanosensors were used for SERS-based molecular sensing. Compared to 2D NHAs, 3D NHAs provided an extra factor used toward the enhancement of the Raman signal due to the strong SPP and LSPR coupling which the 2D NHAs lack. Both simulated and experimental results showed the transmission spectra. It was found that the cavity of the 3D NHA provided an optical trapping effect when sensing a small number of molecules. This strong SPP and LSPR coupling and optical trapping effect resulted in an EF of 10^7 which was used to sense the Raman signal for a single molecule. 3D NHAs can therefore be used for the detection of different molecules since the resonance peaks can be tuned to different positions by changing the periodicity and hole size of the NHA.

Furthermore, we have investigated the absorption coefficient experimentally and theoretically in metallic metamaterials made from an array of split ring resonators. SPPs were found at the interface between the split ring resonators and the substrate. The absorption coefficient spectrum was measured for one sample having a unique split ring resonator radius and periodicity. Each measured spectrum had several resonance peaks due to SPPs. The transmission line theory of metamaterials and Bloch's theorem was used to calculate SPP energies. The transmission and absorption coefficients were calculated using the transfer matrix method. Due to the transmission and absorption coefficients having a similar derivation to that of the NHAs, we compared the theoretical results with the experimental results of a NHA. The experimental and theoretical results agreed well, implying that the theoretical results of the SRRs are correct. This showed that the locations of spectral peaks were dependent on the NHAs' periodicity and hole size.

The interaction of light between QEs and SPPs was found at the interface between the dielectric material and the metal. Excitons also decayed from excited state to the ground state due to the radiative and nonradiative processes. The quantum interference phenomenon occurred between excitons decay rates. It was found that there was a decrease in the absorption of light due to quantum interference. There was also an enhancement in the absorption of light due to the exciton-SPP interaction. This was caused when the light coupled instead of interfered. Absorption peaks were shifted and broadened due to the SPP coupling. Furthermore, due to the exciton-SPP interaction, there was an area with zero transmission which was a result of deconstructive interference. Therefore, since the metamaterial can be fabricated with different periodicities and radii resulting in the shifting in the absorption peak and changes in

the bandwidth of each peak, it can be beneficial in filtering or sensing for medical applications. Additionally, due to the constructive and destructive interference which was observed when probing the QEs, these metamaterials could be used as optical switches for photonic applications.

6.1 Future Recommendations

Future experiments regarding the fabrication of NHAs or other metamaterial structures could benefit by first simulating NHAs with varying periodicities and hole sizes to study how these affect the transmission spectra of the NHAs. Using the code provided in this thesis, numerous simulations could be performed and compared to each other in order to provide a NHA with the most optimal transmission spectrum for a desired application. This would prevent unnecessary fabrications, saving time and money.

Secondly, when measuring the transmission of a metamaterial, FDTD solutions software (Lumerical Inc.) is recommended as it allows for a full frequency sweep. This particular software allows the user to simulate any metamaterial and to use a wide range of frequencies for the incident light to measure the transmission of the metamaterial – as opposed to other leading software that do not allow for frequency sweeps. FDTD solutions also has a user-friendly interface and uses a generic scripting language that is easy to learn.

Appendices

Appendix A – FDTD Solutions Script

```
#############################################################################
# Scriptfile: TestGUI.lsf
#
# Description: Creates a gui that allows the user to create a metamaterial.
#############################################################################

#open the new wizard
newwizard(200,200,"NHA");
wizardoption("fontsize",12);
wizardoption("fieldwidth",200);
wizardoption("fieldheight",20);
newwizardpage("Go");
wizardwidget("label",endl+"Choose the dimensions in for the Power Box"+endl);
wizardoption("margin",50);
wizardwidget("menu","Run from:","Simulation|Saved File");
wizardwidget("menu","Material:","Gold|Silver|Aluminium");
wizardwidget("menu","Lattice Arrangement :","Square|Hexagonal|Rectangular");
wizardwidget("menu","Angles :","[0]|[0,5,12]|[0,1,3,5,7,9]");
wizardwidget("label",endl);
wizardwidget("number","Min-Hole Size (nm):",180);
wizardwidget("number","Max-Hole Size (nm):",180);
wizardwidget("number","Step-Hole Size (nm):",10);
wizardwidget("label",endl);
wizardwidget("number","Min-Periodicity (nm):",340);
wizardwidget("number","Max-Periodicity (nm):",340);
wizardwidget("number","Step-Periodicity (nm):",10);
wizardwidget("label",endl);
wizardwidget("number","Thickness (nm):",155);
wizardwidget("number","Index :",1);
wizardwidget("number","Number of Holes :",1);
wizardwidget("label",endl);
wizardwidget("checkbox","Bandwidth Test",0);
wizardwidget("checkbox","Save Max Peaks",1);
wizardwidget("checkbox","Visualize",1);
wizardwidget("checkbox","Wavelength",0);
wizardwidget("label",endl);
wizardwidget("menu","If Rectangular :","PML on top|Periodic");
wizardwidget("number","Length of Wire (nm):",15000);
wizardwidget("label",endl);
```

```
wizardwidget("checkbox","SiO Layer",1);
wizardwidget("number","SiO Thickness (nm):",200);

#get the user set dimensions
out = runwizard;

Runfrom=wizardgetdata(1);
Material=wizardgetdata(2);
Shape=wizardgetdata(3);
Angles=wizardgetdata(4);
min_holesize=wizardgetdata(5)*1e-9;
max_holesize=wizardgetdata(6)*1e-9;
step_holesize=wizardgetdata(7)*1e-9;
min_periodicity=wizardgetdata(8)*1e-9;
max_periodicity=wizardgetdata(9)*1e-9;
step_periodicity=wizardgetdata(10)*1e-9;
rect_zspan=wizardgetdata(11)*1e-9;
nindex=wizardgetdata(12);
periodicity=wizardgetdata(18);

numberofholes=wizardgetdata(13);
bandwidthtest=wizardgetdata(14);
savemaxpeaks=wizardgetdata(15);
visualizetest=wizardgetdata(16);
getwavelength=wizardgetdata(17);
wirelength=wizardgetdata(19)*1e-9;

SiOcheck=wizardgetdata(20);
SiOthickness=wizardgetdata(21)*1e-9;

killwizard;
#break if the user cancelled
if(out==0) {
   ?"User cancelled";
   break;
}
#if the user pressed "Go", add the monitor box
if(Material==1){
   material=1;
}
if(Material==2){
   material=3;
}
if(Material==3){
   material=2;
}
```

```
if(Runfrom==1){
   simulationtest=1;
}
if(Runfrom==2){
   simulationtest=0;
}

if(Shape==1){
   shape=0;
}
if(Shape==2){
   shape=1;
}
if(Shape==3){
   shape=2;
}
if(Angles==1){
   testangles=0;
}
if(Angles==2){
   testangles=1;
   anglelist = [0,5,12];
}
if(Angles==3){
   testangles=1;
   anglelist = [0,1,3,5,7,9];
}
if(periodicity=1){
   per=0;
}
if(periodicity=2){
   per=1;
}
Run_Hole_Periodicity;
#if the user pressed "Go", add the monitor box
```

```
################################################################################
# Scriptfile: create_nanohole.lsf
#
# Description: Creates a nanohole with variable hole size and periodicity.
################################################################################

newproject;
clearjobs;

if(material==1){
    if(testangles==1){
        cd("/Users/kiefferdavieau/desktop/Research/Gold/Angles"); # Data for index (1.45)
matched, Data2 for water (1.33)
    }
    if(shape==0){
        cd("/Users/kiefferdavieau/desktop/Research/Gold/Square"); # Data for index (1.45)
matched, Data2 for water (1.33)
    }
    if(shape==1){
        cd("/Users/kiefferdavieau/desktop/Research/Gold/Hex"); # Data for index (1.45)
matched, Data2 for water (1.33)
    }
    if(shape==2){
        cd("/Users/kiefferdavieau/desktop/Research/Gold/Rectangular"); # Data for index
(1.45) matched, Data2 for water (1.33)
    }
}
if(material==2){
    if(testangles==1){
        cd("/Volumes/CLOUD3/First
Paper/Simulations/NewSimulations/Aluminium/Angles"); # Data for index (1.45)
matched, Data2 for water (1.33)
    }
    if(shape==0){
        cd("/Volumes/CLOUD3/First
Paper/Simulations/NewSimulations/Aluminium/Square"); # Data for index (1.45)
matched, Data2 for water (1.33)
    }
    if(shape==1){
        cd("/Volumes/CLOUD3/First
Paper/Simulations/NewSimulations/Aluminium/Hex155-200"); # Data for index (1.45)
matched, Data2 for water (1.33)
    }
    if(shape==2){
        cd("/Volumes/CLOUD3/First
Paper/Simulations/NewSimulations/Aluminium/Rectangular"); # Data for index (1.45)
```

```
matched, Data2 for water (1.33)
    }
}
if(material==3){
    if(testangles==1){
        cd("/Users/kiefferdavieau/desktop/Research/Silver/Angles"); # Data for index (1.45)
matched, Data2 for water (1.33)
    }
    if(shape==0){
        cd("/Users/kiefferdavieau/desktop/Research/Silver/Square"); # Data for index (1.45)
matched, Data2 for water (1.33)
    }
    if(shape==1){
        cd("/Users/kiefferdavieau/desktop/Research/Silver/Hex"); # Data for index (1.45)
matched, Data2 for water (1.33)
    }
    if(shape==2){
        cd("/Users/kiefferdavieau/desktop/Research/Silver/Rectangular"); # Data for index
(1.45) matched, Data2 for water (1.33)
    }
}


################################################################################
#material = 1; #1=GOLD, 2=ALUMINIUM, 3=SILVER
#Loop through multiple variations of hole sizes and periodicities
#simulationtest = 1; #0 for no simulations, 1 for running simulations
#openwithoutsimulations = 0; #0 if running simulations, 1 if not running simulations
#bandwidthtest = 0; #0 for no test, 1 for test of bandwidh of max peak
#savemaxpeaks = 1; #0 to not save, 1 to save
#visualizetest = 1; #0 to not visualize/plot, 1 to plot the graphs

nanoholearray = 0; #0 for single nanohole, 1 for nanohole array
#numberofholes = 1; #Number of holes in NHA
#shape = 0; #0 for square, 1 for hexagonal lattice arrangement

#testangles = 0;
#anglelist = [0,5,12];
################################################################################
#min_holesize = 1.5e-007; # Variables to change
#max_holesize = 2.5e-007; # Variables to change
#step_holesize = 0.10e-007; # Variables to change - Intervals at which the hole increases
by

#min_periodicity = 4.0e-007; # Variables to change
#max_periodicity = 4.0e-007; # Variables to change
```

```
#step_periodicity = 0.10e-007; # Variables to change - Intervals at which the periodicity
increases by

#Gold Rectangle - Thickness
#rect_zspan = 1.0e-007;

min_hperiodicity = min_periodicity;
max_hperiodicity = max_periodicity;

#nindex = 1.0; # Variables to change - Index of fdtd (air = 1.00, water = 1.33, pyrex =
1.45)
############################################################################
if (testangles==0){
    anglelist=[0];
    ang = 0;
}

?nPtshole = round(((((max_holesize - min_holesize)/step_holesize)+1));
?nPtsper = round(((((max_periodicity - min_periodicity)/step_periodicity)+1));

#holesizenPts = (max_holesize - min_holesize)/step_holesize;
#periodicitynPts = (max_periodicity - min_periodicity)/step_periodicity;


nPts = nPtshole*nPtsper*length(anglelist);
nPts = round(nPts);
?sqrt(nPts);
array_T_fields = cell(nPts);
array_filenames = cell(nPts);
counter_filenames = 1;
counter_index = 1;
############################################################################
rect_span = 10.0e-007; #w/l of gold and w/l/h of pyrex

mesh_span = min_periodicity; #Size of mesh refinement located on nano-hole

#Pyrex Rectangle
recti_index = 1.4585; # Variables to change - index for Pyrex
recti_zspan = 10.0e-007;
recti_z = -5.0e-007; #location on z axis

#Plane Wave Source
plane_z = -4.8e-007; #location on z axis


#Monitor
```

```
monitor_z = 5.0e-007; #location on z axis
monitor_frequencypoints = 1200;
###############################################################################
nPtsflaghole = 1;
nPtsflagper = 1;
if(max_holesize==min_holesize){
   nPtsflaghole = 0;
}
if(max_periodicity==min_periodicity){
   nPtsflagper = 0;
}

if(material == 1){
   materialname="Gold";
   materialtype=copymaterial("Au (Gold) - Palik");
   setmaterial("Au (Gold) - Palik Copy 1","max coefficients", 10);
   plane_wlstart = 3.0e-007; #wavelength start
   plane_wlstop = 10.0e-007; #wavelength stop
}
if(material == 2){
   materialname="Aluminium";
   materialtype=copymaterial("Al (Aluminium) - Palik");
   plane_wlstart = 4.0e-007; #wavelength start
   plane_wlstop = 10.0e-007; #wavelength stop
}
if(material == 3){
   materialname="Silver";
   #materialtype=copymaterial("Ag (Silver) - CRC");
   materialtype=copymaterial("Ag (Silver) - Palik (0-2um)");
   #setmaterial("Ag (Silver) - CRC Copy 1","max coefficients", 8);
   plane_wlstart = 3.0e-007; #wavelength start
   plane_wlstop = 10.0e-007; #wavelength stop
}
###############################################################################
if(simulationtest==1) { # if 0, skip these lines. if 1, run these lines
###############################################################################
   for(j=1:nPtshole) { # loops through min_holesize to max_holesize with steps of
step_holesize
      #Etch Circle
      hole_size = min_holesize; #HOLE SIZE
      circ_r = hole_size/2;
      circ_zspan = rect_zspan;
      circ_z = rect_zspan/2; #location on z axis


###############################################################################
```

```
    min_periodicity = min_hperiodicity; # reset the min_periodicity which is a variable
in the next for loop
################################################################################
    for(k=1:nPtsper) { # loops through min_periodicity to max_periodicity with steps of
step_periodicity
        k;
        newproject(2); # creates a new project

        #Refined Mesh
        #mesh_xspan = min_periodicity;
        #mesh_yspan = min_periodicity;
        #mesh_zspan = 2.0e-007;
        #mesh_z = 0.3e-007; #location on z axis
        #mesh_derivative = 0.10e-007; #indicates the mesh overide accuracy


################################################################################

        #Variables

        #FDTD Solution Mesh
        fdtd_xspan = min_periodicity; #PERIODICITY
        fdtd_yspan = min_periodicity;
        if(shape == 2){
            fdtd_yspan = wirelength + min_periodicity;
        }
        fdtd_zspan =12e-007;
        fdtd_index = nindex; #index for exterior of gold (not Pyrex index)
        fdtd_meshacc = 5; #indicates the accuracy for the mesh (1 min - 8 max)

################################################################################
        if(testangles==1) { # if 0, skip these lines. if 1, run these lines
################################################################################
            length(anglelist);
            for(m=1:length(anglelist)){
                newproject(2); # creates a new project

                #Create Nano-hole
                ang = anglelist(m);
                if (nanoholearray==0) { # if 0, skip these lines. if 1, run these lines
################################################################################
                    create_nanohole;
                }else{ # if 0, skip these lines. if 1, run these lines
################################################################################
                    create_nanohole_array;
                }
```

```
                #Save File
                hole_sizetxt = num2str(min_holesize * 1e009);
                fdtd_xspantxt = num2str(min_periodicity * 1e009);
                angletxt = num2str(anglelist(m));
                file_name = "D" + hole_sizetxt + "_P" + fdtd_xspantxt + "_Theta-" +
angletxt;
                save(file_name);

                addjob(file_name);

                array_filenames{counter_filenames} = file_name;
                counter_filenames = counter_filenames + 1;
                }
            }else{

                #Create Nano-hole
                if(nanoholearray==0) { # if 0, skip these lines. if 1, run these lines
###############################################################################
                    create_nanohole;
                }else{ # if 0, skip these lines. if 1, run these lines
###############################################################################
                    create_nanohole_array;
                }

            #Save File
            hole_sizetxt = num2str(min_holesize * 1e009);
            fdtd_xspantxt = num2str(min_periodicity * 1e009);
            file_name = "D" + hole_sizetxt + "_P" + fdtd_xspantxt;
            save(file_name);
            addjob(file_name);
            array_filenames{counter_filenames} = file_name;
            counter_filenames = counter_filenames + 1;
        }
        min_periodicity = min_periodicity + step_periodicity;
    }
    min_holesize = min_holesize + step_holesize;
  }
  runjobs; # run all the jobs in order
}


###############################################################################
# This section is to manipulate the files (with out having to run the simulations)
counter_filenames = 1;
if(simulationtest==0) { # if 0, skip these lines. if 1, run these lines
###############################################################################
  for(j=1:nPtshole) { # loops through min_holesize to max_holesize with steps of
```

```
step_holesize
    min_holesize;
    min_periodicity = min_hperiodicity;
    for(k=1:nPtsper) { # loops through min_periodicity to max_periodicity with steps of
step_periodicity
        if(testangles==1) {
            for(m=1:length(anglelist)){
                ang = anglelist(m);
                #Save File
                hole_sizetxt = num2str(min_holesize * 1e009);
                fdtd_xspantxt = num2str(min_periodicity * 1e009);
                angletxt = num2str(anglelist(m));
                ?file_name = "D" + hole_sizetxt + "_P" + fdtd_xspantxt + "_Theta-" +
angletxt;
                array_filenames{counter_filenames} = file_name;

                counter_filenames = counter_filenames + 1;
            }
        }else{
            hole_sizetxt = num2str(min_holesize * 1e009);
            fdtd_xspantxt = num2str(min_periodicity * 1e009);
            file_name = "D" + hole_sizetxt + "_P" + fdtd_xspantxt;
            array_filenames{counter_filenames} = file_name;
            counter_filenames = counter_filenames + 1;
        }
        min_periodicity = min_periodicity + step_periodicity;
    }
    min_holesize = min_holesize + step_holesize; # Increment the first for loop
  }
}
for(i=1:nPts) {
  if(fileexists(array_filenames{i}+".fsp")) {
    ?array_filenames{i};
     load(array_filenames{i}+".fsp");
    #Store T visualizer in array
    T_field = getresult("monitor","T");
############################################################################
    # Testing for bandwidth
    if(bandwidthtest==1) { # if 0, skip these lines. if 1, run these lines
############################################################################
        maxT = max(T_field.T); # Maximum intensity
        ind = find(T_field.T,maxT); # Index for max intensity
        indl = length(T_field.T);
        midwavelength = T_field.lambda(ind); # Wavelength of max intensity
        halfmaxT = maxT / 2; # Half max intensity
        testind = ind;
```

```
flag = 0;
bandwidthl = 0;
bandwidthr = 0;
if(maxT <= 0.9) {
    if(maxT > 0) {
        for(0;flag<1;0) { # similar to a while loop
            if(testind < length(T_field.T)){
                if((T_field.T(testind+1)/halfmaxT)<=1.1) {
                    flag = 1;
                    wavelength = T_field.lambda(testind);
                    bandwidthr = abs((wavelength - midwavelength));
                }
                testind = testind + 1;
            }
            if( testind >= length(T_field.T)) {
                flag = 1;
            }
        }
        testfind = ind;
        for(0;flag<1;0) { # similar to a while loop
            if(testind > 0){
                if((T_field.T(testind-1)/halfmaxT)<=1.1) {
                    flag = 1;
                    wavelength = T_field.lambda(testind);
                    bandwidthl = abs((wavelength - midwavelength));
                }
                testind = testind - 1;
            }
        }
    }
}
bandwidth = bandwidthl + bandwidthr;
}
##############################################################################
if(savemaxpeaks==1) { # if 0, skip these lines. if 1, run these lines
##############################################################################
maxT = max(T_field.T);
ptext = replace(array_filenames{i},1,1,"");
ptext = replace(ptext,4,1,", ");
dtext = replace(ptext,6,1,"");
filename = array_filenames{i}+".txt";
for(l=1:length(T_field.T)) {
    write(filename,num2str(T_field.T(l)));
    #write("Lambda.txt",num2str(T_field.lambda(l) * 1e009));
}
#write("PeaksP600nm.txt",dtext+", "+num2str(maxT)+",
```

```
"+num2str(bandwidth)+", "+num2str(midwavelength));
      }
      array_T_fields{counter_index} = T_field;
      counter_index = counter_index + 1;
   }
}
if(getwavelength==1) {
   load(array_filenames{1}+".fsp");
   T_field = getresult("monitor","T");
   ?x=length(T_field.T);
   for(l=1:length(T_field.T)) {
      write("Lambda.txt",num2str(T_field.lambda(l) * 1e009));
   }
}


##############################################################################
# This section is to plot all the simulations, unfortunately there is no loop that can do
this.........

if(visualizetest==1) { # if 0, skip these lines. if 1, run these lines
##############################################################################
   if(nPts<=60){
      if(nPts<=30){
         if(nPts<=15){
            if(nPts==1){
               visualize(array_T_fields{1});
            }
            if(nPts==2){
               visualize(array_T_fields{1},array_T_fields{2});
            }
            if(nPts==3){
               visualize(array_T_fields{1},array_T_fields{2},array_T_fields{3});
            }
            if(nPts==4){

visualize(array_T_fields{1},array_T_fields{2},array_T_fields{3},array_T_fields{4});
            }
            if(nPts==5){

visualize(array_T_fields{1},array_T_fields{2},array_T_fields{3},array_T_fields{4},arra
y_T_fields{5});
            }
            if(nPts==6){
visualize(array_T_fields{1},array_T_fields{2},array_T_fields{3},array_T_fields{4},arra
y_T_fields{5},array_T_fields{6});
            }
```

```
        if(nPts==7){
visualize(array_T_fields{1},array_T_fields{2},array_T_fields{3},array_T_fields{4},arra
y_T_fields{5},array_T_fields{6},array_T_fields{7});
        }
        if(nPts==8){
visualize(array_T_fields{1},array_T_fields{2},array_T_fields{3},array_T_fields{4},arra
y_T_fields{5},array_T_fields{6},array_T_fields{7},array_T_fields{8});
        }
        if(nPts==9){
visualize(array_T_fields{1},array_T_fields{2},array_T_fields{3},array_T_fields{4},arra
y_T_fields{5},array_T_fields{6},array_T_fields{7},array_T_fields{8},array_T_fields{9
});
        }
        if(nPts==10){
visualize(array_T_fields{1},array_T_fields{2},array_T_fields{3},array_T_fields{4},arra
y_T_fields{5},array_T_fields{6},array_T_fields{7},array_T_fields{8},array_T_fields{9
},array_T_fields{10});
        }
        if(nPts==11){
visualize(array_T_fields{1},array_T_fields{2},array_T_fields{3},array_T_fields{4},arra
y_T_fields{5},array_T_fields{6},array_T_fields{7},array_T_fields{8},array_T_fields{9
},array_T_fields{10},array_T_fields{11});
        }
        if(nPts==12){
visualize(array_T_fields{1},array_T_fields{2},array_T_fields{3},array_T_fields{4},arra
y_T_fields{5},array_T_fields{6},array_T_fields{7},array_T_fields{8},array_T_fields{9
},array_T_fields{10},array_T_fields{11},array_T_fields{12});
        }
        if(nPts==13){
visualize(array_T_fields{1},array_T_fields{2},array_T_fields{3},array_T_fields{4},arra
y_T_fields{5},array_T_fields{6},array_T_fields{7},array_T_fields{8},array_T_fields{9
},array_T_fields{10},array_T_fields{11},array_T_fields{12},array_T_fields{13});
        }
        if(nPts==14){
visualize(array_T_fields{1},array_T_fields{2},array_T_fields{3},array_T_fields{4},arra
y_T_fields{5},array_T_fields{6},array_T_fields{7},array_T_fields{8},array_T_fields{9
},array_T_fields{10},array_T_fields{11},array_T_fields{12},array_T_fields{13},array_
T_fields{14});
        }
        if(nPts==15){
visualize(array_T_fields{1},array_T_fields{2},array_T_fields{3},array_T_fields{4},arra
y_T_fields{5},array_T_fields{6},array_T_fields{7},array_T_fields{8},array_T_fields{9
},array_T_fields{10},array_T_fields{11},array_T_fields{12},array_T_fields{13},array_
T_fields{14},array_T_fields{15});
}
        }else{
```

```
        if(nPts==16){
visualize(array_T_fields{1},array_T_fields{2},array_T_fields{3},array_T_fields{4},arra
y_T_fields{5},array_T_fields{6},array_T_fields{7},array_T_fields{8},array_T_fields{9
},array_T_fields{10},array_T_fields{11},array_T_fields{12},array_T_fields{13},array_
T_fields{14},array_T_fields{15},array_T_fields{16});
        }
        if(nPts==17){
visualize(array_T_fields{1},array_T_fields{2},array_T_fields{3},array_T_fields{4},arra
y_T_fields{5},array_T_fields{6},array_T_fields{7},array_T_fields{8},array_T_fields{9
},array_T_fields{10},array_T_fields{11},array_T_fields{12},array_T_fields{13},array_
T_fields{14},array_T_fields{15},array_T_fields{16},array_T_fields{17});
        }
        if(nPts==18){
visualize(array_T_fields{1},array_T_fields{2},array_T_fields{3},array_T_fields{4},arra
y_T_fields{5},array_T_fields{6},array_T_fields{7},array_T_fields{8},array_T_fields{9
},array_T_fields{10},array_T_fields{11},array_T_fields{12},array_T_fields{13},array_
T_fields{14},array_T_fields{15},array_T_fields{16},array_T_fields{17},array_T_fields
{18});
        }
        if(nPts==19){
visualize(array_T_fields{1},array_T_fields{2},array_T_fields{3},array_T_fields{4},arra
y_T_fields{5},array_T_fields{6},array_T_fields{7},array_T_fields{8},array_T_fields{9
},array_T_fields{10},array_T_fields{11},array_T_fields{12},array_T_fields{13},array_
T_fields{14},array_T_fields{15},array_T_fields{16},array_T_fields{17},array_T_fields
{18},array_T_fields{19});
        }
        if(nPts==20){
visualize(array_T_fields{1},array_T_fields{2},array_T_fields{3},array_T_fields{4},arra
y_T_fields{5},array_T_fields{6},array_T_fields{7},array_T_fields{8},array_T_fields{9
},array_T_fields{10},array_T_fields{11},array_T_fields{12},array_T_fields{13},array_
T_fields{14},array_T_fields{15},array_T_fields{16},array_T_fields{17},array_T_fields
{18},array_T_fields{19},array_T_fields{20});
        }
        if(nPts==21){
visualize(array_T_fields{1},array_T_fields{2},array_T_fields{3},array_T_fields{4},arra
y_T_fields{5},array_T_fields{6},array_T_fields{7},array_T_fields{8},array_T_fields{9
},array_T_fields{10},array_T_fields{11},array_T_fields{12},array_T_fields{13},array_
T_fields{14},array_T_fields{15},array_T_fields{16},array_T_fields{17},array_T_fields
{18},array_T_fields{19},array_T_fields{20},array_T_fields{21});
        }
        if(nPts==22){
visualize(array_T_fields{1},array_T_fields{2},array_T_fields{3},array_T_fields{4},arra
y_T_fields{5},array_T_fields{6},array_T_fields{7},array_T_fields{8},array_T_fields{9
},array_T_fields{10},array_T_fields{11},array_T_fields{12},array_T_fields{13},array_
T_fields{14},array_T_fields{15},array_T_fields{16},array_T_fields{17},array_T_fields
{18},array_T_fields{19},array_T_fields{20},array_T_fields{21},array_T_fields{22});
```

```
        }
        if(nPts==23){
visualize(array_T_fields{1},array_T_fields{2},array_T_fields{3},array_T_fields{4},arra
y_T_fields{5},array_T_fields{6},array_T_fields{7},array_T_fields{8},array_T_fields{9
},array_T_fields{10},array_T_fields{11},array_T_fields{12},array_T_fields{13},array_
T_fields{14},array_T_fields{15},array_T_fields{16},array_T_fields{17},array_T_fields
{18},array_T_fields{19},array_T_fields{20},array_T_fields{21},array_T_fields{22},arr
ay_T_fields{23});
        }
        if(nPts==24){
visualize(array_T_fields{1},array_T_fields{2},array_T_fields{3},array_T_fields{4},arra
y_T_fields{5},array_T_fields{6},array_T_fields{7},array_T_fields{8},array_T_fields{9
},array_T_fields{10},array_T_fields{11},array_T_fields{12},array_T_fields{13},array_
T_fields{14},array_T_fields{15},array_T_fields{16},array_T_fields{17},array_T_fields
{18},array_T_fields{19},array_T_fields{20},array_T_fields{21},array_T_fields{22},arr
ay_T_fields{23},array_T_fields{24});
        }
        if(nPts==25){
visualize(array_T_fields{1},array_T_fields{2},array_T_fields{3},array_T_fields{4},arra
y_T_fields{5},array_T_fields{6},array_T_fields{7},array_T_fields{8},array_T_fields{9
},array_T_fields{10},array_T_fields{11},array_T_fields{12},array_T_fields{13},array_
T_fields{14},array_T_fields{15},array_T_fields{16},array_T_fields{17},array_T_fields
{18},array_T_fields{19},array_T_fields{20},array_T_fields{21},array_T_fields{22},arr
ay_T_fields{23},array_T_fields{24},array_T_fields{25});
        }
        if(nPts==26){
visualize(array_T_fields{1},array_T_fields{2},array_T_fields{3},array_T_fields{4},arra
y_T_fields{5},array_T_fields{6},array_T_fields{7},array_T_fields{8},array_T_fields{9
},array_T_fields{10},array_T_fields{11},array_T_fields{12},array_T_fields{13},array_
T_fields{14},array_T_fields{15},array_T_fields{16},array_T_fields{17},array_T_fields
{18},array_T_fields{19},array_T_fields{20},array_T_fields{21},array_T_fields{22},arr
ay_T_fields{23},array_T_fields{24},array_T_fields{25},array_T_fields{26});
        }
        if(nPts==27){
visualize(array_T_fields{1},array_T_fields{2},array_T_fields{3},array_T_fields{4},arra
y_T_fields{5},array_T_fields{6},array_T_fields{7},array_T_fields{8},array_T_fields{9
},array_T_fields{10},array_T_fields{11},array_T_fields{12},array_T_fields{13},array_
T_fields{14},array_T_fields{15},array_T_fields{16},array_T_fields{17},array_T_fields
{18},array_T_fields{19},array_T_fields{20},array_T_fields{21},array_T_fields{22},arr
ay_T_fields{23},array_T_fields{24},array_T_fields{25},array_T_fields{26},array_T_fie
lds{27});
        }
        if(nPts==28){
visualize(array_T_fields{1},array_T_fields{2},array_T_fields{3},array_T_fields{4},arra
y_T_fields{5},array_T_fields{6},array_T_fields{7},array_T_fields{8},array_T_fields{9
},array_T_fields{10},array_T_fields{11},array_T_fields{12},array_T_fields{13},array_
```

```
T_fields{14},array_T_fields{15},array_T_fields{16},array_T_fields{17},array_T_fields
{18},array_T_fields{19},array_T_fields{20},array_T_fields{21},array_T_fields{22},arr
ay_T_fields{23},array_T_fields{24},array_T_fields{25},array_T_fields{26},array_T_fie
lds{27},array_T_fields{28});
            }
        if(nPts==29){
visualize(array_T_fields{1},array_T_fields{2},array_T_fields{3},array_T_fields{4},arra
y_T_fields{5},array_T_fields{6},array_T_fields{7},array_T_fields{8},array_T_fields{9
},array_T_fields{10},array_T_fields{11},array_T_fields{12},array_T_fields{13},array_
T_fields{14},array_T_fields{15},array_T_fields{16},array_T_fields{17},array_T_fields
{18},array_T_fields{19},array_T_fields{20},array_T_fields{21},array_T_fields{22},arr
ay_T_fields{23},array_T_fields{24},array_T_fields{25},array_T_fields{26},array_T_fie
lds{27},array_T_fields{28},array_T_fields{29});
            }
        if(nPts==30){
visualize(array_T_fields{1},array_T_fields{2},array_T_fields{3},array_T_fields{4},arra
y_T_fields{5},array_T_fields{6},array_T_fields{7},array_T_fields{8},array_T_fields{9
},array_T_fields{10},array_T_fields{11},array_T_fields{12},array_T_fields{13},array_
T_fields{14},array_T_fields{15},array_T_fields{16},array_T_fields{17},array_T_fields
{18},array_T_fields{19},array_T_fields{20},array_T_fields{21},array_T_fields{22},arr
ay_T_fields{23},array_T_fields{24},array_T_fields{25},array_T_fields{26},array_T_fie
lds{27},array_T_fields{28},array_T_fields{29},array_T_fields{30});
            }
        }
    }
  }
}


################################################################################
# Scriptfile: create_nanohole.lsf
#
# Description: Creates a nanohole with variable hole size and periodicity.
################################################################################


# Add the metallic surface
addrect;
get;
set("name",materialname);
set("material",materialtype);
if(shape==0){
    set("x span",2*rect_span);
    set("y span",2*rect_span);
}
if(shape==2){
    set("x span",3*rect_span);
```

```
        set("y span",2*wirelength);
    }
    if(shape==1){
        set("x span",2*min_periodicity);
        set("y span",2*sqrt(3)*min_periodicity);
    }
    set("z span",rect_zspan);
    set("z",circ_z);

    # Add the pyrex
    addrect;
    get;
    set("name","Pyrex");
    set("index",recti_index);
    if(shape==0){
        set("x span",2*rect_span);
        set("y span",2*rect_span);
    }
    if(shape==2){
        set("x span",3*rect_span);
        set("y span",2*wirelength);
    }
    if(shape==1){
        set("x span",2*min_periodicity);
        set("y span",2*sqrt(3)*min_periodicity);
    }
    set("z span",recti_zspan);
    set("z",recti_z);

    # Add the SiO layer if checked
    if(SiOcheck==1){
        addrect;
        get;
        set("name","SiO");
        set("material","SiO2 (Glass) - Palik");
        if(shape==0){
            set("x span",2*rect_span);
            set("y span",2*rect_span);
        }
        if(shape==2){
            set("x span",3*rect_span);
            set("y span",2*wirelength);
        }
        if(shape==1){
            set("x span",2*min_periodicity);
            set("y span",2*sqrt(3)*min_periodicity);
```

```
    }
    set("z span",SiOthickness);
    set("z",(2*circ_z)+(SiOthickness/2));
}

# Etch the holes in the metallic surface
if(shape==0){
    addcircle;
    get;
    set("material","etch");
    if(SiOcheck==1){
        set("material","SiO2 (Glass) - Palik");
    }
    set("name","Etch");
    set("radius",circ_r);
    set("z span",rect_zspan+0.01e-007);
    set("z",circ_z+0.005e-007);
}
if(shape==2){
    addrect;
    get;
    set("material","etch");
    if(SiOcheck==1){
        set("material","SiO2 (Glass) - Palik");
    }
    set("name","Etch");
    set("x span",circ_r*2);
    set("y span",wirelength);
    set("z span",rect_zspan+0.01e-007);
    set("z",circ_z+0.005e-007);
}
if(shape==1){
    addcircle;
    set("x",0);
    set("y",0);
    set("material","etch");
    set("name","Etch");
    set("radius",circ_r);
    set("z span",circ_zspan);
    set("z",circ_z);
    if(SiOcheck==1){
        set("material","SiO2 (Glass) - Palik");
        # addcircle;
        # set("x",0);
        # set("y",0);
        # set("material","etch");
```

```
    # set("name","SiO2 (Glass) - Palik");
    # set("radius",circ_r);
    # set("z span",SiOthickness);
    # set("z",(2*circ_z)+(SiOthickness/2));
}

addcircle;
set("x",-min_periodicity/2);
set("y",-sqrt(3)*min_periodicity/2);
set("material","etch");
set("name","Etch");
set("radius",circ_r);
set("z span",circ_zspan);
set("z",circ_z);
if(SiOcheck==1){
    set("material","SiO2 (Glass) - Palik");
    # addcircle;
    # set("x",-min_periodicity/2);
    # set("y",-sqrt(3)*min_periodicity/2);
    # set("material","etch");
    # set("name","SiO2 (Glass) - Palik");
    # set("radius",circ_r);
    # set("z span",SiOthickness);
    # set("z",(2*circ_z)+(SiOthickness/2));
}

addcircle;
set("x",min_periodicity/2);
set("y",-sqrt(3)*min_periodicity/2);
set("material","etch");
set("name","Etch");
set("radius",circ_r);
set("z span",circ_zspan);
set("z",circ_z);
if(SiOcheck==1){
    set("material","SiO2 (Glass) - Palik");
    # addcircle;
    # set("x",min_periodicity/2);
    # set("y",-sqrt(3)*min_periodicity/2);
    # set("material","SiO2 (Glass) - Palik");
    # set("name","Etch");
    # set("radius",circ_r);
    # set("z span",SiOthickness);
    # set("z",(2*circ_z)+(SiOthickness/2));
}
```

```
        addcircle;
        set("x",min_periodicity/2);
        set("y",sqrt(3)*min_periodicity/2);
        set("material","etch");
        set("name","Etch");
        set("radius",circ_r);
        set("z span",circ_zspan);
        set("z",circ_z);
        if(SiOcheck==1){
            set("material","SiO2 (Glass) - Palik");
            # addcircle;
            # set("x",min_periodicity/2);
            # set("y",sqrt(3)*min_periodicity/2);
            # set("material","SiO2 (Glass) - Palik");
            # set("name","Etch");
            # set("radius",circ_r);
            # set("z span",SiOthickness);
            # set("z",(2*circ_z)+(SiOthickness/2));
        }

        addcircle;
        set("x",-min_periodicity/2);
        set("y",sqrt(3)*min_periodicity/2);
        set("material","etch");
        set("name","Etch");
        set("radius",circ_r);
        set("z span",circ_zspan);
        set("z",circ_z);
        if(SiOcheck==1){
            set("material","SiO2 (Glass) - Palik");
            # addcircle;
            # set("x",-min_periodicity/2);
            # set("y",sqrt(3)*min_periodicity/2);
            # set("material","SiO2 (Glass) - Palik");
            # set("name","Etch");
            # set("radius",circ_r);
            # set("z span",SiOthickness);
            # set("z",(2*circ_z)+(SiOthickness/2));
        }
    }

addfdtd;
get;
set("background index",fdtd_index);
set("mesh accuracy",fdtd_meshacc);
if(shape==0){
```

```
        set("x span",fdtd_xspan);
        set("y span",fdtd_yspan);
        if(testangles==0){
            set("allow symmetry on all boundaries",1);
            set("x min bc","Anti-Symmetric");
            set("x max bc","Anti-Symmetric");
            set("y min bc","Symmetric");
            set("y max bc","Symmetric");
        }else{
            set("x min bc","Periodic");
            set("x max bc","Periodic");
            set("y min bc","Periodic");
            set("y max bc","Periodic");
        }
    }
    if(shape==2){
        set("x span",fdtd_xspan);
        set("y span",fdtd_yspan);
        if(testangles==0){
            set("allow symmetry on all boundaries",1);
            if(per == 0){
                set("x min bc","Periodic");
                set("x max bc","Periodic");
                set("y min bc","PML");
                set("y max bc","PML");
            }
            if(per == 1){
                set("x min bc","Anti-Symmetric");
                set("x max bc","Anti-Symmetric");
                set("y min bc","Symmetric");
                set("y max bc","Symmetric");
            }
        }else{
            set("allow symmetry on all boundaries",1);
            set("x min bc","Anti-Symmetric");
            set("x max bc","Anti-Symmetric");
            set("y min bc","Symmetric");
            set("y max bc","Symmetric");
        }
    }
    if(shape==1){
        set("x span",min_periodicity);
        set("y span",(sqrt(3)*min_periodicity));
        set("allow symmetry on all boundaries",1);
        set("x min bc","Anti-Symmetric");
        set("x max bc","Anti-Symmetric");
```

```
        set("y min bc","Symmetric");
        set("y max bc","Symmetric");
    }
    set("z span",fdtd_zspan);
    if(SiOcheck==1){
        set("z span",fdtd_zspan+SiOthickness);
        set("z",SiOthickness);
    }

    #set("x min bc","PML");
    #set("x max bc","PML");
    #set("y min bc","PML");
    #set("y max bc","PML");

    #addmesh;
    #get;
    #set("x span",mesh_xspan);
    #set("y span",mesh_yspan);
    #set("z span",mesh_zspan);
    #set("z",mesh_z);
    #set("dx",mesh_derivative);
    #set("dy",mesh_derivative);
    #set("dz",mesh_derivative);

    addplane;
    get;
    set("angle theta",ang);
    if(shape==0){
        set("x span",3*rect_span);
        set("y span",3*rect_span);
    }
    if(shape==2){
        set("x span",3*rect_span);
        set("y span",2*wirelength);
    }
    if(shape==1){
        set("x span",2*min_periodicity);
        set("y span",2*sqrt(3)*min_periodicity);
    }
    set("wavelength start",plane_wlstart);
    set("wavelength stop",plane_wlstop);
    set("z",plane_z);

    addpower;
    get;
    if(shape==0){
```

```
set("x span",3*rect_span);
set("y span",3*rect_span);
}
if(shape==2){
    set("x span",3*rect_span);
    set("y span",2*wirelength);
}
if(shape==1){
    set("x span",2*min_periodicity);
    set("y span",2*sqrt(3)*min_periodicity);
}
set("z",monitor_z);
if(SiOcheck==1){
    set("z",monitor_z+SiOthickness);
}
set("override global monitor settings",1);
set("frequency points",monitor_frequencypoints);
```

Appendix B – Supporting Information

Tunable 3D plasmonic cavity nanosensors for surface-enhanced Raman spectroscopy with sub-femtomolar limit of detection [i]

Mohammadali Tabatabaei [1], Mohamadreza Najiminaini [2, 3, 4], Kieffer Davieau [2, 5], Bozena

Kaminska [4], Mahi R. Singh [5], Jeffrey J.L. Carson [2, 3] and François Lagugné-Labarthet [1, 5]

---

[1] *Department of Chemistry and Center for Advanced Materials and Biomaterials, University of Western Ontario*

[2] *Imaging Program, Lawson Health Research Institute St. Joseph's Health Care*

[3] *Department of Medical Biophysics, Schulich School of Medicine and Dentistry, University of Western Ontario*

[4] *The School of Engineering Science, Simon Fraser University*

[5] *Department of Physics, University of Western Ontario*
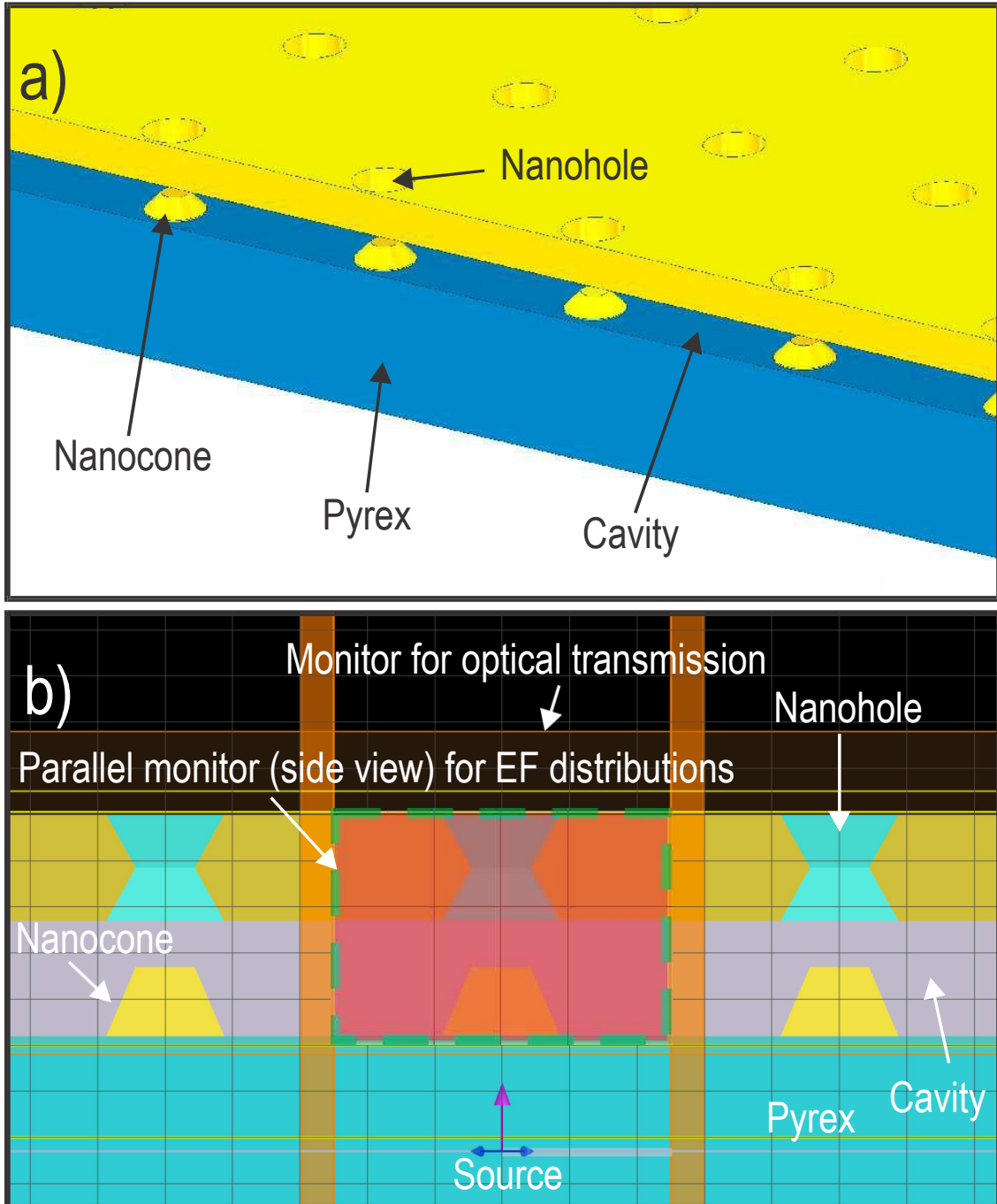
Figure SI1. (a) Schematic of 3D plasmonic nanosensor displaying a cavity beneath the Au layer, and truncated nanocones at the bottom of the cavity; (b) Layout of FDTD simulation model including boundary conditions for optical properties and electromagnetic field (EF) distribution of 3D plasmonic nanosensors with a periodicity of 500 nm.
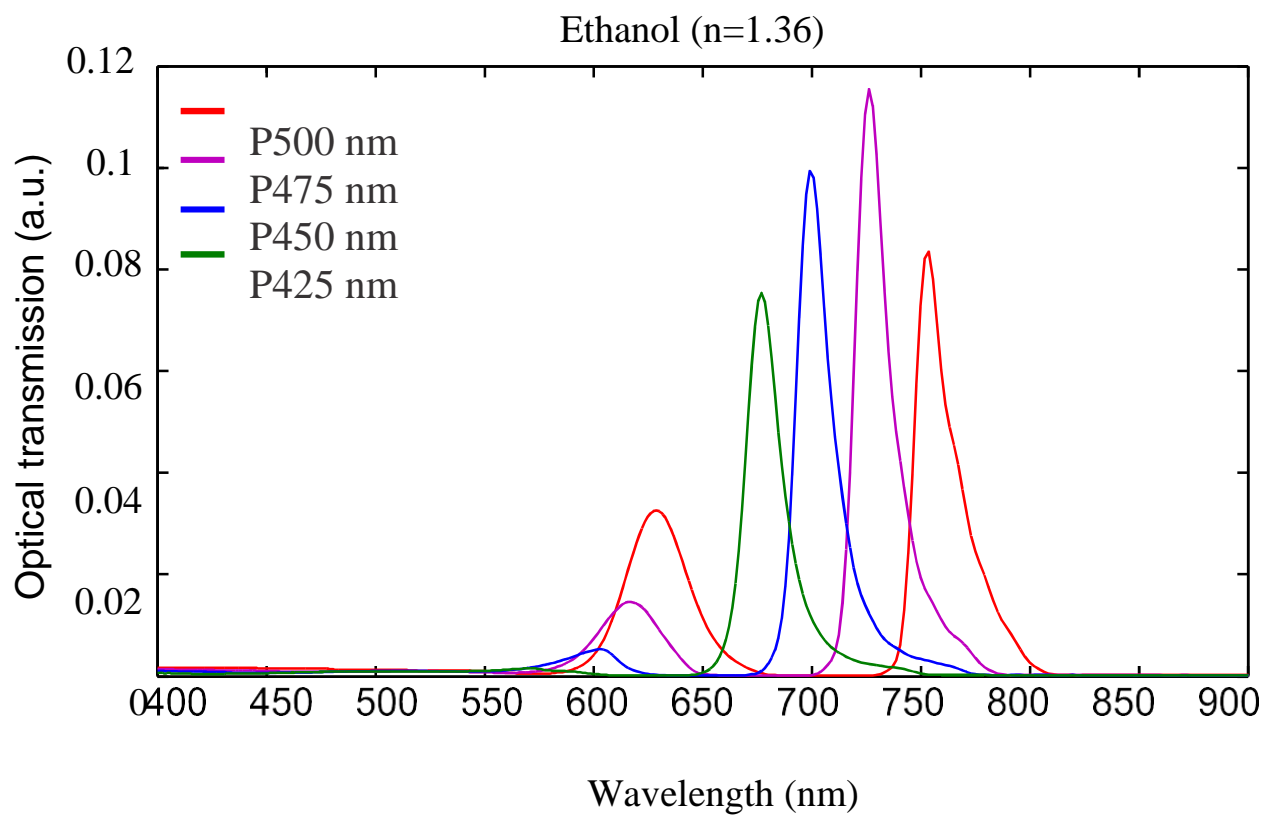
Figure SI2. Simulated optical transmission spectra of 3D cavity plasmonic nanosensors in Ethanol (n=1.36). The periodicities range from 425 nm (green curve) to 500 nm (red curve) with increments of 25 nm.
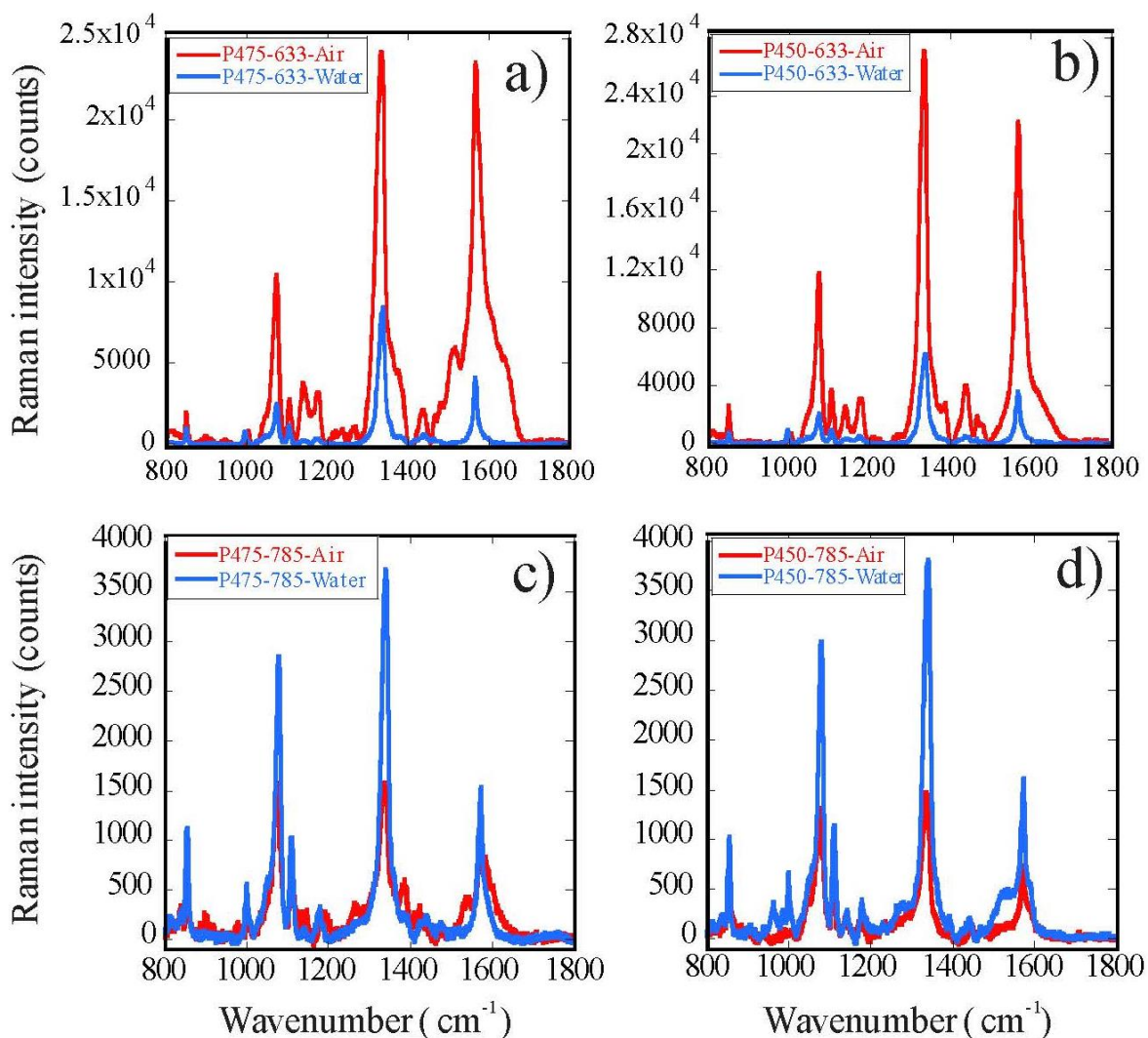
Figure SI3. SERS spectra of 4-NTP adsorbed on the 3D nanosensors with different periodicities, medium (air and water) and wavelength of incident light. a) P475 nm and b) P450 nm periodicities at 633 nm incident light in air (red) and water (blue); c) P475 nm and d) 450 nm periodicities at 785 nm in air (red) and water (blue). Acquisition time for each spectrum was 3 s with 5 accumulations. Base line correction was applied to all spectra.

Enhancement factor calculation

In order to obtain the surface Raman enhancement factor for the sensors, we collected the reference non-SERS Raman spectra of a 1 mM solution of 4-NTP on a blank (sensor-free) substrate. Based on the concentration, the number of molecules that will be placed in the confocal volume can be calculated as number of molecules = confocal volume $\times$ concentration $\times N_A = 10^{-15}$ L $\times 10^{-3}$ mole/L $\times 6 \times 10^{23}$ molecules/mole $= 6 \times 10^5$ molecules. This number represents N_{NE} with the Raman intensity of 2×10^2 (I_{NE}) for vs NO$_2$. The number of molecules in 100 μL of 100 aM solution of 4-NTP can be calculated as $10^{-16} \times 100 \times 10^{-6} = 10^{-20}$ mole which represents $10^{-20} \times 6 \times 10^{23} = 6 \times 10^3$ molecules. For the similar situation one can calculate the number of molecules in 100 μL solution of 100 aM 4-NTP drop-casted onto the sensors to determine the number of adsorbed molecules in the confocal region for SERS measurement. For this, the surface area accessible on the nanosensor (P500) for functionalization is around 2.5×10^3 μm^2. Considering the number of molecules in the 100 μL volume, we can then estimate an average number of molecules per hot spot adsorbed in the confocal region (~ 1 μm^2) to be $6 \times 10^3 / 2.5 \times 10^3 = 2$ molecules (N_{SERS}) with the SERS intensity of 8×10^3 (I_{SERS}) for vs NO$_2$. In both cases a X100 (N.A.= 0.9) objective was used. Considering these calculations, the EF is estimated as:

$$EF = \frac{N_{NE} \times I_{SERS}}{I_{NE} \times N_{SERS}} = \frac{6 \times 10^5 \times 8 \times 10^3}{2 \times 10^2 \times 2} = 1.2 \times 10^7$$

Therefore, a surface Raman EF of $\sim 1.2 \times 10^7$ was achieved for 100 aM 4-NTP from a femtoliter plasmonic focal volume.
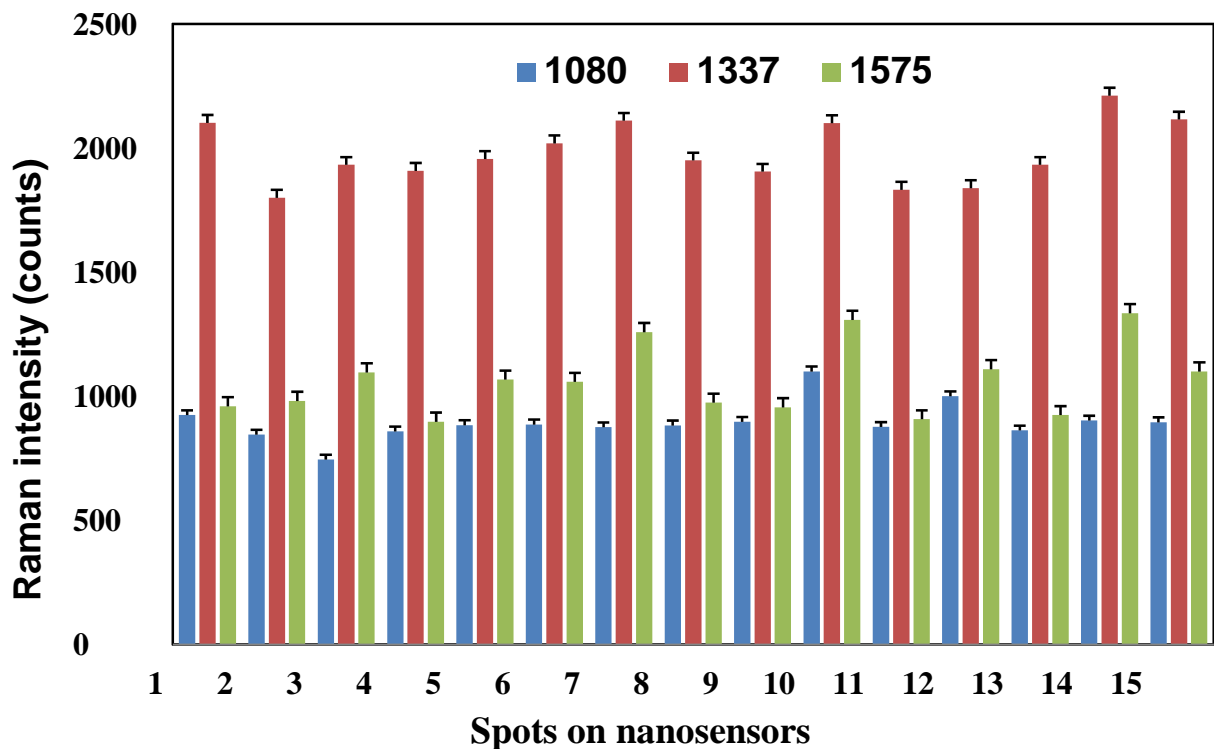
Figure SI4. Standard error analysis of SERS signals for three main peaks of 4-NTP (100 aM) at 1080 (vs C-H), 1337 (vs NO2), and 1575 (vs C-C) cm-1 obtained on 15 spots (average of 3 experiments for each spot) of the P500 nanosensors. The standard error bars are generated based on the obtained mean values of 895.3, 1980.6, 1061.7 (a.u.) for the Raman intensities at 1080, 1337, and 1575 cm-1, respectively.
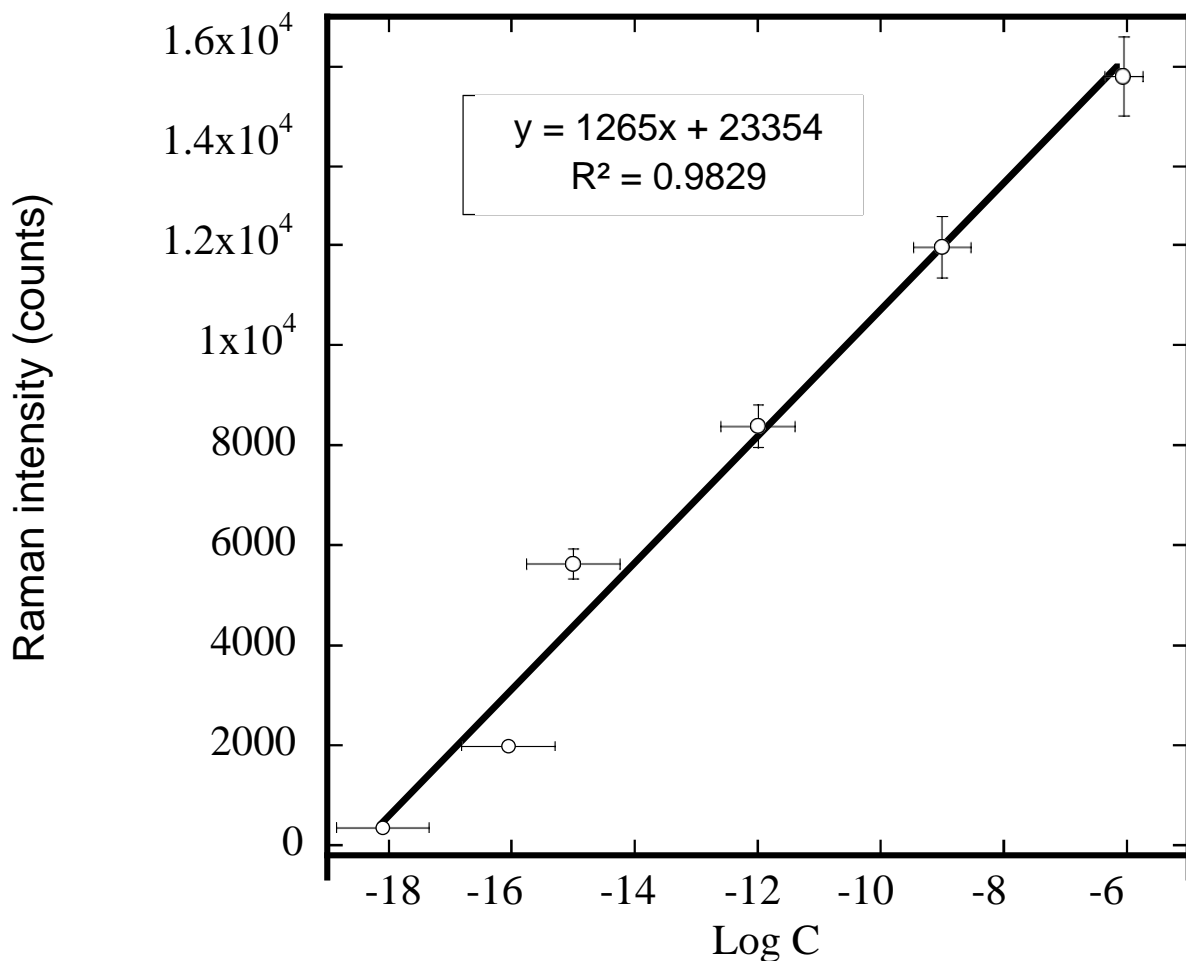
Figure SI5. Sensitivity of sensors represented by SERS signals of vs NO_2 with respect to the Log [Concentration] between 1 aM and 1 µM. Although the SERS intensities do not provide a linear relationship with respect to concentrations, as shown in Fig. SI5, there is a linear relationship between the intensities of signals and the logarithmic concentrations of the solutions between 1 µM and 1 aM. This arise the fact that SERS is a surface sensitive technique and is dependent on the number of molecules located in the hot spots to generate signal. In other terms, a single molecule located within a hot spot can generate a strong signal, whereas many molecules located outside of a hot spot may generate no signal. In order to determine the sensitivity of the sensor once can use the $\frac{\Delta I}{\Delta LogC}$. The corresponding slope of such plot is of 1.2×10^3 (Fig. SI5) and can be used as a parameter of choice to estimate the sensitivity of a given sensor.

Bibliography

i. Tabatabaei, M., Najiminaini, M., Davieau, K., Kaminska, B., Singh, M.R., Carson, J.J.L., & F. Lagugné-Labarthet. "Tunable 3D plasmonic cavity nanosensors for surface-enhanced Raman spectroscopy with sub-femtomolar limit of detection." ACS Photonics 2(6): 752-759 (2015).

Appendix C – Derivation for Matrix Elements ρ_{ij} [43], [55]

In this section the derivation of equation of motion for density matrix elements is explained. The Hamiltonian of SPP modes in the second quantized form is written as [i]

$$H_0 = \varepsilon_0 \sigma_{00} + \varepsilon_1 \sigma_{11} + \varepsilon_2 \sigma_{22} + \varepsilon_3 \sigma_{33} + \varepsilon_4 \sigma_{44} + \varepsilon_5 \sigma_{55} \tag{7.15}$$

where $\sigma_{nn} = |n\rangle \langle n|$ is called the preservation operator.

When an external EM field E_p is applied, dipole moments are induced. The interaction Hamiltonian between photons and induced dipole moments in rotating wave approximation is written as

$$H_F = -\left[\hbar \sum_{n=1}^{5} \Omega_{0n} \sigma_{0n}^+ e^{-i\frac{(\varepsilon_{n0} - \varepsilon_p)t}{\hbar}} \right] + h.c. \tag{7.16}$$

where $\sigma_{0n}^+ = |n\rangle \langle 0|$ is the SPP creation operator and $\varepsilon_{n0} = (\varepsilon_n - \varepsilon_0)$. Here *h.c.* stands for the Hermitian conjugate. Parameter Ω_{0n} is called the Rabi frequency associated with the transition between $|0\rangle$ and $|n\rangle$. The total Hamiltonian of the system is given by

$$H = H_0 + H_F \tag{7.17}$$

$$H = \varepsilon_0 \sigma_{00} + \varepsilon_1 \sigma_{11} + \varepsilon_2 \sigma_{22} + \varepsilon_3 \sigma_{33} + \varepsilon_4 \sigma_{44} + \varepsilon_5 \sigma_{55}$$
$$- \left[\hbar \sum_{n=1}^{5} \Omega_{0n} \sigma_{0n}^+ e^{-i\frac{(\varepsilon_{n0} - \varepsilon_p)t}{\hbar}} \right] + h.c. \tag{7.18}$$

Considering the interaction representation

$$H_F = e^{-i\frac{H_0 t}{\hbar}} H_F e^{+i\frac{H_0 t}{\hbar}} \tag{7.19}$$

It follows that

$$
H_F = -\hbar
\begin{bmatrix}
\left(\Omega_{01}\sigma_{10}e^{-i\omega t-i\omega_1 t+i\omega_0 t} + \Omega_{01}^*\sigma_{01}e^{+i\omega t+i\omega_1 t-i\omega_0 t} \right) + \\[6pt]
\left(\Omega_{02}\sigma_{20}e^{-i\omega t-i\omega_2 t+i\omega_0 t} + \Omega_{02}^*\sigma_{02}e^{+i\omega t+i\omega_2 t-i\omega_0 t} \right) + \\[6pt]
\left(\Omega_{03}\sigma_{30}e^{-i\omega t-i\omega_3 t+i\omega_0 t} + \Omega_{03}^*\sigma_{03}e^{+i\omega t+i\omega_3 t-i\omega_0 t} \right) + \\[6pt]
\left(\Omega_{04}\sigma_{40}e^{-i\omega t-i\omega_4 t+i\omega_0 t} + \Omega_{04}^*\sigma_{04}e^{+i\omega t+i\omega_4 t-i\omega_0 t} \right) + \\[6pt]
\left(\Omega_{05}\sigma_{50}e^{-i\omega t-i\omega_5 t+i\omega_0 t} + \Omega_{05}^*\sigma_{05}e^{+i\omega t+i\omega_5 t-i\omega_0 t} \right)
\end{bmatrix}
\tag{7.20}
$$

We can simplify the above Hamiltonians to

$$
H_F = -\hbar
\begin{bmatrix}
\left(\Omega_{01}\sigma_{10}e^{-i\Delta_{10}t} + \Omega_{01}^*\sigma_{01}e^{+i\Delta_{10}t} \right) + \\[6pt]
\left(\Omega_{02}\sigma_{20}e^{-i\Delta_{20}t} + \Omega_{02}^*\sigma_{02}e^{+i\Delta_{20}t} \right) + \\[6pt]
\left(\Omega_{03}\sigma_{30}e^{-i\Delta_{30}t} + \Omega_{03}^*\sigma_{03}e^{+i\Delta_{30}t} \right) + \\[6pt]
\left(\Omega_{04}\sigma_{40}e^{-i\Delta_{40}t} + \Omega_{04}^*\sigma_{04}e^{+i\Delta_{40}t} \right) + \\[6pt]
\left(\Omega_{05}\sigma_{50}e^{-i\Delta_{50}t} + \Omega_{05}^*\sigma_{05}e^{+i\Delta_{50}t} \right)
\end{bmatrix}
\tag{7.21}
$$

where

$$
\Delta_{10} = \omega - (\omega_1 - \omega_0) \tag{7.22}
$$

$$
\Delta_{20} = \omega - (\omega_2 - \omega_0) \tag{7.23}
$$

$$
\Delta_{30} = \omega - (\omega_3 - \omega_0) \tag{7.24}
$$

$$
\Delta_{40} = \omega - (\omega_4 - \omega_0) \tag{7.25}
$$

$$
\Delta_{50} = \omega - (\omega_5 - \omega_0)
$$

where the density matrix element is

$$
\frac{d\tilde{\rho}}{dt} = -\frac{i}{\hbar}\left[H_F, \tilde{\rho} \right] \tag{7.26}
$$

$$
\tilde{\rho}_{mn} = \langle m|\tilde{\rho}|n \rangle \tag{7.27}
$$

We are only considering the interaction terms because of the interaction representation. With this information, we are able to calculate the density matrix operators for each state.

Let us consider ρ_{55}

$$\left\langle 5 \left| \frac{d\tilde{\rho}}{dt} \right| 5 \right\rangle = \left\langle 5 \left| -\frac{i}{\hbar} \left[H_F, \tilde{\rho} \right] \right| 5 \right\rangle \tag{7.28}$$

$$i\hbar \frac{d\tilde{\rho}_{55}}{dt} = \left\langle 5 \left| \left[H_F, \tilde{\rho} \right] \right| 5 \right\rangle \tag{7.29}$$

Let us calculate each section separately

$$A = \left\langle 5 \left| \left[H_F, \tilde{\rho} \right] \right| 5 \right\rangle \tag{7.30}$$

Now we recalling the commutation of operators

$$[X, Y] = XY - YX \tag{7.31}$$

With this we can solve the following term

$$A = \left\langle 5 \left| \left[H_F, \tilde{\rho} \right] \right| 5 \right\rangle \tag{7.32}$$

$$A = \left\langle 5 \left| H_F \tilde{\rho} - \tilde{\rho} H_F \right| 5 \right\rangle \tag{7.33}$$

We must multiply by one $\Sigma_i |i\rangle \langle i| = 1$

$$A = \left\langle 5 \left| H_F \left(\Sigma_i |i\rangle \langle i| \right) \tilde{\rho} - \tilde{\rho} \left(\Sigma_i |i\rangle \langle i| \right) H_F \right| 5 \right\rangle \tag{7.34}$$

$$= \left\langle 5 \left| \begin{array}{c} H_F \left(|0\rangle \langle 0| + |1\rangle \langle 1| + |2\rangle \langle 2| + |3\rangle \langle 3| + |4\rangle \langle 4| + |5\rangle \langle 5| \right) \tilde{\rho} \\ -\tilde{\rho} \left(|0\rangle \langle 0| + |1\rangle \langle 1| + |2\rangle \langle 2| + |3\rangle \langle 3| + |4\rangle \langle 4| + |5\rangle \langle 5| \right) \tilde{\rho} H_F \end{array} \right| 5 \right\rangle \tag{7.35}$$

$$= \left\langle 5 \left| H_F |0\rangle \langle 0| \tilde{\rho} \right| 5 \right\rangle + \left\langle 5 \left| H_F |1\rangle \langle 1| \tilde{\rho} \right| 5 \right\rangle + \left\langle 5 \left| H_F |2\rangle \langle 2| \tilde{\rho} \right| 5 \right\rangle$$

$$+ \left\langle 5 \left| H_F |3\rangle \langle 3| \tilde{\rho} \right| 5 \right\rangle + \left\langle 5 \left| H_F |4\rangle \langle 4| \tilde{\rho} \right| 5 \right\rangle + \left\langle 5 \left| H_F |5\rangle \langle 5| \tilde{\rho} \right| 5 \right\rangle$$

$$- \left\langle 5 \left| \tilde{\rho} |0\rangle \langle 0| H_F \right| 5 \right\rangle - \left\langle 5 \left| \tilde{\rho} |1\rangle \langle 1| H_F \right| 5 \right\rangle - \left\langle 5 \left| \tilde{\rho} |2\rangle \langle 2| H_F \right| 5 \right\rangle$$

$$- \left\langle 5 \left| \tilde{\rho} |3\rangle \langle 3| H_F \right| 5 \right\rangle - \left\langle 5 \left| \tilde{\rho} |4\rangle \langle 4| H_F \right| 5 \right\rangle - \left\langle 5 \left| \tilde{\rho} |5\rangle \langle 5| H_F \right| 5 \right\rangle \tag{7.36}$$

$$= \langle 5 |H_F| 0\rangle \tilde{\rho}_{05} + \langle 5 |H_F| 1\rangle \tilde{\rho}_{15} + \langle 5 |H_F| 2\rangle \tilde{\rho}_{25} +$$

$$\langle 5 |H_F| 3\rangle \tilde{\rho}_{35} + \langle 5 |H_F| 4\rangle \tilde{\rho}_{45} + \langle 5 |H_F| 5\rangle \tilde{\rho}_{55}$$

$$-\tilde{\rho}_{50} \langle 0 |H_F| 5\rangle - \tilde{\rho}_{51} \langle 1 |H_F| 5\rangle - \tilde{\rho}_{52} \langle 2 |H_F| 5\rangle$$

$$-\tilde{\rho}_{53} \langle 3 |H_F| 5\rangle - \tilde{\rho}_{54} \langle 4 |H_F| 5\rangle - \tilde{\rho}_{55} \langle 5 |H_F| 5\rangle \tag{7.37}$$

To solve the above set of equations we need to remember H_F

$$H_F = -\hbar \begin{bmatrix} \left(\Omega_{01} \sigma_{10} e^{-i\Delta_{10}t} + \Omega_{01}^* \sigma_{01} e^{+i\Delta_{10}t} \right) + \\ \left(\Omega_{02} \sigma_{20} e^{-i\Delta_{20}t} + \Omega_{02}^* \sigma_{02} e^{+i\Delta_{20}t} \right) + \\ \left(\Omega_{03} \sigma_{30} e^{-i\Delta_{30}t} + \Omega_{03}^* \sigma_{03} e^{+i\Delta_{30}t} \right) + \\ \left(\Omega_{04} \sigma_{40} e^{-i\Delta_{40}t} + \Omega_{04}^* \sigma_{04} e^{+i\Delta_{40}t} \right) + \\ \left(\Omega_{05} \sigma_{50} e^{-i\Delta_{50}t} + \Omega_{05}^* \sigma_{05} e^{+i\Delta_{50}t} \right) \end{bmatrix} \tag{7.38}$$

Where $\sigma_{mn} = |m\rangle\langle n|$

$$\langle 5 | H_F | 0 \rangle = \left\langle 5 \left| -\hbar \begin{bmatrix} \left(|1\rangle\langle 0|\Omega_{01}e^{-i\Delta_{10}t} + |0\rangle\langle 1|\Omega_{01}^*e^{+i\Delta_{10}t} \right) + \\ \left(|2\rangle\langle 0|\Omega_{02}e^{-i\Delta_{20}t} + |0\rangle\langle 2|\Omega_{02}^*e^{+i\Delta_{20}t} \right) + \\ \left(|3\rangle\langle 0|\Omega_{03}e^{-i\Delta_{30}t} + |0\rangle\langle 3|\Omega_{03}^*e^{+i\Delta_{30}t} \right) \\ + \left(|4\rangle\langle 0|\Omega_{04}e^{-i\Delta_{40}t} + |0\rangle\langle 4|\Omega_{04}^*e^{+i\Delta_{40}t} \right) + \\ \left(|5\rangle\langle 0|\Omega_{05}e^{-i\Delta_{50}t} + |0\rangle\langle 5|\Omega_{05}^*e^{+i\Delta_{50}t} \right) \end{bmatrix} \right| 0 \right\rangle \quad (7.39)$$

$$= \quad 0+0+0+0+0+0+0+0+\Omega_{05}e^{-i\Delta_{50}t}+0$$

$$\langle 5 | H_F | 0 \rangle = -\hbar\Omega_{05}e^{-i\Delta_{50}t}$$

$$\langle 5 | H_F | 1 \rangle = \langle 5 | H_F | 2 \rangle = \langle 5 | H_F | 3 \rangle = \langle 5 | H_F | 4 \rangle = \langle 5 | H_F | 5 \rangle = 0$$

$$\langle 0 | H_F | 5 \rangle = -\hbar\Omega_{05}^*e^{+i\Delta_{50}t}$$

$$\langle 1 | H_F | 5 \rangle = \langle 2 | H_F | 5 \rangle = \langle 3 | H_F | 5 \rangle = \langle 4 | H_F | 5 \rangle = \langle 5 | H_F | 5 \rangle = 0$$

Thus

$$A = -\Omega_{05}e^{-i\Delta_{50}t}\tilde{\rho}_{05} + \tilde{\rho}_{50}\Omega_{05}^*e^{+i\Delta_{50}t} \quad (7.40)$$

Finally, we can collect all the terms. We get the following equation of motion

$$i\hbar\frac{d\tilde{\rho}_{55}}{dt} = \left\langle 5 \left| \left[H_F, \tilde{\rho} \right] \right| 5 \right\rangle \quad (7.41)$$

$$= \quad A$$

$$= \quad -\hbar\Omega_{05}e^{-i\Delta_{50}t}\tilde{\rho}_{05} + \hbar\tilde{\rho}_{50}\Omega_{05}^*e^{+i\Delta_{50}t} \quad (7.42)$$

We can further simplify the equations by substituting the following

$$\tilde{\rho}_{55} = \rho_{55} \tag{7.43}$$

$$\tilde{\rho}_{50} = \rho_{50}e^{-i\Delta_{50}t} \tag{7.44}$$

$$\tilde{\rho}_{51} = \rho_{51}e^{-i\Delta_{50}t+i\Delta_{10}t} \tag{7.45}$$

The new equations take the form as

$$\frac{d\rho_{55}}{dt} = +i\left(\Omega_{05}\right)\rho_{05} - i\left(\Omega_{05}\right)^{*}\rho_{50} \tag{7.46}$$

Including the radiative linewidth of the state we get the following

$$\frac{d\rho_{55}}{dt} = -2\Gamma_{5}\rho_{55} + i\left(\Omega_{05}\right)\rho_{05} - i\left(\Omega_{05}\right)^{*}\rho_{50} \tag{7.47}$$

Using the same method, we would get the equation of motion for other density matrix

elements ρ_{jj}

Now, let us consider ρ_{50}

$$\left\langle 5 \left| \frac{d\tilde{\rho}}{dt} \right| 0 \right\rangle = \left\langle 5 \left| -\frac{i}{\hbar}\left[H_F, \tilde{\rho} \right] \right| 0 \right\rangle \tag{7.48}$$

$$i\hbar\frac{d\tilde{\rho}_{50}}{dt} = \left\langle 5 \left| \left[H_F, \tilde{\rho} \right] \right| 0 \right\rangle \tag{7.49}$$

Let us calculate each section separately

$$A = \left\langle 5 \left| \left[H_F, \tilde{\rho} \right] \right| 0 \right\rangle \tag{7.50}$$

Now we must remember the commutation of operators

$$[X, Y] = XY - YX \tag{7.51}$$

With this we can solve the following term

$$A = \left\langle 5 \left| \left[H_F, \tilde{\rho} \right] \right| 0 \right\rangle \tag{7.52}$$

$$A = \left\langle 5 \left| H_F \tilde{\rho} - \tilde{\rho} H_F \right| 0 \right\rangle \tag{7.53}$$

We must multiply by one $\Sigma_i |i\rangle \langle i| = 1$

$$A = \left\langle 5 \left| H_F \left(\Sigma_i |i\rangle \langle i| \right) \tilde{\rho} - \tilde{\rho} \left(\Sigma_i |i\rangle \langle i| \right) H_F \right| 0 \right\rangle \tag{7.54}$$

$$= \left\langle 5 \left| \begin{array}{l} H_F \left(|0\rangle \langle 0| + |1\rangle \langle 1| + |2\rangle \langle 2| + |3\rangle \langle 3| + |4\rangle \langle 4| + |5\rangle \langle 5| \right) \tilde{\rho} \\ \\ -\tilde{\rho} \left(|0\rangle \langle 0| + |1\rangle \langle 1| + |2\rangle \langle 2| + |3\rangle \langle 3| + |4\rangle \langle 4| + |5\rangle \langle 5| \right) H_F \end{array} \right| 0 \right\rangle \tag{7.55}$$

$$= \left\langle 5 \left| H_F |0\rangle \langle 0| \tilde{\rho} \right| 0 \right\rangle + \left\langle 5 \left| H_F |1\rangle \langle 1| \tilde{\rho} \right| 0 \right\rangle + \left\langle 5 \left| H_F |2\rangle \langle 2| \tilde{\rho} \right| 0 \right\rangle$$

$$+ \left\langle 5 \left| H_F |3\rangle \langle 3| \tilde{\rho} \right| 0 \right\rangle + \left\langle 5 \left| H_F |4\rangle \langle 4| \tilde{\rho} \right| 0 \right\rangle + \left\langle 5 \left| H_F |5\rangle \langle 5| \tilde{\rho} \right| 0 \right\rangle$$

$$- \left\langle 5 \left| \tilde{\rho} |0\rangle \langle 0| H_F \right| 0 \right\rangle - \left\langle 5 \left| \tilde{\rho} |1\rangle \langle 1| H_F \right| 0 \right\rangle - \left\langle 5 \left| \tilde{\rho} |2\rangle \langle 2| H_F \right| 0 \right\rangle$$

$$- \left\langle 5 \left| \tilde{\rho} |3\rangle \langle 3| H_F \right| 0 \right\rangle - \left\langle 5 \left| \tilde{\rho} |4\rangle \langle 4| H_F \right| 0 \right\rangle - \left\langle 5 \left| \tilde{\rho} |5\rangle \langle 5| H_F \right| 0 \right\rangle \tag{7.56}$$

$$= \langle 5| H_F |0\rangle \rho_{00} + \langle 5| H_F |1\rangle \rho_{10} + \langle 5| H_F |2\rangle \rho_{20} + \langle 5| H_F |3\rangle \rho_{30} +$$

$$\langle 5| H_F |4\rangle \rho_{40} + \langle 5| H_F |5\rangle \rho_{50}$$

$$- \langle 0| H_F |0\rangle \rho_{50} - \langle 1| H_F |0\rangle \rho_{51} - \langle 2| H_F |0\rangle \rho_{52} - \langle 3| H_F |0\rangle \rho_{53} -$$

$$\langle 4| H_F |1\rangle \rho_{54} - \langle 5| H_F |1\rangle \rho_{55} \tag{7.57}$$

To solve the above set of equations we need to remember H_F

$$H_F = -\hbar \left[\begin{array}{l} \left(\Omega_{01} \sigma_{10} e^{-i\Delta_{10}t} + \Omega_{01}^* \sigma_{01} e^{+i\Delta_{10}t} \right) + \\ \\ \left(\Omega_{02} \sigma_{20} e^{-i\Delta_{20}t} + \Omega_{02}^* \sigma_{02} e^{+i\Delta_{20}t} \right) + \\ \\ \left(\Omega_{03} \sigma_{30} e^{-i\Delta_{30}t} + \Omega_{03}^* \sigma_{03} e^{+i\Delta_{30}t} \right) + \\ \\ \left(\Omega_{04} \sigma_{40} e^{-i\Delta_{40}t} + \Omega_{04}^* \sigma_{04} e^{+i\Delta_{40}t} \right) + \\ \\ \left(\Omega_{05} \sigma_{50} e^{-i\Delta_{50}t} + \Omega_{05}^* \sigma_{05} e^{+i\Delta_{50}t} \right) \end{array} \right] \tag{7.58}$$

where $\sigma_{mn} = |m\rangle \langle n|$

$$\langle 5|H_F|0\rangle = \left\langle 5 \left| \hbar \begin{bmatrix} \left(|1\rangle\langle 0|\Omega_{01}e^{-i\Delta_{10}t} + |0\rangle\langle 1|\Omega_{01}^*e^{+i\Delta_{10}t}\right) \\ + \left(|2\rangle\langle 0|\Omega_{02}e^{-i\Delta_{20}t} + |0\rangle\langle 2|\Omega_{02}^*e^{+i\Delta_{20}t}\right) \\ + \left(|3\rangle\langle 0|\Omega_{03}e^{-i\Delta_{30}t} + |0\rangle\langle 3|\Omega_{03}^*e^{+i\Delta_{30}t}\right) \\ + \left(|4\rangle\langle 0|\Omega_{04}e^{-i\Delta_{40}t} + |0\rangle\langle 4|\Omega_{04}^*e^{+i\Delta_{40}t}\right) \\ + \left(|5\rangle\langle 0|\Omega_{05}e^{-i\Delta_{50}t} + |0\rangle\langle 5|\Omega_{05}^*e^{+i\Delta_{50}t}\right) \end{bmatrix} \right| 0 \right\rangle \quad (7.59)$$

$$= 0+0+0+0+0+0+0+0+\Omega_{05}e^{-i\Delta_{50}t}+0 \quad (7.60)$$

$$\langle 5|H_F|1\rangle = \langle 5|H_F|2\rangle = \langle 5|H_F|3\rangle = \langle 5|H_F|4\rangle = \langle 5|H_F|5\rangle = 0$$

$$\langle 1|H_F|0\rangle = \Omega_{01}e^{-i\Delta_{10}t}, \langle 2|H_F|0\rangle = \Omega_{02}e^{-i\Delta_{20}t}, \langle 3|H_F|0\rangle = \Omega_{03}e^{-i\Delta_{30}t},$$

$$\langle 4|H_F|0\rangle = \Omega_{04}e^{-i\Delta_{40}t}$$

Thus

$$A = \Omega_{05}e^{-i\Delta_{50}t}\left(\tilde{\rho_{55}} - \tilde{\rho_{00}}\right) + \hbar\Omega_{01}e^{-i\Delta_{10}t}\tilde{\rho_{51}} + \hbar\Omega_{02}e^{-i\Delta_{20}t}\tilde{\rho_{52}} + \hbar\Omega_{03}e^{-i\Delta_{30}t}\tilde{\rho_{53}} + \hbar\Omega_{04}e^{-i\Delta_{40}t}\tilde{\rho_{54}}$$

$$(7.61)$$

Finally, we can collect all the terms. We get the following equation of motion.

$$i\hbar\frac{d\tilde{\rho_{50}}}{dt} = \left\langle 5 \left| \left[H_F, \tilde{\rho}\right] \right| 0 \right\rangle \quad (7.62)$$

$$= A \quad (7.63)$$

$$\frac{d\tilde{\rho_{50}}}{dt} = -i\Omega_{05}e^{-i\Delta_{50}t}\left(\tilde{\rho_{55}} - \tilde{\rho_{00}}\right)$$

$$-i(\Omega_{01}e^{-i\Delta_{10}t})\tilde{\rho_{51}} - i(\Omega_{02}e^{-i\Delta_{20}t})\tilde{\rho_{52}} - i(\Omega_{03}e^{-i\Delta_{30}t})\tilde{\rho_{53}} - i(\Omega_{04}e^{-i\Delta_{40}t})\tilde{\rho_{54}}$$

We can further simplify the equations by substituting the following

$$\tilde{\rho}_{55} = \rho_{55} \tag{7.64}$$

$$\tilde{\rho}_{50} = \rho_{50}e^{-i\Delta_{50}t} \tag{7.65}$$

$$\tilde{\rho}_{51} = \rho_{51}e^{-i\Delta_{50}t+i\Delta_{10}t} \tag{7.66}$$

By taking into consideration

$$\frac{d(\rho_{50}e^{-i\Delta_{50}t})}{dt} = \frac{d(\rho_{50})}{dt}e^{-i\Delta_{50}t} + \rho_{50}\frac{d(e^{-i\Delta_{50}t})}{dt} \tag{7.67}$$

$$= \frac{d(\rho_{50})}{dt}e^{-i\Delta_{50}t} - i\Delta_{50}\rho_{50}(e^{-i\Delta_{50}t}) \tag{7.68}$$

Including the radiative linewidth we get the following

$$\frac{d\rho_{50}}{dt} = -\left(\frac{\Gamma_5}{2} + i\Delta_{50}\right)\rho_{50} - i\Omega_{05}\left(\tilde{\rho}_{55} - \tilde{\rho}_{00}\right) - i(\Omega_{01})\rho_{51} - i(\Omega_{02})\tilde{\rho}_{52} - i(\Omega_{03})\tilde{\rho}_{53} - i(\Omega_{04})\tilde{\rho}_{54} \tag{7.69}$$

Using the same method, we would get the equation of motion for other density matrix elements.

Bibliography

i. M. R. Singh, *Electronic, Photonic, Polaritonic and Plasmonic Materials* (John Wiley and Sons, Toronto, 2014).

References

1 Ebbesen, T. W.; Lezec, H. J.; Ghaemi, H. F.; Thio, T.; Wolff, P. A. Extraordinary optical transmission through sub-wavelength hole arrays. Nature 1998, 391, 667−669. Retrieved from http://dx.doi.org/10.1038/35570.

2 Krishnan, A.; Thio, T.; Kim, T. J.; Lezec, H. J.; Ebbesen, T. W.; Wolff, P. A.; Pendry, J.; Martin-Moreno, L.; Garcia-Vidal, F. J. Evanescently coupled resonance in surface plasmon enhanced transmission. Opt. Commun. 2001, 200, 1−7.

3 Najiminaini, M.; Vasefi, F.; Kaminska, B.; Carson, J. J. L. "Effect of surface plasmon energy matching on the sensing capability of metallic nano---hole arrays," Appl. Phys. Lett., vol. 100, no. 063110, 2012.

4 Najiminaini, M.; Vasefi, F.; Kaminska, B.; Carson, J. J. L. Nanohole array structure with improved surface plasmon energy matching characteristics. Appl. Phys. Lett. 2012, 100, 043105.

5 Przybilla, F.; Degiron, A.; Laluet, J.-Y.; Genet, C.; Ebbesen, T. W. Optical transmission in perforated noble and transition metal films. J. Opt. A: Pure Appl. Opt. 2006, 8, 458.

6 Valsecchi, C.; Brolo, A. G. Periodic metallic nanostructures as plasmonic chemical sensors. Langmuir 2013, 29, 5638−5649.

7 Brolo, A. G.; Gordon, R.; Leathem, B.; Kavanagh, K. L. Surface plasmon sensor based on the enhanced light transmission through arrays of nanoholes in gold films. Langmuir 2004, 20, 4813−4815.

8 Najiminaini, M.; Ertorer, E.; Kaminska, B.; Mittler, S.; Carson, J. J. L. Surface plasmon resonance sensing properties of a 3D nanostructure consisting of aligned nanohole and nanocone arrays. Analyst 2014, 139, 1876−1882.

9 Gordon, R.; Sinton, D.; Kavanagh, K. L.; Brolo, A. G. A new generation of sensors based on extraordinary optical transmission. Acc. Chem. Res. 2008, 41, 1049−1057.

10 Brolo, A. G. Plasmonics for future biosensors. Nat. Photonics. 2012, 6, 709−713.

11 Passarelli, N.; Perez, L. A.; Coronado, E. A. Plasmonicinteractions: from molecular plasmonics and Fano resonances to ferroplasmons. ACS Nano 2014, 8, 9723−9728.

12 Sonntag, M. D.; Klingsporn, J. M.; Zrimsek, A. B.; Sharma, B.; Ruvuna, L. K.; Van Duyne, R. P. Molecular plasmonics for nanoscalespectroscopy. Chem. Soc. Rev. 2014, 43, 1230−1247.

13 Baffou, G.; Quidant, R. Nanoplasmonics for chemistry. Chem. Soc. Rev.2014,43, 3898−3907.

14 M. Najiminaini, F. Vasefi, B. Kaminska, and J. J. L. Carson, "Optical resonance transmission properties of nano-hole arrays in a gold film: effect of adhesion layer," Opt. Express, vol. 19, no. 27, p. 26186, 2011.

15 Genet, C.; Ebbesen, T. W. Light in tiny holes. Nature 2007, 445, 39−46.

16 Yokogawa, S.; Burgos, S. P.; Atwater, H. A. Plasmonic color filters for CMOS image sensor applications. Nano Lett. 2012, 12, 4349−4354.

17 Yanik, A. A.; Cetin, A. E.; Huang, M.; Artar, A.; Mousavi, S. H.; Khanikaev, A.; Connor, J. H.; Shvets, G.; Altug, H. Seeing protein monolayers with naked eye through plasmonic Fano resonances. Proc. Nat. Acad. Sci. 2011, 108, 11784−11789.

18 Cervantes Tellez, G. A.; Hassan, S. a.; Tait, R. N.; Berini, P.; Gordon, R. Atomically flat symmetric elliptical nanohole arrays in a gold film for ultrasensitive refractive index sensing. Lab Chip 2013, 13, 2541−2546.

19 Fleischmann, M.; Hendra, P. J.; McQuillan, A. J. Raman spectra of pyridine adsorbed at a silver electrode. J. Chem. Phys. Lett. 1974, 26, 163−166.

20 Jeanmaire, D. L.; Van Duyne, R. P. Surface Raman spectroelectrochemistry: Part I. Heterocyclic, aromatic, and aliphatic amines adsorbed on the anodized silver electrode. J. Electroanal. Chem. 19977, 84, 1−20.

21 Nie, S.; Emory, S. R. Probing single molecules and single nanoparticles by surface-enhanced Raman scattering. Science 1997, 275, 1102−1106.

22 Kneipp, K.; Wang, Y.; Kneipp, H.; Perelman, L. T.; Itzkan, I.; Dasari, R. R.; Feld, M. S. Single molecule detection using surface enhanced Raman scattering (SERS). Phys. Rev. Lett. 1997, 78, 1667−1670.

23 Im, H.; Wittenberg, N. J.; Lesuffleur, A.; Lindquist, N. C.; Oh, S.-H. Membrane protein biosensing with plasmonic nanopore arrays and pore-spanning lipid membranes. Chem. Sci. 2010, 1, 688−696.

24 Im, H.; Lee, S. H.; Wittenberg, N. J.; Johnson, T. W.; Lindquist, N. C.; Nagpal, P.; Norris, D. J.; Oh, S.-H. Template-stripped smooth Ag nanohole arrays with silica shells for surface plasmon resonance biosensing. ACS Nano 2011, 5, 6244−6253.

25 Wang, Y.; Kar, A.; Paterson, A.; Kourentzi, K.; Le, H.; Ruchhoeft, P.; Willson, R.; Bao, J. Transmissive nanohole arrays for massively-parallel optical biosensing. ACS Photonics 2014, 1, 241−245.

26 Ricciardi, A.; Consales, M.; Quero, G.; Crescitelli, A.; Esposito, E.; Cusano, A. Versatile optical fiber nanoprobes: from plasmonic biosensors to polarization-sensitive devices. ACS Photonics 2014, 1, 69−78.

27 Barnes, W. L.; Dereux, A.; Ebbesen, T. W. Surface plasmon subwavelength optics. Nature 2003, 424, 824−830. Retrieved from http://dx.doi.org/10.1038/nature01937.

28 Lee, M.; Kim, J.; Seo, W.; Hong, H.-G.; Song, Y.; Dasari, R. R.; An, K. Three-dimensional imaging of cavity vacuum with single atoms localized by a nanohole array. Nat. Commun. 2014, 5, 3441.

29 L. Solymar and E. Shamonina, Waves in metamaterials. Oxford: Oxford University Press, 2009.

30 M. R. Singh. Electronic, Photonic, Polaritonic and Plasmonic Materials. Toronto: Wiley Custom, 2014.

31 C. Carloz and T. Itoh. Electromagnetic Metamaterials. New Jersey: John Wiley and Sons, 2006.

32 Balakrishnan, S., Najiminaini, M., Singh, M. R., Carson, J. J. L., "A study of angle dependent surface plasmon polaritons in nano-hole array structures." Journal of Applied Physics, 120, 034302 (2016).

33 Fayyaz, S.; Tabatabaei, M.; Hou, R.; Lagugné-Labarthet, F. Surface-enhanced fluorescence: mapping individual hot spots in silicaprotected 2D gold nanotriangle arrays. J. Phys. Chem. C 2012, 116, 11665−11670.

34 Aroca, R. F.; Ross, D. J.; Domingo, C. Surface-enhanced infrared spectroscopy. Appl. Spectrosc. 2004, 58, 324A−338A.

35 Jensen, T.; Kelly, L.; Lazarides, A.; Schatz, G. Electrodynamics of noble metal nanoparticles and nanoparticle clusters. J. Cluster Sci. 1999, 10, 295−317.

36 Brown, L. V.; Yang, X.; Zhao, K.; Zheng, B. Y.; Nordlander, P.; Halas, N. J. Fan-shaped gold nanoantennas above reflective substrates for surface-enhanced infrared absorption (SEIRA). Nano Lett. 2015, 15, 1272−1280.

37 Sheehan, P. E.; Whitman, L. J. Detection limits for nanoscale biosensors. Nano Lett. 2005, 5, 803−807.

38 Squires, T. M.; Messinger, R. J.; Manalis, S. R. Making it stick: convection, reaction and diffusion in surface-based biosensors. Nat. Biotechnol. 2008, 26, 417−426.

39 Kumar, S.; Cherukulappurath, S.; Johnson, T. W.; Oh, S.-H. Millimeter-sized suspended plasmonic nanohole arrays for surface-tension-driven flow-through SERS. Chem. Mater. 2014, 26, 6523−6530.

40 Brolo, A. G.; Arctander, E.; Gordon, R.; Leathem, B.; Kavanagh, K. L. Nanohole-enhanced Raman scattering. Nano Lett. 2004, 4, 2015−2018.

41 Im, H.; Sutherland, J. N.; Maynard, J. A.; Oh, S.-H. Nanoholebased surface plasmon resonance instruments with improved spectral resolution quantify a broad range of antibody-ligand binding kinetics. Anal. Chem. 2012, 84, 1941−1947.

42 Merlen, A.; Lagugné-Labarthet, F. Imaging the optical near field in plasmonic nanostructures. Appl. Spectrosc. 2014, 68, 1307−1326.

43 Bukasov, R.; Ali, T. A.; Nordlander, P.; Shumaker-Parry, J. S. Probing the plasmonic near-field of gold nanocrescent antennas. ACS Nano 2010, 4, 6639−6650.

44 Tabatabaei, M.; Sangar, A.; Kazemi-Zanjani, N.; Torchio, P.; Merlen, A.; Lagugné-Labarthet, F. Optical properties of silver and gold tetrahedral nanopyramid arrays prepared by nanosphere lithography. J. Phys. Chem. C 2013, 117, 14778−14786.

45 Yu, Q.; Guan, P.; Qin, D.; Golden, G.; Wallace, P. M. Inverted size-dependence of surface-enhanced Raman scattering on gold nanohole and nanodisk arrays. Nano Lett. 2008, 8, 1923−1928.

46 Zheng, P.; Cushing, S. K.; Suri, S.; Wu, N. Tailoring plasmonic properties of gold nanohole arrays for surface enhanced Raman scattering. Phys. Chem. Chem. Phys. 2015, DOI: 10.1039/C4CP05291A.

47 Y. Pang and R. Gordon, "Optical trapping of a single protein," Nano Lett., vol. 12, no. 1, pp. 402– 406, 2012.

48 S. E. E. Harris, J. E. E. Field, and A. Imamoglu, "Nonlinear optical processes using electromagnetically induced transparency," Phys. Rev. Lett., vol. 64, no. 10, pp. 3–5, 1990.

49 M. O. Scully and M. S. Zubairy, Quantum Optics. London: Cambridge University Press, 1997.

50 G. S. Agarwal, Quantum Optics (Springer Tracts in Modern Physics), vol. 70. Springer, Berlin, 1976.

51 D. G. Angelakis, E. Paspalakis, P. L. Knight, D. G. Angelakis, E. Paspalakis, E. Paspalakis, E. Paspalakis, P. L. Knight, E. Paspalakis, and G. B. Serapiglia, "Mod. Opt.," vol. 47, no. 1025, 2000.

52 O. G. Calderón, M. A. Antón, and F. Carreño, "Near dipole-dipole effects in a V-type medium with vacuum induced coherence," Eur. Phys. J. D, vol. 25, no. 77, 2003.

53 Raether, H. (1988). Surface plasmons. Berlin: Springer-Verlag.

54 Tetz, K. (2006). Plasmonics in the near-infrared: Spatial, spectral, and temporal studies of Surface plasmon polaritons. (Unpublished).

55 Stefan A. Maier, Plasmonics: Fundamentals and Applications, Springerscience + Business media LLC, New York, 2007.

56 M. R. Singh, M. Najiminaini, S. Balakrishnan, and J. J. L. Carson, "Metamaterial-based theoretical description of light scattering by metallic nano-hole array structures," no. April, pp. 2–3, 2014.

57 Schatz, G. C.; Young, M. A.; Van Duyne, R. P. In Surface-enhanced Raman scattering. Kneipp, K., Moskovits, M., Kneipp, H., Eds.; Springer-Verlag: Berlin, 2006; Vol. 103, pp 19−46.

58 Felidj, N.; Aubard, J.; Levi, G.; Krenn, J. R.; Salerno, M.; Schider, G.; Lamprecht, B.; Leitner, A.; Aussenegg, F. R. Controlling the optical response of regular arrays of gold particles for surface-enhanced Raman scattering. Phys. Rev. B 2002, 65, 075419.

59 M. R. Singh, D. Schindel, and A. Hatef, "Dipole-dipole interaction in a quantum dot and metallic nanorod hybrid system," Appl. Phys. Lett., vol. 99, no. 181106, 2011.

60 Palik, E. D. Handbook of Optical Constants of Solids. Academic Press: New York, 1985.

61 Skadtchenko, B. O.; Aroca, R. Surface-enhanced Raman scattering of p-nitrothiophenol: Molecular vibrations of its silver salt and the surface complex formed on silver islands and colloids. Spectrochim. Acta A Mol. Biomol. Spectrosc. 2001, 57, 1009−1016.

62 Marquestaut, N.; Martin, A.; Talaga, D.; Servant, L.; Ravaine, S.; Reculusa, S.; Bassani, D. M.; Gillies, E.; Lagugne-Labarthet, F. Raman enhancement of azobenzene monolayers on substrates prepared   by Langmuir−Blodgett deposition and electron-beam lithography techniques. Langmuir 2008, 24, 11313−11321.

63 Felidj, N.; Truong, S. L.; Aubard, J.; Levi, G.; Krenn, J. R.; Hohenau, A.; Leitner, A.; Aussenegg, F. R. Gold particle interaction in regular arrays probed by surface enhanced Raman scattering. J. Chem. Phys. 2004, 120, 7141−7146.

64 L. Novotny and B. Hecht, "Principles of Nano-Optics," 2nd ed., no. November. Cambridge University Press, 2012.

65 M. R. Singh. Electronic, Photonic, Polaritonic and Plasmonic Materials. Toronto: Wiley Custom, 2014.

66 Qin Feng, Mingbo Pu, Chenggang Hu and Xiangang Luo. "Engineering the dispersion of metamaterial surface for broadband infrared absorption," 2012 / Vol. 37, No. 11 / OPTICS LETTERS, 37, 2133 (2012).

67 Mingbo Pu, Chenggang Hu, Cheng Huang, Changtao Wang, Zeyu Zhao, Yanqin Wang, and Xiangang Luo, "Investigation of Fano resonance in planar metamaterial with perturbed periodicity," OPTICS EXPRESS 21, 992 (2013).

Curriculum Vitae

Name: Kieffer J. Davieau

Post-secondary   Wilfrid Laurier University
Education and   Waterloo, Ontario, Canada
Degrees: 2010-2014 Honours Photonics BSc.

                       The University of Western Ontario
                       London, Ontario, Canada
                       2014-2017 MSc.

Honours and   The Lillian Margaret and Walter David Jackson
Awards: Scholarship in Physics
                       MSc. Student in Physics
                       2015

                       Western Nanofabrication Facility Research Support
                       2015

Related Work   Teaching Assistant
Experience: The University of Western Ontario
                       2014-2016

                       Teaching Assistant
                       Wilfrid Laurier University
                       2011-2014

Publications:

1. Tabatabaei, M., Najiminaini, M., Davieau, K., Kaminska, B., Singh, M.R., Carson, J.J.L., & F. Lagugné-Labarthet. "*Tunable 3D plasmonic cavity nanosensors for surface-enhanced Raman spectroscopy with sub-femtomolar limit of detection.*" ACS Photonics 2(6): 752-759 (2015).

2. Singh, M. R., Davieau, K. J., and Carson, J. J. L., "*Effect of quantum interference on absorption of light in metamaterial hybrids.*" Journal of Physics D: Applied Physics, 49(44) (2016).